Metabolic Modelling of Tomato Fruit Ripening

Aliah Hazmah Hawari

St. Cross College

Thesis submitted for the degree of

Doctor of Philosophy, University of Oxford,

Department of Plant Sciences

Hilary Term 2014

Abstract

Metabolic Modelling of Tomato Fruit Ripening

Aliah H. Hawari, St. Cross College, University of Oxford

Submitted for the degree of DPhil, Hilary Term 2014

Tomatoes are the fourth most valuable commodity in agriculture after rice, wheat and soybeans globally with 151 million tonnes of fruit being produced in 2012. The tomato fruit is also a model system for fleshy fruit development. During ethylene-regulated fruit ripening there are complex changes in fruit chemical composition due to degradation and synthesis of a number of soluble and volatile metabolites. Ultimately, these changes control the composition of the ripe fruit and dictate its flavour and texture. It is known that ripening can proceed when mature green fruit are removed from the plant (and indeed this is standard commercial practice) but the extent to which metabolic changes are sustained when fruit are ripened in this way has yet to be established. A modelling approach such as constraints-based modelling can provide system-level insights into the workings of the complex tomato metabolic network during ripening. The first aim of this thesis was therefore to construct a genome-scale metabolic network model for tomato and to use this model to explore metabolic network flux distributions during the transitions between the stages of fruit ripening. The flux distributions predicted provided insight into the production and usage of energy and reductants, into routes for climacteric CO_2 release, and the metabolic routes underlying metabolite conversions during ripening. The second aim of this thesis was to use the model to explore metabolic engineering strategies for increased production of lycopene in tomato fruit. The model predictions showed that rearrangement of dominant metabolic fluxes were required to cope with the increased demand for reductants at high lycopene accumulation, which came at a cost of a lower accumulation of other secondary metabolites. Overall the thesis provides an approach to connect underlying metabolic mechanisms to the known metabolic processes that happen during ripening.

Acknowledgments

Foremost, I would like to express my sincere gratitude to my supervisors Prof. Lee J. Sweetlove and Prof. R. George Ratcliffe, for their continuous mentoring, support, encouragement and patience throughout the course of my DPhil project. A special thanks also goes to Prof. David Fell and Dr. Mark Poolman for their guidance and advice on metabolic modelling and ScrumPy; as well as for the use of their computational facilities at Oxford Brookes University.

Many thanks also to Dr. Alisdair Fernie and Dr. Fernando Carrari for sharing their experimental data for the modelling tasks in this thesis. I would also like to thank the department of Plant Sciences, for providing support and facilities throughout my study.

I would also like to thank everyone in the Sweetlove and Ratcliffe lab, particularly Dr. Maurice Cheung for his help and advice on the modelling aspects of my work. Dr. Bernadette Gehl, for her helpful discussions on tomatoes. Clare Woods, Constantine Garagounis, and Gemma Hayton for their help and advice in my writing, including the support and encouragement they have shared throughout my study.

I would also like to acknowledge the support I have received from the Cell Systems Modelling Group, especially Hassan Hartman and Achuthanunni Chokkathukalam for their help with ScrumPy and discussions on metabolic modelling.

I am also grateful to Yayasan Khazanah of Malaysia for their financial support and care throughout my study.

Last but not least, I would like to express my heartfelt appreciation to my family: my parents Dato' Dr Hawari Hussein and Datin Azura Bahaman for their constant encouragement to pursue my dreams, my husband Fadhli Nor for his patience, understanding and love to support my ambition, and my little daughter Farah Fadhli who have all made this journey more interesting and worthwhile.

Abbreviations

2KI	2-ketoisovalerate
2OG	2-oxoglutarate
3-PGA	3-phosphoglycerate
ACL	ATP-citrate lyase
ADP	adenosine diphosphate
ATP	adenosine triphosphate
BR-TU	breaker to turning transition
CDH	carbonic anhydrase
CMP	cytidine monophosphate
CO_2	carbon dioxide
coA	coenzyme A
CTP	cytidine triphosphate
DAA	days after anthesis
DAS	days after sowing
DFBA	dynamic flux balance analysis
DHAP	dihydroxyacetone phosphate
DMAPP	dimethylallyl diphosphate
DXR	deoxyxylulose-5-phosphate reductase
DXS	deoxyxylulose-5-phosphate
EC	enzyme commission
ETC	electron transport chain
FBA	flux balance analysis
FPP	farnesyl diphosphate
FUBP	fructose-1,6-bisphosphate
FVA	flux variability analysis
FW	fresh weight
GABA	γ-aminobutyrate
GAD	glutamate decarboxylase
GAP	glyceraldehyde-3-phosphate

GGPP	geranylgeranyl diphosphate
GOGAT	glutamate synthase
GPP	geranyl diphosphate
HMBPP	hydroxymethylbutenyl diphosphate
HMGR	hydroxymethylglutaryl-coA reductase
ICDH	isocitrate dehydrogenase
IPP	isopentenyl diphosphate
ME	malic enzyme
MEP	methylerythritol phosphate
MEV	mevalonate
MG-BR	mature green to breaker transition
MMM	multiscale metabolic modelling
MOMA	minimisation of metabolic adjustment
MS	mass spectometry
NAD	nicotinamide adenine dinucleotide
NADH	reduced nicotinamide adenine dinucleotide
NADP	nicotinamide adenine dinucleotide phosphate
NADPH	reduced nicotinamide adenine dinucleotide phosphate
NCC	non-fluorescent chlorophyll catabolite
NMR	nuclear magnetic resonance
OAA	oxaloacetate
ODE	ordinary differential equation
PDH	pyruvate dehydrogenase
PEP	phospho*enol*pyruvate
PEPC	phospho*enol*pyruvate carboxylase
Pi	inorganic phosphate
PPS	phospho*enol*pyruvate synthase gene
PS	pyruvate synthase
psy	phytoene synthase gene
TCA	tricarboxylic acid

Table of Contents

Chapter 1: General Introduction

1.1 Aims of this thesis

The aim of this thesis is to construct a genome-scale model of tomato (*Solanum lycopersium*) metabolism and to use this model to understand the metabolic changes during fruit ripening and to engineer fruit lycopene production *in silico*. This is important because the metabolic changes that occur during ripening determine both the flavour and nutritional composition of the fruit. There is substantial interest in altering the composition of flavour metabolites and increasing the content of health beneficial antioxidants such as lycopene. To achieve this, a network-level understanding of metabolic fluxes in fruit tissue is required.

1.2 The tomato fruit

1.2.1 Tomato fruit quality

Fruits are an important component of the human diet and consumption has been shown to reduce the risk of chronic diseases (Martin et al., 2013). The tomato is the world's most consumed fruit. Not only is the fruit highly palatable, it is also a valuable source of minerals, vitamins, fibre and antioxidants. The latter may be behind the link between tomato consumption and the lower risk of cancers and cardiovascular diseases (Canene-Adams et al., 2005; Raffo et al., 2002; Rao & Rao, 2007). Accordingly, with increasing demand for this crop, tomatoes have a high economic value. Tomatoes are the fourth most valuable commodity in agriculture globally after rice, wheat and soybeans, with 161

million tonnes of fruit being produced in 2012 [http://faostat.fao.org/]. With a growing economic value and positive health interest, improving how the fruit taste and look is important to growers, seed companies and consumers (Kader, 2008; Malundo et al., 1995; Martin et al., 2013, 2011; Tandon et al., 2003).

1.2.2 Developmental stages of tomato fruit growth and ripening

The tomato fruit is a model system for fleshy fruit development with a well characterised ethylene-regulated ripening phase. Its small diploid genome size of 950Mb and short life cycle makes this fruit tractable for research studies (Sato et al., 2012). Tomato fruit development can be divided into four distinct stages: i) cell differentiation; ii) cell division; iii) cell expansion and iv) cell ripening (Gillaspy et al., 1993). As the fruit proceeds from cell differentiation to cell expansion stages, there are prominent changes in the cell wall layers, which become thinner as the cells enlarge (Gillaspy et al., 1993). During the cell expansion phase, the fruit increases in volume and there are marked shifts in the cell wall composition (Gillaspy et al., 1993; Matas et al., 2011).

Like apples, bananas, avocadoes and melons, tomatoes undergo climacteric ripening, where ripening is accompanied by a burst of respiration and ethylene biosynthesis. The ripening stage can be further sub-divided into four smaller stages, namely mature green, breaker, turning, and ripe. The mature green stage is where the fruit has reached its final size and sugars began to rapidly accumulate. Then the first change in colour from green to yellow can be seen at the bottom of the fruit, marking the breaker stage. This is due to the transition of chloroplasts into chromoplasts and the beginning of

carotenoid accumulation. It is at this stage that the second burst of respiration, characteristic for a climacteric fruit, occurs (Andrews, 1995). At the turning stage, the surface of the fruit shows a definite change in colour from green to yellow, pink, red, or a combination of thereof, indicating the increasing content of carotenoids such as lycopene (Carrari et al., 2006). Lastly, at ripe stage the surface of the fruit is predominantly red, and sugars and acidic metabolites such as citrate, aspartate and glutamate have accumulated to high levels (Carrari et al., 2006; Salunkhe et al., 1974).

1.2.3 The ripening stages

As the metabolic changes that affect fruit quality mainly occur during ripening, many efforts to improve fruit quality have been focused on this stage. Such efforts include manipulation of fruit composition to improve nutritional value, palatability and shelf life. For instance, several genetic engineering studies have been conducted in tomato to improve the production of selected compounds such as sugars (Powell et al., 2012), carotenoids (Enfissi et al., 2010; Fraser et al., 2007; Powell et al., 2012) and anthocyanins (Butelli et al., 2008; Martin et al., 2013; Zhang et al., 2013). Many of these genetic interventions reveal the extent that different facets of ripening are inter-dependent. For example, control of plastid development through the GLK transcription factor has knock-on consequences for accumulation of metabolites including sugars and carotenoids (Powell et al., 2012). There are also metabolic inter-dependencies. Thus, constitutive overexpression of *Psy-1* gene encoding phytoene synthase in tomatoes led to the expected increases in the carotenoids

lycopene and β-carotene but also caused significant increases in amino and organic acids at the ripe stage (Fraser et al., 2007).

These observations indicate that the altered metabolite composition in the ripe fruit is the property of metabolic-network-flux distributions that change during development and that metabolism and fruit development are inter-dependent. This leads to the question as to the nature of the developmentally-regulated redistributions of metabolic flux that underpin the final metabolite composition of the ripe fruit. In order to answer this, a greater understanding of the underlying metabolic processes during ripening is required and several studies using transcriptomic, proteomic, metabolomic approaches or a combination thereof of these approaches have been reported (Carrari et al., 2006; Osorio et al., 2011; Rohrmann et al., 2011). Of these approaches, metabolite profiles provide the direct insight of metabolic change during fruit development (Carrari et al., 2006). It is clear that there are coordinated changes in metabolite levels during development that can be, in part, linked to changes in transcripts encoding the relevant enzymes (Carrari et al., 2006). Although metabolic profiles are a useful indicator of metabolic change and metabolic outputs, they do not intuitively lead to an understanding of the underlying metabolic activity. Thus, a more informative way of assessing a metabolic network is by analysing its fluxes.

1.2.4 On- and off-vine ripening

Another important factor that influences the nature of metabolic changes during ripening is whether the fruit is ripened on, or off the plant. It is

established that ripening can proceed when mature green tomatoes are taken off the plant (Arias et al., 2000; Bisogni et al., 1976; Sorrequieta et al., 2010). Thus, it is standard commercial practice to harvest a cluster at mature green stage because the fruit are hard and therefore robust for storage. Storage under controlled conditions can delay ripening until the fruit are ready for the shelf (Beckles, 2012). However, these actions are likely to have consequences for the flavour and quality of the fruit because there is a cessation of supply of water, amino acids and sugar from the mother plant. As a result, vine-ripened tomatoes have better flavour and overall quality when compared with room-ripened tomatoes (Bisogni et al., 1976). Although a more recent sensory test study suggested that there were no major differences in the flavour of on- and off-vine ripened fruit (Arias et al., 2000), there were substantial differences in metabolite compositions that could have flavour implications (Arias et al., 2000; Pek et al., 2010; Sorrequieta et al., 2013). Additionally, it was found that the content of sugars (Sorrequieta et al., 2013), and total protein (Ré et al., 2012) were lower in off-vine ripened tomatoes.

Although the aforementioned taste test study found that there were no flavour differences between off- and on-vine ripened tomatoes, it is important to note that the cultivar used in that study was of *Solanum lycopersicum* Mill cv. Laura (Arias et al., 2000). Unlike cherry tomatoes which have a reputation for their flavour (Allen et al., 1977; Kader et al., 1977; Pagliarini et al., 2001; Raffo et al., 2002), *Solanum lycopersicum* Mill cv. Laura is not known for its palatability. These differences in flavour may be due to the differences in metabolic composition of the different tomato cultivars. This is corroborated by a study that found that there are indeed changes in total soluble solids, sugars

and lycopene contents in seven different tomato cultivars during ripening (Kaur et al., 2006), and another study observed differences in flavour across eight different tomato cultivars (Pagliarini et al., 2001). Therefore, this posed the question of what determines the final metabolite composition of the fruit. The control of fruit quality, in terms of controlling the flavour and texture, mostly occurs during ripening. This is because it is during this stage that metabolites such as sugars and acids accumulate to high levels (Baxter et al., 2005; Carrari & Fernie, 2006), giving the fruit an appealing taste (Carli et al., 2009).

1.3 Analysing metabolic networks

1.3.1 Quantifying plant metabolic fluxes using metabolic flux analysis (MFA)

One effective and reliable approach to quantify metabolic fluxes is through steady-state metabolic flux analysis (MFA). This approach uses a stable isotope, typically ^{13}C or ^{14}C, to label sugar precursors such as glucose (Morgan et al., 2013; Williams et al., 2010) and/or amino acid precursors such as glutamine and asparagine (Allen & Young, 2013). These labelled precursors are incubated in a system of interest until the system reaches an isotopic and metabolic steady-state. This allows the label to be metabolised and create a labelling pattern. The redistribution of the label can then be quantified using nuclear magnetic resonance (NMR) or mass spectrometry (MS) techniques (Kruger & Ratcliffe, 2009). By fitting a mathematical model to the experimental measurements using available programs such as 13CFLUX (Wiechert et al., 2001), 13CFLUX2 (Weitzel et al., 2013), FiatFlux (Zamboni et al., 2005),

NMR2Flux (Sriram et al., 2004), or 4F (Ettenhuber et al., 2005), a flux map that best describes the experimental labelling patterns can be generated (Kruger & Ratcliffe, 2009).

MFA has been applied to several plant systems such as in developing oilseed rape embryos to describe the metabolism of Rubisco without the Calvin cycle to increase carbon conversion efficiency (Allen et al., 2009; Schwender et al., 2004), and in Arabidopsis heterotrophic cell culture to reveal the changes in metabolic fluxes under different conditions (Masakapalli et al., 2013; Williams et al., 2010). However, the limitation of this MFA method is that it is laborious (Kruger & Ratcliffe, 2009) requiring extensive analysis of stable isotope redistribution. An alternative approach to study plant metabolic fluxes is by *in silico* metabolic modelling such as Flux Balance Analysis (FBA) (Sweetlove & Ratcliffe, 2011).

1.3.2 Modelling plant metabolic networks with FBA

Given the flexibility of FBA to model large scale networks, this approach has shown to be effective for modelling various plant networks such as Arabidopsis (Cheung et al., 2013; Dal'Molin et al., 2010; Mintz-Oron et al., 2012; Poolman et al., 2009; Williams et al., 2010), maize (*Zea mays*) (Dal'Molin et al., 2010; Saha et al., 2011), rapeseed (*Brassica napus*) (Hay & Schwender, 2011a, 2011b; Pilalis et al., 2011), barley seed (*Hordeum vulgare*) (Grafahrend-Belau et al., 2009), and more recently rice (*Oryza sativa*) (Lakshmanan et al., 2013; Poolman et al., 2013). The main application of plant FBAs is to predict the changes in the metabolic network in response to different conditions, such as

varying energy demands (Poolman et al., 2009) or varying photon uptake (Poolman et al., 2013) or to explore trade-offs that relate to crop yield and performance (Schwender & Hay, 2012). However, the use of FBAs is not just limited to the above as these models can also be used to test hypotheses or predict the effects of perturbing the network such as deleting a reaction or overproducing a metabolite in the network. For example, a recent updated Arabidopsis model was used to estimate the maintenance costs when producing biomass, which is useful as this not only leads towards a more realistic flux prediction but also provided a novel way to estimate maintenance costs without substantial experimental analysis (Cheung et al., 2013). In a FBA model of barley seeds, the flexibility of the metabolic network to compensate for enzyme deletion was investigated by carrying out *in silico* knockouts and they were able to identify three essential reactions for growth (Grafahrend-Belau et al., 2009).

The heart of FBA is an optimisation technique, which is typically linear programming, that finds the optimal network flux distribution to satisfy an objective function within the constraints imposed onto the model. Commonly used objective functions include the maximisation of biomass production or growth rate, which optimises the molar yield (Feist & Palsson, 2010), and minimisation of the overall intracellular fluxes, which is a proxy for minimal enzyme-machinery costs (Holzhütter, 2004). The latter objective function usually predicts fewer reactions in the flux distribution as this will result in a lower sum of flux (Holzhütter, 2004) and also eliminates futile cycles (Cheung et al., 2013). The choice of objective functions will depend on the system and the condition under investigation and the question being addressed as no single

objective function is universally suitable (Schuetz et al., 2007). Moreover the optimal flux distribution predicted from these objective functions is not necessarily unique - multiple optimal solutions may be found. This is due to the nature of the network that may have alternative routes towards the biosynthesis of its metabolites that are equivalent in terms of the objective value. In addition, the structure of plant metabolic networks further complicates the situation. Subcellular compartmentation in the metabolic network also leads towards alternative flux distributions (Sweetlove & Ratcliffe, 2011).

1.4 Metabolic models as tools to represent the metabolic network

Mathematical models provide a framework to simulate, predict, modify and understand metabolic networks. These models can be seen as an abstract representation of a metabolic network and the stoichiometric matrix is a way to represent the stoichiometric coefficients of the metabolites in all the reactions involved (Fell & Schuster, 2007). As an example, matrix N in Equation 2, below, represents a compilation of all stoichiometric coefficients of these two reactions:

$$\text{glucose} + \text{ATP} \leftrightarrow \text{glucose-6-phosphate} + \text{ADP} \qquad \textbf{Equation 1a}$$

$$\text{glucose-6-phosphate} \leftrightarrow \text{fructose-6-phosphate} \qquad \textbf{Equation 1b}$$

$$\mathrm{N} = \begin{bmatrix} -1 & 0 \\ -1 & 0 \\ 1 & -1 \\ 1 & 0 \\ 0 & 1 \end{bmatrix} \qquad \textbf{Equation 2}$$

In matrix N, each column from left to right represent reactions in Equation 1a (hexokinase) and 1b (phosphoglucoisomerase) respectively. Meanwhile, each row represents the five metabolites glucose, ATP, glucose-6-phosphate,

ADP, and fructose-6-phosphate from top to bottom. To differentiate between substrates in the left hand side of the equation from the products in the right hand side of the equation, the stoichiometric coefficients are taken as negative for substrates and positive for products.

To effectively describe the reactions that are involved in the network, mathematical equations that follow the law of mass conservation are used. The law of mass conservation states that during any chemical reaction in an isolated system, the total mass of the reactants or starting material must equal the mass of the products. Therefore, in a metabolic network, the change in the concentration of each metabolite over time equals the sum of all reaction rates producing that metabolite minus all reaction rates consuming it. Using the stoichiometric coefficients, the change in a metabolite over time can be written as an ordinary differential equation (ODE):

$$\frac{\mathrm{d}S_i}{\mathrm{d}t} = \sum_{j=1}^{r} n_{ij} v_j$$

Equation 3

Where S_i stands for the concentration of the *i*-th metabolite and v_j as the rate for *j*-th reaction. The symbol *r* denotes the number of reactions and n_{ij} corresponds to the entry at the *i*-th row and *j*-th column of a stoichiometric matrix such as N in Equation 2. Equation 3 can be written as Equation 4 when S_i and v_j are compiled into vectors S and v respectively.

$$\frac{\mathrm{d}\mathbf{S}}{\mathrm{d}t} = \mathbf{N}\mathbf{v}$$

Equation 4

There are two main approaches to modelling a metabolic network: kinetic and structural modelling. Kinetic modelling allows for specific metabolic behaviour, such as reaction rates and concentration, to be captured as each enzymatic reaction turnover in the network is governed by a rate expression. For kinetic modelling, each v for the j-th reaction in Equation 4 corresponds to a reaction rate that depends on the concentration of each metabolite following an enzyme kinetics rate law such as Michaelis-Menten, and v_j can be written as:

$$v_j = \frac{V_{max} S}{K_m + S} \qquad \textbf{Equation 5}$$

Where V_{max} is the limiting rate and K_m is the Michaelis constant. As such, kinetic models provide quantitative insights into the metabolic network by integrating kinetic parameters to describe its biochemical reactions (Morgan & Rhodes, 2002; Rohwer, 2012). This would mean that kinetic models could generate quantitative predictions that are useful for understanding control of flux. Also, kinetic models can be used to simulate a network over a time course, allowing prediction of various metabolite concentrations over time (Morgan & Rhodes, 2002; Poolman et al., 2004; Rohwer, 2012; Schallau & Junker, 2010).

Kinetic models have been used to investigate a number of plant metabolism networks such as the Calvin cycle (Poolman et al., 2004, 2001, 2000) and the biosynthesis of aspartate (Curien et al., 2009) in Arabidopsis (*Arabidopsis thaliana*), sugar metabolism in sugarcane (*Saccharum offinarum)* (Rohwer & Botha, 2001; Uys et al., 2007), choline metabolism in tobacco

(McNeil et al., 2001, 2000), the benzenoid biosynthesis network in petunia flowers (*Petunia hybrid*) (Colón et al., 2010) and monoterpenoid biosynthesis in peppermint (*Mentha x piperita*) (Rios-Estepa et al., 2010, 2008). These models have been used to gain a better understanding of flux distribution control and demonstrate the utility of kinetic models as a tool to guide metabolic engineering strategies in plants. For example, a kinetic model of the benzenoid biosynthesis network was perturbed to mimic transgenic petunia flowers supplied with 150mM phenylalanine over a 4 hour period and was able to predict an increase in the metabolite pool which was in good agreement with their experimental observations (Colón et al., 2010).

However, the major drawback of constructing a kinetic model is in accumulating the kinetic parameters for each reaction in the network. Although literature and online databases such as BRENDA (Schomburg et al., 2013) and SABIO-RK (Wittig et al., 2012) provide vast kinetic information for biochemical reactions, often this information is inadequate to describe a specific biochemical pathway in a specific species. This problem is especially acute for plants. The best approach is to undertake a systematic experimental analysis of kinetic parameters of the relevant enzyme set as was done by Curien et al. (2009), who performed *in vitro* kinetic measurements and incorporated these data into their model to replicate aspartate biosynthesis in Arabidopsis. As a result, they were able to construct a reliable kinetic model and gained an in depth understanding of the functional role of enzyme isoforms and allosteric regulation in the system. However, measuring kinetic properties is time consuming and often *in vitro* kinetic values may not represent those in the intracellular state (Shachar-Hill, 2013). To tackle the issue of kinetic data inadequacy, kinetic

models are often simplified to reduce complexity (Rohwer & Botha, 2001). In this respect, kinetic models are often composed of a small and focused network of reactions, and are not able to provide a wider perspective on the relationship between reactions in pathways. As an example, the aspartate metabolism network contained approximately 13 reactions (Curien et al., 2009), and the benzenoid network kinetic model comprised 31 biochemical reactions (Colón et al., 2010). However, plant systems are complex and composed of many hundreds of reactions - more than can adequately be represented in kinetic models. To add to the complexity, plant cells are compartmentalized and contain transporters that link these spaces together (Shachar-Hill, 2013). For these reasons, a kinetic modelling approach is not suitable for a larger scale network such as the tomato fruit metabolic network which comprises of at least 1500 enzymatic reactions (Bombarely et al., 2011).

Larger scale plant metabolic networks can be constructed and modelled using a structural modelling approach (Sweetlove & Ratcliffe, 2011). In contrast to kinetic models, structural models are built based on reaction stoichiometry and require no knowledge of enzyme kinetics (Dal'Molin & Nielsen, 2013). These stoichiometry data are readily available from species-specific and generic plant metabolic databases such as PlantCyc [http://www.plantcyc.org] for generic plant information, LycoCyc [http://solcyc.solgenomics.net/] for tomato (*Solanum lycopersicum*) (Bombarely et al., 2011); and AraCyc [http://pmn.plantcyc.org/ARA], for Arabidopsis (Zhang et al., 2005). The basis of structural modelling is the steady state hypothesis, where metabolite concentration is constant (Orth et al., 2010). Thus, in this instance, Equation 4

can be written as Equation 6 below, where N represents the stoichiometric matrix and v as the vector of all reaction fluxes.

$$Nv = 0 \qquad \textbf{Equation 6}$$

Structural modelling is constraints-based and one popular approach is FBA (Oberhardt et al., 2009). In addition to mass-balance constraints in FBA which creates a bound in the network, an optimization technique known as linear programming predicts the optimal steady-state metabolic flux distribution (Orth et al., 2010). This provides a platform to explore the metabolic network capabilities by observing the robustness of metabolic networks against internal and external perturbations, and studying plant metabolic network properties (Oberhardt et al., 2009; Shachar-Hill, 2013; Sweetlove & Ratcliffe, 2011).

In modelling, a solution space contains a set of all possible flux distributions within a metabolic network. Without any constraints, however, it is difficult to determine an optimal flux distribution as it may lie at any point in a solution space (Orth et al., 2010). With FBA, the metabolic network is primarily constrained with stoichiometric coefficients that control the flow of metabolites through the network (Orth et al., 2010). Additional constraints such as carbon intake rate or growth rate imposed onto the network further constrain the solution space into a more manageable size for determining an optimal flux distribution. This manageable-sized solution space can then be more effectively searched for the optimal flux distribution, depending on the search interest, or objective function. An objective function is effectively measuring a solution state that is optimally efficient in terms of use of resources. FBA seeks to maximise or

minimise an objective function, such as to maximise the growth rate in order to predict the point that corresponds to the maximum growth rate, or to minimise the intake of carbon to predict the point that corresponds to the minimum carbon uptake rate of a metabolic network, given the constraints applied. However, the solution space is underdetermined as the number of reactions typically exceeds the number of metabolites in a metabolic network. As a result, there is more than one optimal flux distribution that can be found.

FBA has been implemented on a number of plant genome-scale models to explore various biological processes or aspects such as ATP demand constraints for biomass production and maintenance in Arabidopsis (Poolman et al., 2009), photosynthesis and photorespiratory processes in Arabidopsis (Arnold & Nikoloski, 2013; Dal'Molin et al., 2010; Poolman et al., 2000) and maize (*Zea Mays*) (Saha et al., 2011), seed oil accumulation in rapeseed (*Brassica napus*) (Hay & Schwender, 2011b; Pilalis et al., 2011), grain yield in barley (*Hordeum vulgare*) (Grafahrend-Belau et al., 2009), and metabolic responses to varying light intensities in leaf cell of rice (*Oryza sativa*) (Poolman et al., 2013). In this thesis, FBA was chosen as the modelling approach to investigate the underlying metabolic processes during tomato fruit ripening.

1.5 Metabolic engineering

The ultimate goal in understanding metabolic networks is to design successful engineering strategies. Many studies have attempted to manipulate the metabolic network in order to engineer the production of a certain metabolite (DellaPenna, 2001; Milo & Last, 2012). Notable successes in the engineering of

plant metabolism often involve the overproduction of secondary metabolites for their health-promoting effects. For example, the production of the 'purple tomato', where anthocyanins, which exist at low levels in wild type tomatoes, accumulate to high levels due to expression of two transcription factors *Del* and *Ros1* that control expression of enzymes of the anthocyanin biosynthesis pathway (Butelli et al., 2008). Another example is the production of artemisinin, a natural anti-malarial compound from *Artemisia annua*, in tobacco by over-expressing five plant- and yeast- derived genes involved in the mevalonate (MEV) and artemisinin pathways (Farhi et al., 2011). There has been a long history of successful metabolic engineering of microbial organisms, and in several cases, this has involved the transferral of metabolic capabilities from plants, such as the production of artemisinic acid, in yeast (Ro et al., 2006), and the successful overproduction of amorphadiene, also a precursor for artemisinin, following the integration of the MEV pathway into *E. Coli* (*Escherichia coli*) that bypasses its native methylerythritol phosphate (MEP) pathway (Martin et al., 2003). However, integration of the heterologous MEV pathway into *E. coli* resulted in flux imbalances in the pathway, albeit with a significant increase in terpenes, and this led towards the accumulation of hydroxymethylglutaryl-coA (HMG-coA) that is toxic to the cell (Pitera et al., 2007). This problem was overcome by the balanced expression of a second enzyme in the MEV pathway, HMG-coA reductase (HMGR), which relieved the metabolic bottleneck and ensured a high production rate of the final product (Pitera et al., 2007).

The successes in engineering secondary metabolism in both plants and microbes is largely due to the fact that these pathways are at the periphery of

the metabolic network, with only few interconnections to other parts of the network (Sweetlove & Ratcliffe, 2011). This reduces the need to change a large part of the network to compensate for the change in the secondary metabolism and thus reduces any detrimental effect on growth.

However, engineering capability for rational engineering of primary metabolism is important for the synthesis of many industrially important metabolites such amino acids and organic acids. Generally, engineering of primary metabolism has proved rather difficult, although there are isolated successes. For example, in ripening tomatoes, the level of citrate was increased with minimal changes in gross developmental characteristics such as fruit size and number. In that study, introgression lines were used to identify the importance of aconitase activity as a key determinant of fruit citrate level and this was the enzyme targeted in the transgenic plants (Morgan et al., 2013).

Relative to microbial systems, plant systems engineering has had much less success. This is due to the nature of the plant metabolic network, which is more complicated due to its size and compartmentation. In microbial organisms such as *Mannheimia succiniciproducens* (Hong et al., 2004), *E. Coli* (Edwards et al., 2001), *Haemophilus influenza* (Edwards & Palsson, 1999), *Helicobacter pylori* (Schilling et al., 2002), and *Saccharomyces cerevisiae* (Förster et al., 2003), the reconstructed genome-scale metabolic networks consist of 686, 720, 461, 390 and 1175 metabolic reactions respectively. In contrast, the genome-scale metabolic networks for plants such Arabidopsis (*Arabidopsis thaliana*) (Poolman et al., 2009) and maize (*Zea mays*) (Saha et al., 2011) consist of 5253 and 1985 metabolic reactions respectively.

The successes and downfalls of metabolic engineering studies and the complex nature of metabolic networks reaffirms the notion of how tightly metabolic networks are regulated, where a change in the network will perturb other parts of the network. Every attempt at manipulation requires a broader view of the metabolic network, rather than focusing on only a small part of the network. Therefore, gaining a fuller understanding of the metabolic network is important to effectively perturb the system and reduce unanticipated outcomes.

1.6 Summary

The tomato metabolic network consists of hundreds of metabolites, interconnected by hundreds of metabolic reactions and therefore it is likely that the perturbation of one pathway will have an effect on other parts of the network, which may be positive or detrimental to the growth and survival of the organism (Sweetlove & Ratcliffe, 2011). Therefore, the whole network must be considered in order to gain a more in depth understanding of tomato metabolism. Given the size and complexity of the network, assessing the metabolic network is not an easy task, especially without any computational approach such as metabolic modelling.

Chapter 2: Data and Methods

2.1 Sources of data used in this thesis

2.1.1 Modelling software package

All model construction and modelling tasks in this thesis were carried out using ScrumPy, a Python-based software package (Poolman, 2006). ScrumPy contains a number of modules for performing various types of model analysis such as elementary modes analysis and linear programming and the software can be downloaded from [http://mudshark.brookes.ac.uk/ScrumPy]. All relevant modules used in this thesis are in Appendix A.

2.1.2 Modelling prerequisites

Operating system

The operating system used to install ScrumPy was Linux and the Ubuntu 10.4 distribution was used in this thesis.

Python

ScrumPy runs on Python scripting language and Python 2.6 was used in this thesis.

Launching ScrumPy

ScrumPy can be launched through command line by invoking "!ScrumPy".

2.1.3 Tomato metabolic reactions

The tomato metabolic reactions were obtained from the metabolic database LycoCyc and the model constructed in this thesis was based on LycoCyc 3.0. Query and visualisation access of LycoCyc can be done at [solcyc.solgenomics.net] with *Solanum lycopersicum* selected as the organism of choice. The data files used to construct the model was downloaded from [biocyc.org/download.shtml].

2.1.4 Modelling constraints

The data used to constrain the model in this thesis was based from the metabolite profiling data published by Carrari et al. (2006), Baxter et al. (2005) and Valle et al. (1998). Details on how these data is used are explained in Chapter 4.

2.2 Building the model

For this thesis, the model was constructed using the codes in "BuildModel_MC.py" module. Before invoking the functions in the module, a few prerequisites were: a) the LycoCyc 3.0 metabolic database; and b) four modules, namely "Unwanted.py", "Substitutes.py", "Compartmented.py" and "Corrections.spy" were present in the same directory as the model. To begin constructing the model, the two Commands below were run ScrumPy to invoke model building functions from the "BuildModel_MC.py" module:

```
import BuildModel_MC
```
Command 1

BuildModel_MC.BuildModel() **Command 2**

where Command 1 instructed ScrumPy to import the model building module "BuildModel_MC.py" and Command 2 called the "BuildModel" function. By calling the "BuildModel" function, several other functions linked to it are automatically invoked too and these functions are discussed in the following subsections.

2.2.1 Importing reactions from LycoCyc 3.0 and generating a raw model

The first step in model construction using the "BuildModel" function was to import the database LycoCyc 3.0 into ScrumPy. This was done by invoking the "SetUpDB" function, which used the PyoCyc module in ScrumPy to choose the 'lycocyc_3.0' database from the directory. Using the "MakeAll" function in the "BuildModel_MC" module, reactions listed in the "reactions.dat" file in the database were extracted and formed a stoichiometry matrix, the structure for a raw model of the tomato metabolic network.

2.2.2 Correcting reactions or metabolites

Changes to the raw model were done manually by inserting the name of reactions or metabolites in the "Unwanted.py", "Substitutes.py", "Compartmented.py" and "Corrections.spy" modules accordingly. The "Unwanted.py" module lists all reactions and metabolites which were ill-defined (see Chapter 3 for details) and should be removed from the model. To change the directionality of the reactions from its predefined directionality in the

database, the reactions are listed in the “Substitutes.py” module. In this module, any irreversible reactions can be made reversible or reactions predefined as “RIGHT-TO-LEFT” can be changed to “LEFT-TO-RIGHT” (see Chapter 3 for details). The “Compartmented.py” module lists all reactions in the model with appropriate subcellular compartment suffixes to indicate subcellular location. The list can be manually edited to insert or delete any reactions in or out from any compartments. There were four compartments defined in the module – cytosol, plastid, mitochondria, and peroxisome. Reactions with no definitive localisation information were placed in the cytosol by default. Finally, reactions with incorrect stoichiometries were replaced with manually corrected stoichiometries contained in “Corrections.spy”.

Model constructions were done iteratively, where the structure of the model was constructed first, followed by manually editing the model by changing the reactions or metabolite lists in the four modules above, and finally repeating the construction of the model structure with updated changes by using Command 2.

2.2.3 Assembling the model

The “BuildModel” function will generate one module called “Tom_compartmented.spy” that lists all of the reactions in separate compartments. The localisation of reactions and associated metabolites are defined by their suffixes, “_c”, “_p”, “_m” and “_x” corresponding to cytosol, plastid, mitochondria and peroxisome respectively. The “Tom_compartmented.spy” module is not the complete tomato metabolic model

and other modules are needed. This includes the “Transporters.spy” module that lists all of the transport reactions including transport reactions for inputs and outputs of the model and intracellular transporters that allow movement of metabolites between compartments. Other modules needed include “ExtraTom.spy” which lists all reactions, which are manually edited. These included reactions in the chlorophyll degradation pathway, which required manual curation as they were not in LycoCyc 3.0 as well as a generic ATPsynthase used for maintenance costs (see Chapter 3 for details). The final module needed is the “Tom_Vacuole.spy”, which lists all tonoplast transporters that were inserted manually to allow for storage and degradation of metabolites during fruit ripening.

These additional modules were then assembled with the “Tom_compartmented.spy” module by listing the all of these modules in a separate file called “Tom3Comp.spy”, which represent the complete tomato metabolic model.

2.3 Modelling tomato fruit ripening

To load the tomato metabolic model to perform the modelling tasks, Command 3 below is written in ScrumPy:

m=ScrumPy.Model(“Tom3Comp.spy”) **Command 3**

Command 3 loads the tomato metabolic model “Tom3Comp.spy” into ScrumPy and assigns it to “m”. To perform the modelling tasks using linear programming

(LP), an LP object is required. The object was built by invoking the functions using these Commands:

from ScrumPy import LP **Command 4**

lp=LP.lp(m) **Command 5**

Command 4 loads ScrumPy's predefined LP module and Command 5 builds the LP object and assigned it as "lp". The LP object was then used to define an objective function. In this thesis, the objective to minimise the sum of fluxes were used and this was set by:

lp.SetObjDirec("Min") **Command 6**

lp.SetObjective(lp.cnames.values) **Command 7**

Command 6 set the objective to minimise and Command 7 set the objective to minimise all reactions.

To define the constraints specific for each ripening transition, the fluxes of the inputs and outputs are fixed with a specific flux value according to the data obtained from the literature (Baxter et al., 2005; Carrari & Fernie, 2006; Ré et al., 2012; Valle et al., 1998) (see Chapter 4 for details). This was done by:

lp.SetFixedFlux({"reaction_1": 0.12; "reaction_2": 0.24}) **Command 8**

Command 8 constraint a list of input and output reactions with a fixed flux value where “reaction_1”, “reaction_2” and the corresponding flux values are examples of reaction names and values used to constrain the model. In some cases where the flux value of inputs or outputs was required to be different from the data, the command line below is written in ScrumPy:

lp.SetFluxBounds({“reaction_3”: (min_value, max_value)}) **Command 9**

This Command 9 allowed “reaction_3” to carry any flux value within a range of the minimum (min_value) and maximum (max_value) flux value defined. The list of inputs and outputs that defined each ripening transition can be found in Chapter 4.

To find an optimal flux distribution with the objective function and constraints as presented above, Command 10 below is written in ScrumPy:

lp.Solve() **Command 10**

sol=lp.GetPrimSol(AsMtx=True) **Command 11**

sol.Transpose() **Command 12**

Command 11 instructs ScrumPy to retrieve the dataset of the optimal flux distribution found and display it as a matrix, where the columns are the reaction names and the rows are the flux values. The matrix can then be transposed using Command 12 to make analysing tasks easier.

2.4 Modelling lycopene engineering

To model *in silico* engineering of lycopene production in the tomato metabolic network, a module called “LycoScan.py” was used. This module is based on the modelling task performed for the Arabidopsis heterotrophic cell culture where ATPase value were varied and the “ATPScan.py” module was used (Poolman et al., 2009). The “LycoScan.py” module is located in the “Tools” folder in the directory and it contains a function called “LycoScan”. This function allows lycopene accumulation rates (defined by flux value carried by the reaction “LYCOPENE_tx”) to vary within a range and finds an optimal flux distribution using the values within this range, depending on the number of steps defined. The model is also constrained with the inputs and outputs used to model the breaker to turning transition (BR-TU) and these constraints were allowed to vary within a 10% range of its original flux value throughout the varying lycopene accumulation rates (see Chapter 4 for details). The “LycoScan” function was invoked by these Commands below:

import LycoScan **Command 13**

ds=LycoScan.LycoScan (m, min_value, max_value, num_steps) **Command 14**

Command 13 loads the “LycoScan.py” module into ScrumPy and Command 14 calls the “LycoScan” function where “m” is the tomato metabolic model “Tom3Comp.spy”, “min_value” is the minimum lycopene accumulation rate, “max_value” is the maximum lycopene accumulation rate, “num_steps” is the

number of flux distributions required and “ds” represents the dataset of the optimal flux distributions found.

2.5 Flux variability analysis (FVA)

Flux variability analysis was carried using a module called “FVA_MC.py” which contains the “FVA” function. The analysis was carried out separately from the modelling tasks above. The model would need to be loaded first as described by Command 3 in order to perform FVA. Command 15 below is used to load the “FVA_MC.py” module into ScrumPy:

```
import FVA_MC
```
Command 15

The prerequisites of this analysis are an LP object and the constraints of each ripening transition, which can be defined using Commands 4 to 9. To perform the FVA analysis, Command 16 below is written in ScrumPy:

```
ds=FVA_MC.FVA(lp,lp.cnames.values(),“Min”,
lp.cnames.values())
```
Command 16

```
matrix=ds.AsMtx()
```
Command 17

Command 16 calls the “FVA” function, which required four inputs. The first input is the LP object “lp”, the second and third inputs represent the objective function to minimise the sum of fluxes and the fourth input corresponds to the list of reactions that will be analysed. In this thesis, “lp.cnames.values()” was set, which means that all reactions in the model are selected for FVA. Finally, “ds”

corresponds to the dataset generated that can be displayed as a matrix using Command 17. The dataset contains two sets of flux values for each reaction, which correspond to the minimum and maximum flux value allowable within the applied constraints.

Chapter 3: Construction of a tomato metabolic model

3.1 Introduction

This aim of this chapter is to construct a metabolic model that can be used to model the ripening stages of tomato fruit development. A metabolic model can typically be a structural or a kinetic one. However, the latter is unfavourable to model large plant networks such as for tomatoes as the approach requires a large amount of kinetic data to describe its enzymatic reactions (Dal'Molin & Nielsen, 2013). Structural modelling, on the other hand, is built based on stoichiometric data of the enzymatic reactions and no kinetic information is needed (Kauffman et al., 2003; Orth et al., 2010; Sweetlove & Ratcliffe, 2011). Therefore, this approach is preferred to represent unicellular eukaryotes such as yeast (*Saccharomyces cerevisiae*) (Förster et al., 2003), *Mycoplasma gallisepicum* (Bautista et al., 2013) and *Pichia sp.* (Caspeta et al., 2012), and in higher plant metabolic networks such as Arabidopsis (*Arabidopsis thaliana)* (Cheung et al., 2013; Dal'Molin et al., 2010; Poolman et al., 2009), rice (*Oryza sativa*) (Lakshmanan et al., 2013; Poolman et al., 2013), maize (*Zea mays*), rape seeds (*Brassica napus)* and barley seeds (*Hordeum vulgare*).

3.1.1 Model development process

The development of a structural metabolic model generally consist of four phases: 1) Reconstruction of the metabolic network into a draft model; 2) Model refinement; 3) Model testing; and 4) Prospective use (Fell et al., 2010; Ruppin et al., 2010; Thiele & Palsson, 2010). The model development process is an iterative one as the phases are often repeated to improve the predictive

capabilities of the model. Given the increasing availability of annotated genome sequences, metabolic models can be built based on the information in the genome. Therefore, in the first phase of construction for these genome-scale metabolic models involves importing reactions from available metabolic databases that are based on genome annotations such as EcoCyc (Keseler et al., 2013), AraCyc (Zhang et al., 2005), and LycoCyc (Mueller et al., 2005): metabolic databases for *E. coli*, Arabidopsis and tomatoes respectively. These metabolic databases are available to download from the BioCyc database collection website [http://biocyc.org/download.shtml] in various formats and for a wide range of organisms, including plants and microbial organisms (Karp et al., 2005).

The process of importing or listing the reactions to be included in the metabolic model can be done manually or in an automated fashion. Manually listing all the reactions is laborious but it could avoid or significantly decrease the inclusion of ill-defined reactions or metabolites in the model, an issue if the process were fully automated to import all reactions from a metabolic database. This stem from the fact that these metabolic databases are based on genome annotations which contain errors that arise because of incomplete annotation and inconsistencies between different databases used to translate Enzyme Commission (EC) numbers to reactions (Fell et al., 2010; Radrich et al., 2010). The whole construction process of a yeast genome scale model was done manually by listing reactions in the organism by thoroughly examining the literature and entries of pathway databases such as Kyoto Encyclopaedia of Genes and Genomes (KEGG) and Enzyme nomenclature database (Förster et al., 2003). Impressively, the yeast model contains 1175 reactions and 584

metabolites but this construction approach is not suitable for plant metabolic networks, which are larger. Plant metabolic networks typically contain more than 1500 reactions and metabolites, and compartmentation makes it more challenging as plant specific knowledge to distribute reactions across organelles and to identify transporters between the compartments is required (Dal'Molin & Nielsen, 2013). In the yeast genome-scale model, only two compartments were created – the cytosol and mitochondria. For most plant genome-scale models, however, at least five subcellular compartments were integrated namely the cytosol, mitochondria, plastid, peroxisome and the vacuole (Cheung et al., 2013; Dal'Molin et al., 2010; Mintz-Oron et al., 2012; Saha et al., 2011). Therefore, these plant modellers have opted to combine an automated approach to import all of the reactions from specific databases and then manually refine the model to include transporters and removing ill-defined reactions (Cheung et al., 2013; Lakshmanan et al., 2013; Poolman et al., 2013; Radrich et al., 2010). This reduces the time and effort of manually listing more than 1500 reactions and yet allows the modeller to reduce the erroneous annotation in the model manually.

This is important in phase two of model construction as refining the model that includes identifying ill-defined reactions or metabolites, identifying plant specific transporters and identifying missing reactions to ensure biomass synthesis, for example, is not an easy task. This phase usually goes hand in hand with the next phase of model testing as it involves iteratively finding a solution in the metabolic network for a metabolite synthesis problem. This would identify gaps in the metabolic network, the first step in refining the model that leads to time and effort consuming thorough checks across published literature

and online databases for information. However, this step is crucial in ensuring a good quality model with good predictive capabilities. For these reasons, efforts are focused on automating the reconstruction process (Bautista et al., 2013; Henry et al., 2010; Radrich et al., 2010). The Model SEED is a web-based resource [http://www.theseed.org/models/] that provides a model construction pipeline. It performs genome sequence annotations and obtains gene-protein-reaction association to construct an organism-specific reaction network then automates the gap filing process to generate a working draft model, complete with a biomass reaction (Henry et al., 2010). The pipeline has generated 130 genome-scale bacterial metabolic models and each model construction took approximately 48 hours to complete. However, manual curation is still required for these models before they can match most published models in quality and accuracy as the pipeline is not able to collect any experimental data or mend the network gaps resulting from erroneous genome annotation (Henry et al., 2010). Furthermore, model compartmentation is impossible as the pipeline is unable to add any intracellular transport reactions, making this approach further unsuitable for the construction of realistic plant metabolic models. Therefore, there is a need for manual curation efforts in metabolic model construction.

3.2 Results

3.2.1 Building the structural framework of the model

Extracting metabolic reactions from the LycoCyc database

Metabolic reactions were imported from the tomato metabolic database-LycoCyc (Bombarely et al., 2011) into ScrumPy, a Python-encoded module for metabolic modelling (Poolman, 2006). Metabolic databases can be downloaded from BioCyc [http://biocyc.org/]. These metabolic databases, including LycoCyc are available in several data file formats and for this work; attribute-value data files were chosen. These files have the extension '*.dat'. One of these files is 'reactions.dat' which contains all of the reactions in LycoCyc. In 'reactions.dat', each reaction entry has 14 attributes that provide information to convert the reaction in the database into a reaction format that is compatible with ScrumPy (Figure 3.1A). To convert each reaction entry into a ScrumPy compatible format, each reaction in the model is named based on the 'UNIQUE-ID' attribute. Attributes 'LEFT' and 'RIGHT' determine the substrate(s) and product(s) for the corresponding reaction respectively by default. The 'REACTION-DIRECTION' attribute provides information on the reaction directionality to either be; a) 'LEFT-TO-RIGHT' where metabolites in attributes 'LEFT' and 'RIGHT' becomes substrates and products respectively; b) 'RIGHT-TO-LEFT' where metabolites in 'RIGHT' and 'LEFT' becomes substrates and products respectively; and c) 'REVERSIBLE' where the reaction is reversible between metabolites in 'LEFT' and 'RIGHT'. In ScrumPy, reversible reactions are denoted with a ' <>' symbol whereas irreversible reactions are denoted with

a '->' symbol. The stoichiometry coefficients for each reaction were provided by the '^COEFFICIENT' attribute. If there was no information provided from that attribute, the default coefficient was one. Figure 3.1B shows an example of a reaction in ScrumPy.

Removing and correcting ill-defined metabolites and reactions

The next step in building the structural framework of the model was to manually correct or remove ill-defined metabolites and reactions. Ill-defined metabolites are metabolites that are either obscurely described in the database and/or had no associated chemical formula. If the metabolites were described obscurely in the database and no chemical formula was associated with them, these kinds of metabolites are removed from the model. Accordingly, the reactions consisting of these metabolites were also removed from the model. These type of ill-defined metabolites and reactions are listed in a module called 'Unwanted.py' (Appendix A). Meanwhile, if the metabolites had chemical formula associated with them but were obscurely named in the database; they were corrected and remained in the model. Figure 3.2A illustrates an example of obscure metabolites that were corrected and remained in the model. In that example, 'RXN-8025' is a carotene β-hydroxylase reaction which converts β-carotene into β-cryptocanthin and this reaction is part of the carotenoid synthesis pathway. However, this was not clear when looking at the reaction before it was corrected. In the original reaction, metabolites 'CPD1F-129', 'Donor-H2', 'CPD-7409' and 'Acceptor' were not described intuitively (Figure 3.2A). Crosschecking the reaction with other plant metabolic databases through MetaCyc [http://www.metacyc.org/] showed that 'CPD1F-129' and 'CPD-7409'

were β-carotene and β-cryptoxanthin respectively and that ‘Donor-H2’ and 'Acceptor’ were NADH and NAD^+ respectively.

Another type of database curation of metabolic names that is problematic to the model construction is having multiple names for the same metabolite. For example, "D-Glucose", "ALPHA-GLUCOSE" and "GLC" in LycoCyc all correspond to glucose. In this case, "GLC" was chosen to represent glucose and "D-Glucose", "ALPHA-GLUCOSE" were substituted with "GLC" in the model. This was done for each metabolite with multiple names.

Another type of metabolite in the database that needed attention when constructing the model was "NAD-P-OR-NOP" and "NADH-P-OR-NOP" which represented $NAD(P)^+$ and NAD(P)H respectively. Reactions containing these metabolites can either use NAD^+ or $NADP^+$ as an electron acceptor and NADH or NADPH as an electron donor. In the model, these reactions were split into two reactions: a) an NAD^+ dependent reaction and a "-(NAD)" suffix was appended to the reaction name; and b) an $NADP^+$ dependent reaction and a "-(NADP) suffix was appended to the reaction name. An example is of “RXN-7979”, a zeaxanthin epoxidase which can either use NAD^+ or $NADP^+$ to convert zeaxanthin into antheraxanthin. For modelling purposes, this reaction exists as “RXN-7979-(NAD)” and “RXN-7979-(NADP)” in the model to denote NAD- and NADP-dependent zeaxanthin epoxidases respectively.

3.2.2 Compartmentation of the tomato metabolic model

The tomato model consists of five subcellular compartments

In the tomato model, metabolites and corresponding reactions were assigned to five subcellular locations – cytosol, mitochondrion, plastid, peroxisome and vacuole. The metabolites and reactions in these compartments were differentiated by adding suffixes to the metabolite and reaction names, "_c" for cytosol, "_m" for mitochondria, "_p" for plastid, "_x" for peroxisome and "_v" for vacuole. Compartmental assignment was made based on the compartmentation of the Arabidopsis genome-scale model (Cheung et al., 2013). Information for compartmentation in this model was obtained from the literature and the SUBA database (Heazlewood et al., 2007; Tanz et al., 2013). Reactions with no reliable information on subcellular localisation were assigned to the cytosol.

Transport reactions between compartments

Transport steps that enabled metabolite exchange between subcellular compartments are not included in the LycoCyc metabolic database. Thus, these transport reactions were included manually based on information obtained from published literature on plant transporters (Bush, 1993; Simkin et al., 2011; Weber & Linka, 2011).

3.2.3 Manually curating the chlorophyll degradation pathway for the tomato model

Chlorophyll degradation is one of the prominent metabolic changes that occur during the transition of chloroplast into chromoplast in ripening tomato fruits. Accordingly, the pathway for chlorophyll degradation is required to model the tomato fruit ripening stages in this work. However, unclear information surrounding the end product of this pathway posed a challenge. It has been established that one class of end products of chlorophyll degradation are the non-fluorescent chlorophyll catabolites (NCCs), formed from the tetrapyrrole ring (Hörtensteiner & Kräutler, 2011; Oberhuber et al., 2003). From the perspective of model construction, NCCs are regarded as orphan metabolites as they are not metabolised anywhere else in the network. This in turn created a gap in the tomato metabolic network as the carbons from the degraded chlorophylls are not used to produce any intermediates towards the accumulation of other required metabolites during ripening. As well as the tetrapyrrole ring, chlorophylls also contain a phytol chain which can be degraded (Ischebeck et al., 2006). However, the information on the fate of phytol in plants is unclear. In LycoCyc, the phytol salvage pathway (LycoCyc pathway reference: PWY-5107), was shown to produce vitamin E and tocopherol. Interestingly, in animals, it has been shown that phytol can be degraded into acetyl-coA through the phytanic acid degradation pathway (Verhoeven & Jakobs, 2001; Wanders et al., 2003). In addition, it was suggested that the phytol degradation pathway via phytanic acid found in mammals were similar to plants as a homolog of PAHX gene was found in Arabidopsis (Araújo et al., 2011). The identification of this gene in tomato

(LycoCyc gene reference: SOLYC05G007970.2) further corroborates this finding. Therefore, the phytanic acid degradation pathway was manually added to the tomato metabolic network. The pathway consisted of the α-oxidation of phytanic acid into pristanoyl-coA, which in turn is converted into acetyl-coA and propionyl-coA through β-oxidation in the peroxisome. This allowed acetyl-coA to join the glyoxylate cycle in the peroxisome and propionyl-coA to be imported into the mitochondria to join the TCA cycle via succinyl-coA.

3.2.4 General model properties

The tomato metabolic model based on LycoCyc 3.0 has a total of 2500 reactions, which consist of 1720 cytosolic reactions, 357 plastidic reactions, 93 mitochondrial reactions, 38 peroxisomal reactions, 31 vacuolar reactions, 176 intracellular transport reactions, and 85 model-defined external transporters that include the transport of metabolites constrained as inputs and outputs. As for metabolites, the model has a total of 2366 metabolites where 1822 are in the cytosol, 123 are in the mitochondria, 347 are in the plastid, 58 are in the peroxisome and the remaining 16 in the vacuole.

(A) Reaction entry from LycoCyc

```
UNIQUE-ID - GALACTOKIN-RXN
ORPHAN? - :NO
EC-NUMBER - 2.7.1.6
MEMBER-SORT-FN - NUMBERED-CLASS-SORT-FN
REACTION-DIRECTION - LEFT-TO-RIGHT
IN-PATHWAY - PWY-3821
IN-PATHWAY - COLANSYN-PWY
IN-PATHWAY - GALACTMETAB-PWY
COMMON-NAME - Galactokinase
ENZYMATIC-REACTION - ENZRXN8JW-7514
ENZYMATIC-REACTION - ENZRXN8JW-7165
ENZYMATIC-REACTION - ENZRXN8JW-6740
ENZYMATIC-REACTION - ENZRXN8JW-5922
ENZYMATIC-REACTION - ENZRXN8JW-4123
ENZYMATIC-REACTION - ENZRXN8JW-3859
OFFICIAL-EC? - T
TYPES - EC-2.7.1
TYPES - Small-Molecule-Reactions
LEFT - |D-Galactose|
^COEFFICIENT - -1
LEFT - ATP
^COEFFICIENT - -1
RIGHT - GALACTOSE-1P
^COEFFICIENT - 1
RIGHT - ADP
^COEFFICIENT - 1
```

(B) Reaction in ScrumPy

```
"GALACTOKIN-RXN":

      1.0 "D-Galactose" + 1.0 "ATP" -> 1.0 "GALACTOSE-1P" + 1.0 "ADP"

      ~
```

Figure 3.1. Example of a reaction entry from LycoCyc. (A) shows an example of a reaction entry as it is imported from LycoCyc while (B) shows how the same reaction in ScrumPy. Each reaction entry typically has 14 attributes. ScrumPy takes into account five of these attributes, which are the 'UNIQUE-ID', 'REACTION-DIRECTION', 'LEFT', 'RIGHT' and '^COEFFICIENT'. 'UNIQUE-ID' provides the unique LycoCyc reference for that reaction. 'REACTION-DIRECTION' provides the direction of the reaction, which in this case is 'LEFT-TO-RIGHT' indicating the reaction produces the metabolite in the 'RIGHT' field ('GALACTOSE-1P') from the metabolite in the 'LEFT' field ('|D-Galactose|').

(A) In LycoCyc:

```
'RXN-8025':

      1.0 'CPD1F-129' + 1.0 'OXYGEN-MOLECULE' + 1.0 'Donor-H2'->

      1.0 'CPD-7409' + 1.0 'WATER' + 1.0 'Acceptor'
```

(B) In the model:

```
'RXN-8025_p':

      1.0 'BETA-CAROTENE_p' + 1.0 'OXYGEN-MOLECULE_p' + 1.0
      'NADH_p'-> 1.0 'BETA-CRYPTOXANTHIN_p' + 1.0'WATER' + 1.0
      'NAD_p'

      ~
```

Figure 3.2. An example of a corrected reaction which was ill-defined in LycoCyc. 'RXN-8025' represent β-carotene hydroxylase in LycoCyc. However, it was obscurely annotated by using metabolites such as 'Donor-H2', 'Acceptor' and 'CPD-7409'. Crosschecking with other plant metabolic databases such as PlantCyc and the literature, the reaction was corrected as (B).

3.3 Discussion

3.3.1 The model is intended to investigate the known processes linked to tomato fruit ripening

All metabolic models can vary according to their intended functional role. In this work, the tomato metabolic model was constructed to investigate the processes that are known to occur during the ripening stage. Therefore, this model was curated to enable the model to degrade and accumulate all of the important metabolites during fruit ripening. One example to demonstrate this was the manual curation of the chlorophyll degradation pathway. As the transition of chloroplast to chromoplast was established as one of the prominent processes that occurred during tomato fruit ripening (Egea et al., 2011), it was important that this tomato metabolic network was able to degrade chlorophyll into intermediates that are useful for the accumulation of other important metabolites of ripening. Manually adding and curating a pathway or group of reactions in a model to suit the needs to replicate a specific biological process *in silico* was also shown for the Arabidopsis model *i*AT1475 (Chung et al., 2013). They have updated the Arabidopsis model *i*RS1597 (Saha et al., 2011) by manually including the reactions for the biosynthesis of terpenoid backbone, monoterpenoids, diterpenoids, triterpenoids, tetraterpenoids and sesquiterpenoids (Chung et al., 2013).

The ability to model secondary metabolism is also important in this metabolic network as the ripening process involves the degradation and accumulation of a range of carotenoids (Baxter et al., 2005; Carrari et al., 2006).

The degradation and accumulation of these carotenoids in addition to other metabolites require the fluxes from both central and secondary metabolism. Typically, most published plant models were utilised to produce biomass components such as amino acids, nucleic acids, and carbohydrates, which only involved the central metabolism (Dal'Molin et al., 2010; Poolman et al., 2013, 2009; Saha et al., 2011). This has been shown for the Arabidopsis (Dal'Molin et al., 2010) and rice (Poolman et al., 2013) models which were used to depict photosynthesis, photorespiration and respiration. Few plant models have included the synthesis of secondary metabolites. Examples include C4Gem (Dal'Molin et al., 2010) and the updated Arabidopsis (Chung et al., 2013; Mintz-Oron et al., 2012) models, which included the synthesis of vitamins and terpenoids respectively. However, it should be noted that the secondary metabolism curated in this tomato metabolic model is only limited to the degradation and production of a selected range of carotenoids such as lycopene, β-carotene, zeaxanthin, lutein, antheraxanthin and neoxanthin in accordance to the need of these metabolites during the ripening stages that were modelled (Baxter et al., 2005; Carrari et al., 2006). If the reactions in the pertinent pathways are added manually, the tomato metabolic network can also degrade and produce other classes of terpenoids.

In order to closely mimic the processes that occurred during ripening, the number of constraints used to model the tomato ripening stages was more than what was typically used to model other plant networks. In this work, degradation and accumulation rates of a range of metabolites were used as inputs and outputs respectively. These rates were obtained from published metabolite profiling data, which provided degradation and accumulation rates for more than

30 metabolites (Baxter et al., 2005; Carrari et al., 2006). For example, to model the transition between mature green and breaker stages of ripening, 14 metabolites were degraded as inputs and 38 metabolites accumulated as outputs. In most plant models, meanwhile, there are typically only one to five inputs and one biomass reaction as an output. A biomass reaction may consist of more than 10 metabolites that are produced in an experimentally observed proportion. For example, to model the photosynthesis, photorespiration and respiration in Arabidopsis, only inputs of CO_2, sucrose and photons were used to produce a range of carbohydrates, sugars, cell wall components, amino acids, nucleotides and fatty acids that were combined in one biomass reaction (Dal'Molin et al., 2010). In this work, however, instead of including all outputs into one biomass reaction, the output metabolites were assigned an individual transporter. This was to allow the output fluxes to be set independently. This was also done for the rice model as it provided not only a more convenient mechanism but also a prerequisite to investigate variations in biomass composition (Poolman et al., 2013).

3.4 Summary

The main goal of this chapter was to construct a metabolic model of a tomato fruit, which was intended to model the processes that are known to occur during ripening. The model has a total of 2500 reactions and 2366 metabolites which are distributed into five compartments. The current model is able to degrade and accumulate more than 30 metabolites that include sugars, amino acids, organic acids, and carotenoids. However, the limitation of the model is that it is not able to produce or degrade larger terpenes and fatty acid

due to lack of information available or it was not one of the required metabolites for the ripening process. Further work needs to be done to further refine the model to exclude ill-defined metabolites and reactions that may have been overlooked in this work. Nevertheless, this model can be used to investigate the underlying processes during ripening and serves as a platform for further development to suit other physiological processes in the tomato that can be modelled.

Chapter 4: Modelling metabolic changes during the ripening stages of tomato fruit development

4.1 Introduction

The aim of this work was to model the metabolic states that occur at different stages of tomato fruit ripening using the metabolic model constructed in Chapter 3. Ripening is a complex process involving a series of changes in fruit chemical composition due to degradation and synthesis of a number of soluble and volatile metabolites (Baxter et al., 2005; Carrari et al., 2007, 2006). The degradation and synthesis of these important determinants of fruit flavour arise from interconnected processes in the fruit metabolic network. In order to gain a better understanding of the metabolic changes during tomato fruit ripening, a number of questions need to be addressed including: (a) which metabolic processes are involved; (b) how these processes link with each other to orchestrate the accumulation and degradation of specific metabolites; and c) whether there are differences in these underlying metabolic processes during on- and off-vine ripening. Due to the complexity of the metabolic network involved, these answers are intuitively impossible to elucidate without a computational approach such as mathematical modelling (Steuer, 2007).

Tomato fruit ripening consists of a number of well-defined phases in which there are pronounced differences in metabolic behaviour (Giovannoni, 2004; Klee & Giovannoni, 2011). One modelling approach that is able to simulate and capture such dynamic metabolic behaviour is kinetic modelling. Kinetic models provide quantitative insights into the metabolic network by integrating enzyme kinetic parameters to describe its biochemical reactions

(Morgan & Rhodes, 2002; Rohwer, 2012). These models can generate quantitative predictions that are useful for understanding control of flux. Also, kinetic models can be used to simulate a network over a time course, allowing prediction of metabolite concentrations over time (Morgan & Rhodes, 2002; Poolman et al., 2004; Rohwer, 2012; Schallau & Junker, 2010). Kinetic models have been successfully used to investigate the dynamic behaviour of a number of small-scale plant metabolic networks in Arabidopsis (*Arabidopsis* thaliana) (Curien et al., 2009; Poolman et al., 2004, 2001, 2000), sugarcane (*Saccharum offinarum*) (Rohwer & Botha, 2001; Uys et al., 2007), tobacco (McNeil et al., 2001, 2000), petunia flowers (*Petunia hybrid)* (Colón et al., 2010), and peppermint (*Mentha x piperita*) (Rios-Estepa et al., 2010, 2008). However, these models are often simplified or limited to a small-scale, as the kinetic modelling approach requires kinetic measurements for each enzyme in the network which are difficult to obtain. For this reason, large-scale metabolic networks such as those in plants are difficult to decipher using kinetic modelling approaches due to lack of large-scale kinetic data.

In this work, Flux Balance Analysis (FBA) was chosen as the modelling approach to model the ripening stages of the tomato fruit. In contrast to the kinetic modelling approach, FBA does not require any kinetic measurements to describe its reactions. Instead, the approach is based on a matrix of reaction stoichiometries and is constrained using mass balancing and input or output constraints (Kauffman et al., 2003; Orth et al., 2010; Sweetlove & Ratcliffe, 2011). FBA has been widely used to model large-scale plant metabolic networks in Arabidopsis (Cheung et al., 2013; Dal'Molin et al., 2010; Mintz-Oron et al., 2012; Poolman et al., 2009; Williams et al., 2010), maize (*Zea mays*)

(Dal'Molin et al., 2010; Saha et al., 2011), rapeseed (*Brassica napus*) (Hay & Schwender, 2011a, 2011b; Pilalis et al., 2011), barley seed (*Hordeum vulgare*) (Grafahrend-Belau et al., 2009), and more recently rice (*Oryza sativa*) (Lakshmanan et al., 2013; Poolman et al., 2013). However, one of the limitations of FBA relates to its ability to capture the dynamic behaviour of metabolism as FBA analysis requires a metabolic steady state (Sweetlove & Ratcliffe, 2011).

An extension to FBA that allows the integration of dynamic properties to the static characteristics of FBA is known as dynamic flux balance analysis (DFBA). DFBA was first introduced by Mahadevan et al. to simulate the metabolic network reprogramming behaviour during diauxic growth in *Escherichia coli* (Mahadevan et al., 2002). In that study, kinetic expressions were incorporated to accommodate time and metabolite concentration dependencies. They also incorporated rate of change constraints on the metabolic fluxes to describe the metabolic network reprogramming during diauxic growth. These rates were estimated from transcription and translational rates, obtained from published literature (Mahadevan et al., 2002). Although the study simplified the metabolic network to only four pathways (85 reactions), the approach demonstrated that it was possible to simulate the dynamic behaviour of the metabolic network with a structural model. DFBA does not require kinetic measurements for all reactions in the network, instead the formalism allows the incorporation of kinetic expressions when the kinetics are well characterized. In this example, kinetic measurements were used to describe the uptake of glucose (Mahadevan et al., 2002).

In addition to *Escherichia coli* (Mahadevan et al., 2002; Meadows et al., 2010), DFBA models have been developed to describe the dynamic metabolism of microrganisms such as *Saccharomyces cerevisiae* (Ghosh et al., 2011; Jouhten et al., 2012), *Bordetella pertussis* (Budman et al., 2013), *Pichia pastoris* (Calık et al., 2011) and a co-culture of *Saccharomyces cerevisiae* and *Scheffersomyces stipitis* (Hanly & Henson, 2013). The DFBA approach has been shown to be useful to simulate batch fermentation (Budman et al., 2013; Ghosh et al., 2011; Meadows et al., 2010) and predicted an increase of 24.7% in ethanol production in microaerobic *S. cerevisiae* with an engineered cofactor balanced pathway (Ghosh et al., 2011). In that study, they modified a published genome-scale model of *S. cerevisiae* (iMM904) (Mo et al., 2009) by introducing an engineered cofactor-balanced pentose sugar utilizing pathway. DFBA was used to predict the optimal flux distribution to increase the production of ethanol from glucose, D-xylose, and L-arabinose in engineered cofactor-balanced and -imbalanced pathway models. They showed that the approach was able to predict ways to optimize the utilization of pentose sugar to increase biofuel production within a shorter period of time in the strain with an engineered cofactor-balanced pathway. The predictions were shown to have good agreement with experimental findings and suggested a strategy of changing enzyme cofactor specificity for improved pentose sugar utilisation efficiency and increased ethanol production in *S. cerevisiae* (Ghosh et al., 2011).

However, using DFBA to model complex plant systems is still a challenge. Only two studies have reported this approach as the basis for their modelling technique in plants (Grafahrend-Belau et al., 2013; Luo et al., 2009). Luo et al (2009) introduced a method called M_DFBA, which is an extension of

the DFBA formalism by combination with a method called Minimisation Of Metabolic Adjustment (MOMA) - an optimization technique that finds a flux distribution that is the closest to the flux distribution of the wild type strain, assuming that the wild type has the optimal flux configuration (Segrè et al., 2002). Using two methods; a) M_DFBA and b) DFBA, they modelled photosynthetic metabolism in the chloroplast of C3 plants. They compared model predictions from the two methods and found that the M_DFBA method predictions were closer to the experimental observations than the DFBA predictions. However, the paper did not discuss any observations from the flux distribution predicted using DFBA and the photosynthetic metabolic model in that study was simplified to only five reactions in order to obtain an optimal flux distribution using M_DFBA, which suggests the limitations of the latter approach (Luo et al., 2009).

In another plant systems study, Grafahrend-Belau et al (2013) modelled a whole barley plant using Multiscale Metabolic Modelling (MMM) method, which is based on DFBA (Grafahrend-Belau et al., 2013). They combined a multi organ FBA model – which consisted of phloem, leaf, stem, and root static FBA models – with a dynamic process network model (ProNet-CN) (Grafahrend-Belau et al., 2013; Muller et al., 2012). Using a DFBA approach, the model is divided into several time points. The dynamic process model (ProNet-CN) predicted the carbon and nitrogen exchange fluxes, which constrained the multi organ FBA model at the beginning of each time interval. This allows the static multi organ FBA to be computed at each time interval within a dynamic constraint. As a result, a series of spatio-temporal snapshots of the multi organ FBA can be predicted. In that study, they have shown that the

model was able to predict a sink-to-source shift of barley stem metabolism at 64 to 65 days after sowing (DAS) as a result of a decline in leaf source capacity which in turn decreased the loading of sucrose from the phloem. The observation was found to be in good agreement with the literature (Grafahrend-Belau et al., 2013). Furthermore, they showed that it is possible to overcome the lack of kinetic measurements for substrate uptake rates to describe the dynamics of the individual FBA organ models by generating dynamic constraints in the form of exchange fluxes from the dynamic ProNet-CN model (Grafahrend-Belau et al., 2013). The required parameters needed to supply carbon fluxes and nitrogen fluxes to the dynamic ProNet-CN model were leaf-area-based concentrations, chlorophyll content, photosynthesis rate, and glucose, fructose, sucrose, starch, and fructan content in leaves, which they were able to obtain through greenhouse experiments and ontogenetic course data from published literature (Muller et al., 2012). The MMM approach was shown to be successful in investigating the source-sink metabolism in barley plant.

However, in respect to the biological question that needs to be addressed in this study, which is to investigate the underlying metabolic changes during ripening, a DFBA modelling approach is not the best. Firstly, DFBA integrates kinetic measurements to describe the uptake or output fluxes for the model. In the previous example of DFBA modelling in *S. cerevisiae*, kinetic measurements were required to describe the uptake of only three substrates whereas the MMM approach coupled a process-network model to generate input rates for its multiorgan FBA model. In addition, kinetic information for microbial organisms is more widely available than for plants. On

the other hand, my study has more than 70 inputs and outputs that create boundaries in the metabolic network to model the ripening stages. These constraints would have to follow a kinetic law such as Michaelis-Menten to model the dynamics according to DFBA. This would mean that large sets of kinetic measurements would need to be obtained, a limitation that can be avoided by using a purely static approach such as FBA. Secondly, the DFBA approach would divide the ripening stages into several time intervals, concatenate them and solve the model at the beginning of each time interval. This would also mean that the outputs predicted from the previous timepoint would constrain the flux distribution prediction of the next timepoint, resulting in a pileup of possible prediction errors. In my work, I am able to avoid such pileup by modelling each stage of ripening discretely, using different sets of constraints specific for each stage.

Consequently, the tomato-fruit-ripening stages in this study were modelled using a static FBA approach by sub-dividing the ripening into discrete temporal transitions and using different sets of metabolite degradation and accumulation rates as constraints for each transition. These constraints were obtained from metabolite abundance data from tomato fruit developmental metabolic profiles obtained from the literature (Carrari et al., 2006). By calculating the difference in metabolite abundance between each stage, it was possible to generate a constraint as to how the rate at which each metabolite must accumulate or be consumed. The rates were calculated by dividing the change from one time point to another by seven days (seven-day intervals were used in the study). This enables the ripening stage to be modelled in two transitions: i) mature-green to breaker (MG-BR); and ii) breaker to turning (BR-

TU), which used the degradation and accumulation rates based on the change between mature-green (49 DAA) to breaker (56 DAA) and breaker (56 DAA) to turning (63 DAA) stages developmental timepoints respectively (Figure 4.1). In this context, citrate for example, becomes an ouput as it must accumulate during mature green to breaker transition and becomes an input when it must be consumed during breaker to turning transition (Figure 4.1).

Metabolic changes during ripening were analysed by comparing the flux distributions between these two ripening transitions, assuming that each ripening transition is in steady-state with no flux fluctuation. That assumption is based on the fact that a single-point snapshot at the mid-point between the two ripening stages is modelled and hence the changes in metabolite concentrations are assumed to be minimal, and a pseudo setady-state can be assumed. With that in consideration, metabolite degradation and accumulation rate is also assumed to be linear between these stages. An objective function of minimization of total flux was used for these modellings. This objective function represents a flux state that is optimally efficient in terms of use of resources. In effect, the flux distribution is that which minimises the investment in enzymes. This objective function has been shown to lead to accurate predictions of fluxes for plant systems (Cheung et al., 2013).

One hypothesis of this thesis is that there are underlying metabolic differences between on- and off-vine ripening. It is known that ripening can proceed when a mature green fruit is removed from the plant, and indeed this is standard commercial practice (Arias et al., 2000; Oms-Oliu et al., 2011; Ré et al., 2012). However, tomatoes that are ripened off the plant do not taste the

same as tomatoes ripened on the vine (Bisogni et al., 1976). It has also been reported that total soluble metabolites differ in on- and off-vine tomatoes (Arias et al., 2000; Ré et al., 2012). This is likely to have consequences for flavour and the overall quality of the fruit (Arias et al., 2000; Bisogni et al., 1976; Malacrida et al., 2006). Accordingly, to investigate the underlying metabolic differences between on- and off-vine ripening, the ripening stages were modelled in an open and closed system. An open system allows flux of metabolites from the phloem into the fruit as additional inputs, modelling an on-vine ripening condition. Meanwhile, a closed system does not allow additional input flux and the system uses only its internal metabolite pool, modelling an off-vine ripening condition. Using the model constructed in Chapter 3, it was possible to uncover how the network is able to degrade and accumulate a range of important metabolites within an open and closed system.

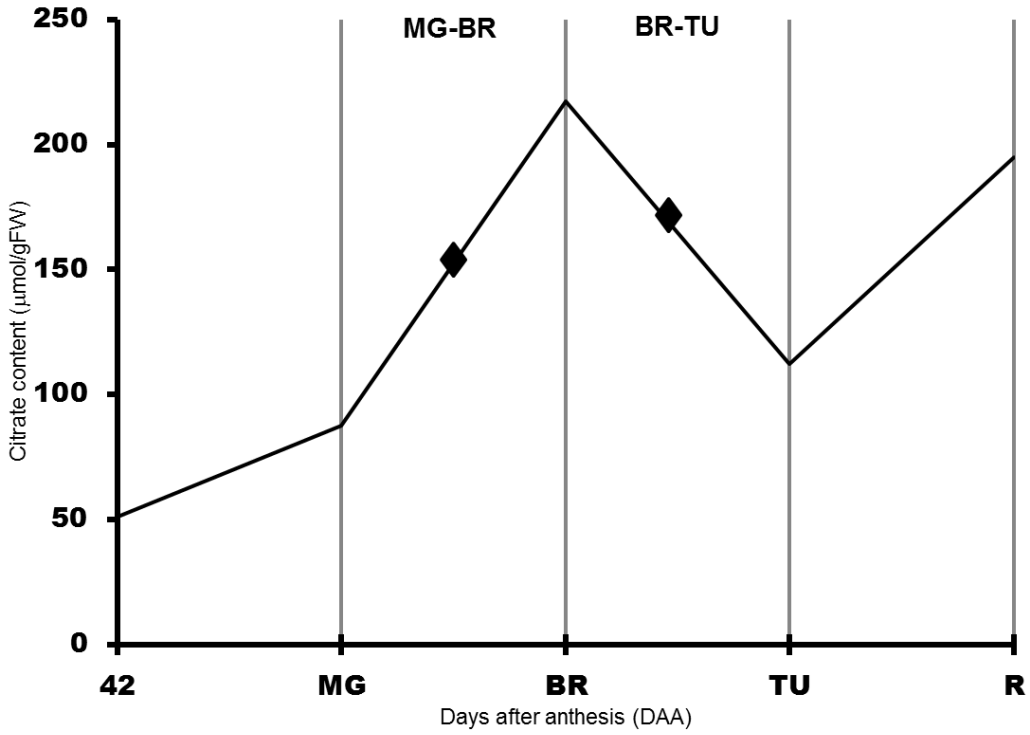

Figure 4.1. Changes in citrate levels during tomato fruit ripening. An illustration of the changes in metabolite (e.g citrate) concentration for each stage of ripening is shown. Abbreviations are as follows; MG- mature green stage; BR- breaker stage, TU- turning stage; R-ripe stage, MG-BR – mature green to breaker transition; and BR-TU – breaker to turning transition. Each stage is within 7-day intervals, which corresponds to 49, 56, 63 and 70 DAA for MG, BR, TU and R respectively. Black diamonds represent single-point snapshots of the corresponding transition where metabolite concentration changes were assumed to be minimal and a pseudo-steady state can be assumed when modelling.

4.2 Results

4.2.1 Modelling approach

Metabolic constraints: obtaining metabolite accumulation and degradation rates

The tomato metabolic model was used to observe changes between mature green to breaker and breaker to red ripening stages. To model each transition between these ripening stages, the metabolic network was constrained with a specific set of degradation and accumulation rates, which were obtained from metabolic profiling and protein measurement studies in tomato fruits (Baxter et al., 2005; Carrari et al., 2006; Ré et al., 2012; Valle et al., 1998). Carrari *et al.* (2006) provided a comprehensive metabolite accumulation data during tomato fruit development for 70 days after anthesis (DAA) with 7 days interval between each time point (Carrari et al., 2006). However, these data were provided only in relative units. In another study, Baxter *et al.* (2005) provided metabolite accumulation data during tomato fruit development in absolute values (μmol/gFW) but for only five time points during the development. Only two of those time points were marked clearly for the ripening stages, which were for breaker and ripe stages (Baxter et al., 2005). In order to get absolute values for all stages during ripening which includes stages from mature green, breaker and turning, the relative data from Carrari *et al.* (2006) were converted into absolute values by comparing them with a common developmental time point, which is the breaker stage in the study by Baxter *et al.* (2005). This provided a set of metabolite accumulation data in absolute values (μmol/gFW) for three time points during ripening, representing mature

green, breaker and turning stages of ripening. Metabolite accumulation and degradation rates were then calculated by dividing the change from one time point to another by seven days based on the interval used in Carrari *et al.* (2006). As a result, two sets of accumulation and degradation rates (in units of μmol/gFW/day) describing the transition between mature green to breaker stages (MG-BR) and between breaker to turning (BR-TU) were obtained.

Metabolic constraints: obtaining protein degradation rates

Protein degradation was taken into account when modelling MG-BR and BR-TU. Ré et al. (2012) provided protein measurement data for different time points during on-vine tomato fruit ripening (Ré et al., 2012). Protein degradation rates were calculated by dividing the change of protein content at different time points with seven days and this provided two protein degradation rates for MG-BR and BR-TU respectively (Ré et al., 2012). To convert these protein degradation rates into amino acid degradation rates, the average amino acid composition of fruit protein was required. There was no information on amino acid composition for tomato fruits in the literature and instead, amino acid composition measured for Arabidopsis was used (Williams et al., 2010). These sets of amino acid accumulation and degradation rates were then merged with the amino acid accumulation and degradation rates obtained from the Carrari et al. (2006) and Baxter et al. (2005) studies (Baxter et al., 2005; Carrari et al., 2006).

Metabolic constraints: obtaining amino acid composition for modelling on-vine ripening

As the phloem provides the fruit with amino acids in addition to sugars during on-vine ripening, it is important that the tomato metabolic network allows additional influx of amino acids when modelling on-vine ripening. In order to do that, phloem amino acid composition data were obtained from a study that extracted tomato plant phloem sap and the top five most abundant amino acids in the phloem were chosen to be included in the model (Valle et al., 1998). These five amino acids were glutamate, phenylalanine, aspartate, glutamine and threonine and they were grouped into one transporter reaction (amino acids_phloem) for modelling purposes and this transporter was allowed to carry flux when modelling on-vine ripening.

Modelling MG-BR and BR-TU

MG-BR and BR-TU each has a specific set of degradation and accumulation rates. Degraded metabolites were made as inputs whereas accumulated metabolites were made as outputs for the tomato metabolic model. An objective function to minimise the sum of fluxes was used when modelling MG-BR and BR-TU as the objective function was shown to lead to accurate predictions of fluxes for plant systems (Cheung et al., 2013). To model MG-BR, each input and output was fixed with the corresponding degradation and accumulation rate value as listed in tables 4.1 and 4.2. An exception was made for cysteine degradation. When a fixed degradation rate value was assigned to each constraint including cysteine, the model could not find an optimal flux distribution that satisfied the objective function within the applied constraints. This is due to the sulphur containing metabolites, methionine and

cysteine, that were constrained during this transition. As the experimental flux for methionine had a higher degradation rate than the accumulation rate of cysteine, this created an imbalance for the sulphur flux in the network (ie the sulphur produced during this transition by methionine was not able to be consumed by cysteine). As a result, cysteine degradation rate was allowed to vary with a minimum rate of 0.0001 μmol/gFW/day and no maximum flux value boundary. This was to force the cysteine degradation transporter to carry a non-zero flux during modelling. This action enabled the model to find an optimal flux distribution when modelling MG-BR. The same strategy was applied to model BR-TU, where each input and output was fixed with the corresponding degradation and accumulation rate value as listed in tables 4.3 and 4.4, but with exceptions for caffeate, neoxanthin and myoinositol-1-phosphate degradation. An optimal flux distribution that satisfied the objective function within the applied constraints could not be found when a specific degradation rate value was fixed for these metabolites during BR-TU. As a result, the three metabolites were allowed to degrade within a range. Like the modelling approach used in MG-BR, a minimum degradation rate of 0.0001 μmol/gFW/day was used to force non-zero flux through input transporters carrying caffeatte, neoxanthin and myoinositol-1-phosphate during BR-TU.

Open and closed systems

Both MG-BR and BR-TU were modelled in a closed (no influx of sugars and amino acids from the phloem) and open (influx from the phloem allowed) system to depict off- and on-vine ripening conditions, respectively. In open system modelling, ‘open’ transporters, which supplied metabolites from the phloem, were allowed to carry flux and were represented as additional inputs to

the model. Meanwhile, in a closed system modelling, these ‘open’ transporters were not allowed to carry any flux, thus blocking any additional inputs from entering the metabolic network. Furthermore, there are another five additional metabolite transporters that could carry flux in these models. Three of these transporters carry an influx of oxygen, phosphate and sulphate, which were allowed to carry flux during both transitions. The remaining two transporters carried efflux of carbon dioxide for both stages and non-fluorescent chlorophyll catabolites (NCCs) during MG-BR only. This extra sink transporter that accumulates NCCs was to create carbon balance in the network since we could find no evidence that these NCCs are further degraded. These additional transporters were allowed to carry free flux, meaning that these transporters were not constrained to any specific flux values.

Main metabolic changes during tomato fruit ripening

Tomato fruits initially contain chloroplasts that are photosynthetically active, but these differentiate to non-photosynthetic chromoplasts during the ripening process (Egea et al., 2011). As ripening proceeds to breaker stage, carotenoids begin to accumulate in tomato fruits, which bring out the red colour typical of tomatoes. Soluble sugars also increase from mature green to breaker stage. This increase in soluble sugars is thought to result from starch degradation from pre-ripening stages (Baxter et al., 2005). GABA, one of the abundant amino acids in tomatoes, is rapidly degraded after the breaker stage (Yin et al., 2010).

4.2.2 Flux Variability Analysis (FVA)

Flux variability analysis (FVA) was carried out on both ripening stages to identify variable fluxes in the model flux distributions. Figure 4.2 presents a summary of the results obtained from FVA for both of the ripening stages. The Venn diagrams in Figure 4.2 represent all of the reactions that carried flux during the modelling of MG-BR and BR-TU. This group of reactions contains both 'variable' and 'essential' reactions. 'Variable' reactions are reactions that can carry a range of fluxes. These variable reactions may be considered 'substitutable' if they can carry a zero flux within the range and 'non-substitutable' if they can only carry non-zero flux. Non-substitutable reactions are also a part of the 'essential' group of reactions. Essential reactions are reactions that must carry a flux in order for the network to reach optimality during a modelling and this group of reactions can contain reactions which are variable (non-substitutable) or not (fixed flux value). For MG-BR, FVA identified 394 reactions that were allowed to carry flux in order to reach optimality. 21% of these reactions were found to be variable. Meanwhile, for BR-TU stages of ripening, FVA identified 351 reactions that were allowed to carry flux and only 13% of these reactions were found to be variable. Tables 4.5 and 4.6 lists all variable reactions identified for MG-BR and BR-TU stages respectively.

4.2.3 Additional influx of sugars and amino acids were required to obtain an optimal flux distribution

The MG-BR and BR-TU transitions were modelled in a closed system and no optimal flux distribution could be found. In order to find an optimal flux distribution that satisfied the objective function to minimise the sum of fluxes

within the applied constraints, the metabolic network was required to be modelled as an open system. This allowed influx of sugars and amino acids from the phloem as additional inputs to the metabolic network. As can be seen from tables 4.1 and 4.3, MG-BR required substantially higher influx of sugars and amino acids from the phloem than BR-TU (18.82 μmol/gFW/day of additional sugar influx and 2.32 μmol/gFW/day of amino acid influx during MG-BR). Only 26% of the sugar influx from the phloem during MG-BR was stored as sucrose, glucose and fructose, which were constrained as outputs, and the remaining sugar was degraded through glycolysis (Tables 4.1 and 4.2). On the other hand, BR-TU required 4.93 μmol/gFW/day of additional sugar influx and only 0.07 μmol/gFW/day of additional amino acid influx. 100% of the additional sugar influx during BR-TU was used for storage of glucose and fructose that were constrained as outputs (Table 4.4). Sugar was also supplied through sucrose that was constrained as an input during BR-TU (Table 4.3).

4.2.4 Dominant fluxes during MG-BR are those involved in glycolysis

To assess the optimal flux distribution predicted for each transition, reactions were sorted according to their flux values. The reactions with fluxes above 5.00 μmol/gFW/day were mapped out. These reactions represented 21% of the total number of reactions that carried flux during MG-BR. Figure 4.3A presents a distribution of the dominant fluxes predicted for MG-BR. These reactions are involved in glycolysis, which occurred in two subcellular locations. The first part of the pathway that converted sugars into dihydroxyacetone phosphate (DHAP) and glyceraldehyde-3-phosphate (GAP) occurred in the cytosol. GAP was then imported into plastid where it was converted into 3-

phosphoglycerate (3-PGA). The last process of 3-PGA conversion into phospho*enol*pyruvate (PEP) took place in the cytosol again. It was also shown that significant oxaloacetate (OAA) flux was predicted to enter the peroxisome where it was converted into citrate and malate. Citrate and malate were constrained as outputs during MG-BR.

4.2.5 Low glycolytic flux predicted during BR-TU

To assess the change in flux distribution between BR-TU and MG-BR, cytosolic reactions that carried flux during BR-TU were mapped out. Figure 4.3 compares the cytosolic and plastidic flux distribution predicted during MG-BR and BR-TU. It is apparent from this diagram that flux through the glycolytic pathway is almost non-existent during BR-TU (Figure 4.3B). Only the reactions in the upper part of glycolysis were active and carried small flux values. These reactions were involved with the accumulation of sugars such as trehalose and maltose, which are constrained as outputs during BR-TU. From Figure 4.3B, we can see that the significant cytosolic and plastidic fluxes during BR-TU were those involving malate, OAA and pyruvate, which ultimately forms cytosolic acetyl-coA.

4.2.6 A complete TCA cycle flux mode was predicted during MG-BR

The distribution of dominant fluxes during MG-BR continued in the mitochondria. Figure 4.4 presents the predicted TCA cycle flux modes during MG-BR and BR-TU. It can be seen that a complete TCA cycle flux mode was predicted during MG-BR and a partial TCA cycle flux mode for BR-TU. The individual reactions in the TCA cycle did not carry the same flux during MG-BR.

Figure 4.4A shows that mitochondrial ATP synthesis was a significant flux and 25.86 μmol/gFW/day of mitochondrial carbon dioxide (CO_2) was exported into the cytosol. It was also shown that the main substrate for the TCA cycle was predicted to be malate and the main metabolite to be exported into the cytosol was citrate. Propionyl-coA, a downstream product of chlorophyll degradation during MG-BR was also shown to join the TCA cycle via succinyl-coA in Figure 4.4A. This is an important observation as the chlorophyll degradation pathway was manually added into this model, thus the joining of succinyl-coA into TCA cycle proves that the chlorophyll degradation pathway is well integrated into this tomato metabolic model.

4.2.7 A partial TCA cycle flux mode was predicted during BR-TU

Turning now to the mitochondrial flux distribution during BR-TU, it can be seen that a partial TCA cycle flux mode was predicted (Figure 4.4B). The active reactions were of those involved in the lower half of the TCA cycle and these reactions did not carry identical fluxes. The main substrate for this partial TCA cycle was 2-oxoglutarate (2-OG) with an influx of 7.45 μmol/gFW/day and the main metabolite exported to the cytosol was malate with an efflux of 10.10 μmol/gFW/day. GABA was shown to be degraded into glutamate via GABA transaminase and glutamate in turn was converted into aspartate through the action of an aspartate transaminase reaction (Figure 4.4B). The mitochondrial ATP produced is significant but was only 43% of the mitochondrial ATP produced during MG-BR. Mitochondrial reactions during this transition were shown to export 7.56 μmol/gFW/day of CO_2 into the cytosol, which is a 3.4-fold decrease from MG-BR.

4.2.8 Carotenoid biosynthesis during MG-BR was predicted to require both the mevalonate (MEV) and methylerythritol phosphate (MEP) pathways

Carotenoids make up 6.3% of the total metabolite that was required to accumulate during MG-BR and β-carotene was the fourth most accumulated metabolite (Table 4.2). From the flux distribution in Figure 4.3A, it is apparent that both the cytosolic MEV and plastidic MEP pathways were operating during MG-BR to provide the precursors for carotenoid biosynthesis. In order to discern how the carotenoids are synthesised during MG-BR, fluxes through these two pathways and carotenoid biosynthesis are presented in more detail in Figure 4.5A. The plastidic MEP pathway was the predominant route to synthesise carotenoids during MG-BR contributing 78% of the total isopentenyl diphosphate (IPP) required for this process (Figure 4.5A).

4.2.9 The MEV and not the MEP pathway for carotenoid biosynthesis operated during BR-TU

During BR-TU, β-carotene was the third highest metabolite required to degrade (Table 4.3). It is apparent that the plastidic reactions did not carry much flux as shown in Figure 4.2A and, in contrast to MG-BR, the cytosolic MEV pathway and not the MEP pathway was responsible for the provision of precursors for carotenoid biosynthesis during BR-TU. Figure 4.5 compares the flux distribution for carotenoid biosynthesis during MG-BR and BR-TU. The MEV pathway during BR-TU was shown to be the sole supplier of IPP and IPP was imported into the plastid to produce dimethylallyl diphosphate (DMAPP), another precursor for carotenoid biosynthesis.

4.2.10 Higher CO_2 release during BR-TU than MG-BR

A significantly higher efflux CO_2 was predicted for the BR-TU transition than for MG-BR: (54.80 mmol/gFW/day compared to 20.78 mmol/gFW/day, respectively) (Figure 4.6). Mitochondrial reactions were shown to be the top CO_2 contributor during MG-BR, followed by plastidial, cytosolic, and peroxisomal reactions. The cytosolic phospho*enol*pyruvate carboxylase (PEPC) was the dominant CO_2 fixing reaction during this transition (Figure 4.6A). Meanwhile, the cytosolic reactions were predicted to be main CO_2 contributor during BR-TU stages, followed by the mitochondrial, peroxisomal and plastidial reactions. A much lower flux was predicted for fixing CO_2 during this transition (Figure 4.6B).

4.2.11 Fewer metabolites can be accumulated when the MG-BR transition is modelled as a closed system

No feasible flux distribution could be found when MG-BR and BR-TU were modelled as closed systems (i.e. additional influx of sugars and amino acids from the phloem was not permitted) and constrained to a fixed flux rate of inputs and outputs (as described in 4.2.1). To assess which metabolites were able to accumulate with the existing inputs (i.e. not including the 'open' transporters), both MG-BR and BR-TU were modelled with more flexibility in the outputs. The metabolites during these transitions were allowed to accumulate within a broad flux range -- minimum flux of 0.0001 μmol/gFW/day and no maximum flux limit. This forced the metabolite output transporters to carry flux during modelling but they could carry any flux value. The inputs remain constrained with a fixed flux rate and no additional influx of sugars and amino

acids were allowed to enter the system. As a result, only 21 out of 38 metabolites were able to accumulate during MG-BR whereas all 26 metabolites were able to accumulate during BR-TU (tables 4.8 and 4.9). Most of these metabolites were only able to accumulate with minimum flux of 0.001 μmol/gFW/day except for succinate, β-carotene, aspartate and caffeate, which had fluxes greater than the minimum during MG-BR. The three most abundant sugars during MG-BR: glucose, sucrose and fructose- were not able to accumulate when modelled in a closed system. Amongst the metabolites that could, succinate was shown to accumulate highest with 5.398 μmol/gFW/day followed by aspartate with 0.508 μmol/gFW/day. It was similar for BR-TU where most metabolites were only able to accumulate with a minimum flux of 0.001 μmol/gFW/day except for glucose, neoxanthin, fructose, succinate, caffeatte, myoinositol-1-phosphate, lycopene and sorbitol, which had fluxes more than 0.0001 μmol/gFW/day. Succinate was also predicted to accumulate highest during BR-TU with 15.00 μmol/gFW/day. This was followed by glutamate with 4.237 μmol/gFW/day and neoxanthin with 1.904 μmol/gFW/day. In contrast to MG-BR, glucose and fructose were able to accumulate during this transition but with significantly lower flux relative to when BR-TU was modelled in an open system. The accumulation fluxes predicted for these metabolites during both transitions were significantly different from the experimental data (tables 4.8 and 4.9). I also explored whether further relaxing the metabolic output by applying different weighting factors to each output constraint allowed a more detailed exploration of the metabolic capability of the closed system. In FBA, all reactions are assigned a weighting factor and the default is to have all reactions equally weighted (i.e. a weighting factor of 1). Slightly increased fluxes were

observed for some of the output metabolites when the weighting factors were adjusted. Rather than an equal weighting of 1, each output reaction was weighted according to the reciprocal value of output flux multiplied by the molecular mass of the metabolite. This ensures that the small molecules were not preferentially produced. These modified weighting factors reordered the importance of the accumulation of the output metabolites. However, a major problem with this approach was that multiple optimal flux distributions were found. In order to assess the variability of the reactions, FVA was carried out. A total of 886 reactions were allowed to carry flux during MG-BR and all of these reactions were variable within an infinite range. This approach, therefore, does not produce a useful answer from a modelling perspective. Clearly some combinations of output flux values are possible in a closed system, but I was not able to develop a modelling approach to explore this solution space effectively.

Table 4.1. List of inputs used for modelling MG-BR. Input flux corresponds to the flux value used to constrain the model and the values were based on experimental data as outlined in section 4.2.1 (Baxter et al., 2005; Carrari et al., 2006; Ré et al., 2012). Carbon flux corresponds to the input flux multiplied with the number of carbons in the corresponding metabolite. Phloem amino acid levels (**) were obtained from Valle et al (1998) and all of these amino acids were written as one equation/ reaction in the model. (*) denotes the total influx of amino acids from the phloem predicted from modelling this transition.

	inputs	input flux	number of carbons	carbon flux
1	chlorophyll a	0.973	55	53.51
2	chlorophyll b	0.348	55	19.14
3	alanine	0.127	3	0.38
4	valine	0.092	5	0.46
5	leucine	0.074	6	0.44
6	lysine	0.052	6	0.31
7	methionine	0.051	5	0.26
8	threonine	0.043	4	0.17
9	arginine	0.038	6	0.23
10	tyrosine	0.026	9	0.23
11	histidine	0.014	6	0.08
12	asparagine	0.009	4	0.04
13	glycine	0.006	2	0.01
14	violaxanthin	0.005	40	0.20
15	sucrose_phloem	18.815	12	225.78
16	amino acids_phloem:	2.324*		
	glutamate	0.535**	5	2.67
	phenylalanine	0.232**	9	2.09
	aspartate	0.256**	4	1.02
	glutamine	1.023**	5	5.11
	threonine	0.302**	4	1.21

	other transporters	input flux	number of carbons	carbon flux
1	oxygen	32.300	0	0
2	sulphate	0	0	0
3	phosphate	0	0	0
	Total carbon flux			**313.3**

Table 4.2. List of outputs used for modelling MG-BR. Output flux corresponds to the flux value used to constrain the model and the values were based on experimental data as outlined in section 4.2.1 (Baxter et al., 2005; Carrari et al., 2006; Ré et al., 2012). Carbon flux corresponds to the output flux multiplied by the number of carbons of the corresponding metabolite. NCCs- non-fluorescent chlorophyll catabolites, which are one of the end products of chlorophyll degradation, are modelled as a sink transporter in this transition to achieve carbon flux balance in the network.

	output	output flux	number of carbons	carbon flux
1	citrate	18.551	6	111.304
2	glucose	2.449	6	14.691
3	sucrose	1.560	12	18.714
4	beta carotene	1.341	40	53.652
5	GABA	1.086	4	4.343
6	fructose	0.985	6	5.909
7	malate	0.770	4	3.080
8	glutamine	0.745	5	3.725
9	aspartate	0.365	4	1.462
10	glutamate	0.339	5	1.696
11	antheraxanthin	0.336	40	13.440
12	phenylalanine	0.272	9	2.450
13	zeaxanthin	0.193	40	7.728
14	putrescine	0.187	4	0.747
15	myoinositol	0.127	6	0.762
16	isocitrate	0.070	6	0.419
17	succinate	0.056	4	0.226
18	cysteine	0.051	3	0.153
19	maltose	0.050	12	0.605
20	serine	0.048	3	0.143
21	shikimate	0.037	7	0.260
22	ornithine	0.035	5	0.174
23	dehydroascorbate	0.033	6	0.199
24	glucose-6-phosphate	0.009	6	0.052
25	sorbitol	0.007	6	0.040
26	proline	0.006	5	0.031
27	ribose	0.006	5	0.030
28	glycerate	0.006	3	0.018
29	caffeatte	0.005	9	0.046
30	isoleucine	0.005	6	0.031
31	ascorbate	0.005	6	0.030
32	fructose-6-phosphate	0.005	6	0.030
33	fumarate	0.004	4	0.018
34	trehalose	0.004	12	0.049
35	myoinositol-1-phosphate	0.003	6	0.018
36	glycerol-3-phosphate	0.003	3	0.009
37	aconitate	0.002	6	0.012
38	2-oxoglutarate	0.001	5	0.005
	other transporters	**output flux**	**number of carbons**	**carbon flux**
1	carbon dioxide	20.779	1	20.780
2	NCCs	1.321	35	46.235
	Total carbon flux			**313.3**

Table 4.3. List of inputs used for modelling BR-TU. Input flux corresponds to the flux value used to constrain the model and the values are based on experimental data as outlined in section 4.2.1 (Baxter et al., 2005; Carrari et al., 2006; Ré et al., 2012). Carbon flux corresponds to the input flux multiplied with the number of carbons of the corresponding metabolite. Amounts of phloem amino acid phloem (**) were obtained from Valle *et al* (1998) and all of these amino acids were written as one equation/ reaction in the model. (*) denotes the total influx of amino acids from the phloem predicted from modelling this transition.

	inputs	input flux	number of carbons	carbon flux
1	citrate	15.024	6	90.143
2	GABA	2.684	4	10.738
3	beta carotene	1.317	40	52.696
4	malate	0.964	4	3.855
5	glutamine	0.521	5	2.603
6	antheraxanthin	0.352	40	14.092
7	sucrose	0.297	12	3.565
8	zeaxanthin	0.217	40	8.672
9	serine	0.153	3	0.460
10	myoinositol	0.127	6	0.762
11	glycine	0.115	2	0.231
12	valine	0.076	5	0.381
13	phenylalanine	0.071	9	0.640
14	isocitrate	0.064	6	0.386
15	shikimate	0.057	7	0.399
16	asparagine	0.034	4	0.135
17	mannitol	0.023	6	0.136
18	leucine	0.018	6	0.111
19	violaxanthin	0.018	40	0.708
20	glucose-6-phosphate	0.017	6	0.099
21	fructose-6-phosphate	0.006	6	0.035
22	glycerol-3-phosphate	0.005	3	0.014
23	fumarate	0.005	4	0.019
24	glycerate	0.004	3	0.011
25	histidine	0.003	6	0.021
26	arginine	0.003	6	0.019
27	tyrosine	0.003	9	0.026
28	aconitate	0.002	6	0.011
29	2-oxoglutarate	0.001	5	0.005
30	sucrose_phloem	2.812	12	33.741
31	glucose_phloem	2.125	6	12.750
32	amino acids_phloem:	0.07*		
	glutamate	0.015**	5	0.076
	phenylalanine	0.007**	9	0.060
	aspartate	0.007**	4	0.029
	glutamine	0.029**	5	0.146
	threonine	0.009**	4	0.035

	other transporters	input flux	number of carbons	carbon flux
1	oxygen	25.11	0	0
2	sulphate	0.11	0	0
	Total carbon flux			**237.81**

Table 4.4. List of outputs used for modelling BR-TU. Output flux corresponds to the flux value used to constrain the model and the values were based on experimental data as outlined in section 4.2.1 (Baxter et al., 2005; Carrari et al., 2006; Ré et al., 2012). Carbon flux corresponds to the output flux multiplied with its corresponding number of carbons. NCCs: non-fluorescent chlorophyll catabolites, which are a product of chlorophyll degradation and are modelled as a sink transporter during MG-BR to achieve carbon flux balance in the network.

	outputs	output flux	number of carbons	carbon flux
1	glucose	5.2307	6	31.384
2	fructose	2.8772	6	17.263
3	neoxanthin	2.7192	40	108.770
4	aspartae	1.9891	4	7.957
5	glutamate	1.4107	5	7.054
6	putrescine	0.2021	4	0.808
7	alanine	0.1755	3	0.527
8	myoinositol-1-phosphate	0.1270	6	0.762
9	caffeatte	0.0936	9	0.843
10	maltose	0.0899	12	1.079
11	methionine	0.0803	5	0.401
12	lycopene	0.0746	40	2.983
13	isoleucine	0.0670	6	0.402
14	ribose	0.0655	5	0.328
15	tyramine	0.0440	8	0.352
16	threonine	0.0353	4	0.141
17	lutein	0.0302	40	1.207
18	ornithine	0.0268	5	0.134
19	lysine	0.0268	6	0.161
20	dehydroascorbate	0.0262	6	0.157
21	cysteine	0.0261	3	0.078
22	succinate	0.0256	4	0.102
23	proline	0.0105	5	0.053
24	ascorbate	0.0048	6	0.029
25	trehalose	0.0032	12	0.038
26	sorbitol	0.0003	6	0.002

	other transporters	flux value	number of carbons	carbon flux
1	carbon dioxide	54.80	1	54.797
2	NCCs	0.00	0	0.000
	Total carbon flux			**237.81**

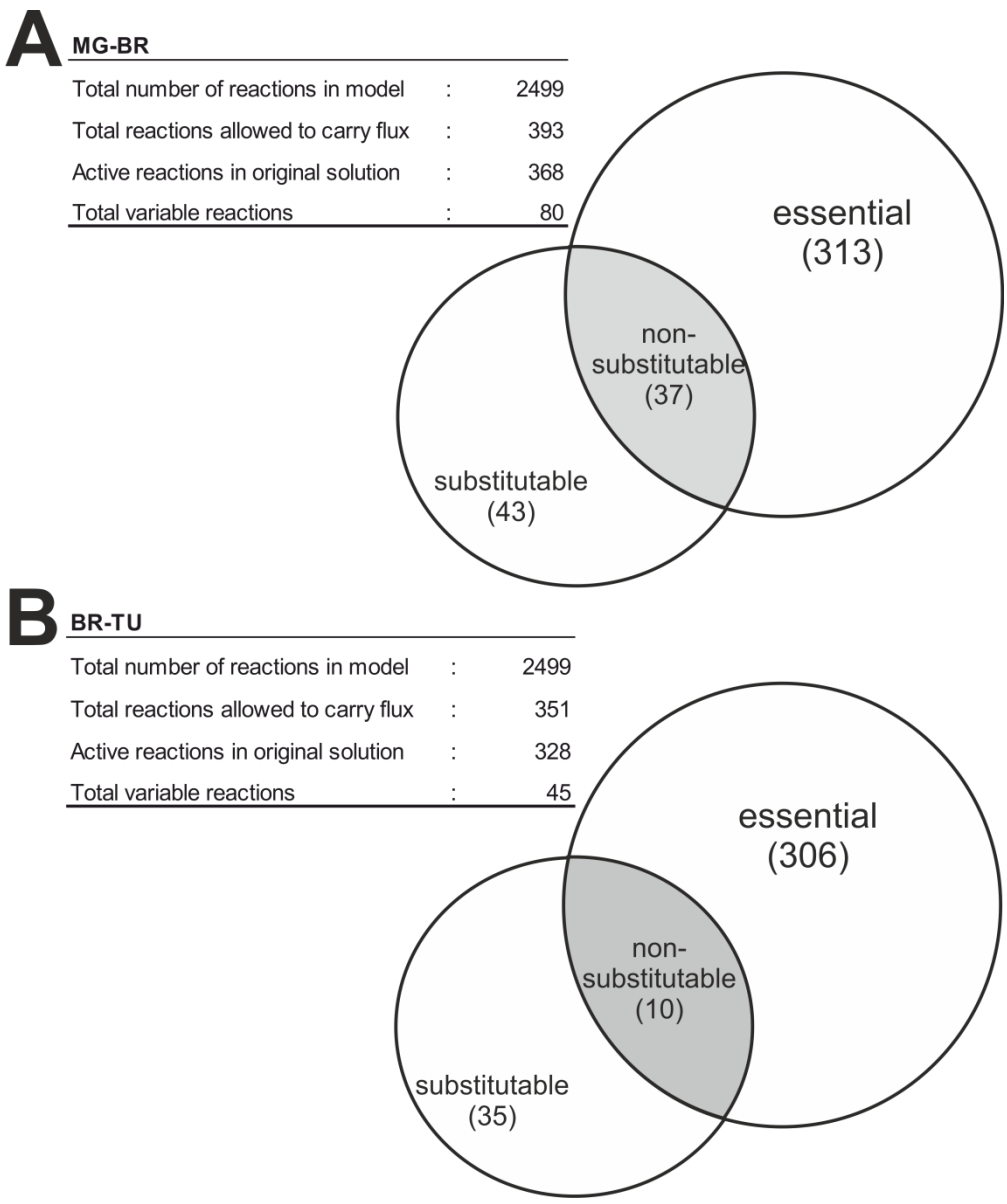

Figure 4.2. A summary of the results from Flux Variability Analysis (FVA). FVA was carried out on both transitions; (A) MG-BR, and (B) BR-TU. 'Original solution' means the first optimal flux distribution obtained when modelling the ripening stages. Through FVA, reactions that were allowed to carry flux were identified. These reactions include essential and substitutable reactions; hence there are fewer reactions in the original solution relative to the number of reactions allowed to carry flux. Essential reactions represent the reactions that must carry non-zero flux in order to reach optimality. They may be variable. Essential reactions which are variable are deemed non-substitutable. Meanwhile, the remaining variable reactions are deemed substitutable and these reactions may carry zero flux. Allowable reactions identified through FVA in these ripening stages are represented as a Venn diagram. Lists of variable reactions are listed in Table 4.3 for MG-BR and Table 4.4 for BR-TU.

Table 4.5. List of variable reactions identified through FVA for MG-BR. ‘Essential’ and ‘substitutable’ reactions means that in order for an optimal flux distribution to be obtained, these reactions must carry flux or may be substituted with other reaction(s) respectively.

	cytosolic variable reactions	original solution	min	max	variability type
1	phosphoglycerate mutase	42.13	42.13	43.80	essential
2	phosphopyruvate hydratase	42.13	42.13	43.80	essential
3	phosphoenolpyruvate carboxylase	42.13	42.13	43.80	essential
4	fructokinase	30.65	16.27	30.65	essential
5	triosephosphate isomerase	30.61	0.00	30.61	substitutable
6	xylose isomerase	14.38	0.00	14.38	substitutable
7	malate dehydrogenase	13.04	11.38	16.37	essential
8	phosphoglycerate kinase	12.38	10.71	12.38	essential
9	glyceraldehyde-3-phosphate dehydrogenase	12.38	10.71	12.38	essential
10	glutamate dehydrogenase (NADP)	6.99	0.00	6.99	substitutable
11	aspartate aminotransferase	6.98	4.97	7.11	essential
12	L-serine ammonia-lyase	6.37	0.00	6.37	substitutable
13	malate dehydrogenase (NADP)	5.55	5.49	8.88	essential
14	glucokinase	0.29	0.29	14.67	essential
15	citrullinase	0.18	0.18	0.22	essential
16	ornithine decarboxylase	0.15	0.15	0.19	essential
17	hexokinase	0.13	0.13	14.52	essential
18	aminoadipate-semialdehyde dehydrogenase	0.05	0.00	0.05	substitutable
19	arginine decarboxylase	0.04	0.00	0.04	substitutable
20	agmatinase	0.04	0.00	0.04	substitutable
21	urease	0.04	0.00	0.04	substitutable
22	phosphogluconate dehydrogenase	0.01	0.00	0.01	substitutable
23	aldehyde dehydrogenase	0.00	0.00	0.05	substitutable
24	phosphogluconate dehydrogenase (NADP)	0.00	0.00	0.01	substitutable
25	glucose-6-phosphate isomerase	0.00	0.00	14.38	substitutable
26	N-carbamoylputrescine amidase	0.00	0.00	0.04	substitutable
27	glucose-6-phosphate isomerase (isoenzyme)	0.00	0.00	14.38	substitutable
28	aconitate hydratase	0.00	0.00	0.07	substitutable
29	aconitase	0.00	0.00	0.07	substitutable
30	arginine deiminase	0.00	0.00	0.04	substitutable
31	agmatine deiminase	0.00	0.00	0.04	substitutable
32	NAD(P)(+) transhydrogenase	0.00	0.00	4.99	substitutable
33	glutamate dehydrogenase (NADP+)	0.00	0.00	6.99	substitutable

	peroxisomal variable reactions	original solution	FVA		variability type
			min	max	
1	OAA transporter	22.11	22.11	22.46	essential
2	citrate transporter	10.22	10.15	10.22	essential
3	2-oxoglutarate transporter	1.67	1.32	1.67	essential
4	glutamate transporter	0.35	0.00	0.35	substitutable
5	isocitrate transporter	0	0.00	0.07	substitutable
6	aspartate transporter	0	0.00	0.35	substitutable
7	aconitate hydratase	0	0.00	0.07	substitutable
8	aconitase	0	0.00	0.07	substitutable
9	aspartate aminotransferase	0	0.00	0.35	substitutable

	plastidic variable reactions	original solution	min	max	variability type
1	glyceraldehyde 3-phosphate dehydrogenase	36.531	36.531	38.195	essential
2	phosphoglycerate kinase	36.531	36.531	38.195	essential
3	GAP - 3PGA exchanger	29.754	0.000	33.082	substitutable
4	malate dehydrogenase	29.329	29.329	30.993	essential
5	malate dehydrogenase (NADP)	22.445	22.323	24.110	essential
6	carbon dioxide exporter	19.387	17.723	19.509	essential
7	GAP phosphate transporter	19.085	0.000	19.085	substitutable
8	aspartate aminotransferase	6.883	5.219	7.006	essential
9	aspartate transporter	6.883	7.006	5.219	essential
10	malic enzyme (NADP)	6.700	5.036	6.822	essential
11	phosphoglycerate dehydrogenase	6.650	4.986	6.650	essential
12	phosphoserine transaminase	6.650	4.986	6.650	essential
13	phosphoserine phosphatase	6.650	4.986	6.650	essential
14	phopshate proton transporter	6.568	4.903	6.568	essential
15	serine transporter	6.472	0.100	6.472	essential
16	pyruvate transporter	5.696	0.000	7.360	substitutable
17	cystathionine β–synthase	0.178	0.178	6.213	essential
18	cystathionine β–lyase	0.173	0.173	6.207	essential
19	ATP transporter	1.664	0.000	1.664	substitutable
20	GLT-MAL exchanger	0.183	0.000	0.183	substitutable
21	triosephosphate isomerase	0.082	0.082	30.689	essential
22	2OG-MAL exchanger	0.000	0.000	0.183	substitutable
23	DHAP-3PGA exchanger	0.000	0.000	30.607	substitutable
24	DHAP phosphate transporter	0.000	0.000	19.085	substitutable
25	ammonia transporter	0.000	0.000	6.034	substitutable
26	OAA-MAL exchanger	0.000	0.000	1.664	substitutable

	mitochondrial variable reactions	original solution	FVA		variability type
			min	max	
1	malate phosphate transporter	8.718	8.648	9.913	essential
2	mAL-CIT exchanger	8.334	7.069	8.406	essential
3	aconitate hydratase	2.946	2.874	2.946	essential
4	aconitase	2.944	2.874	2.944	essential
5	2OG-MAL exchanegr	2.110	0.845	2.110	essential
6	succinate phosphate transporter	1.195	0.000	1.265	substitutable
7	SUCC-ISOCIT exchanger	0.070	0.000	0.070	substitutable
8	mAL-aconitate exchanger	0.002	0.000	0.072	substitutable
9	2OG-SUCC exchanger	0.000	0.000	1.265	substitutable
10	SUCC-CIT exchanger	0.000	0.000	1.265	substitutable
11	SUCC-ACONITATE exchanger	0.000	0.000	0.072	substitutable
12	MAL-isocitrate exchanger	0.000	0.000	0.070	substitutable

Table 4.6. List of variable reactions identified through FVA for BR-TU. 'Essential' reactions means that these reactions must carry flux in order for an optimal flux distribution to be obtained and 'substitutable' means that these reactions may be substituted with other reaction(s) for an optimal flux distribution to be obtained

	cytosolic variable reactions	original solution	FVA		variability type
			min	max	
1	citrullinase	0.229	0.226	0.229	essential
2	cystathionine gamma lyase	0.147	0.106	0.147	essential
3	ornithine decarboxylase	0.202	0.199	0.202	essential
4	inosine nucleosidase	0.066	0.000	0.066	substitutable
5	cystathioninase	0.041	0.000	0.041	substitutable
6	nucleotidase	0.066	0.000	0.066	substitutable
7	Hypoxanthine phosphoribosyltransferase	0.066	0.000	0.066	substitutable
8	Arginine deiminase	0.003	0.000	0.003	substitutable
9	cystathionine beta lyase	0.000	0.000	0.041	substitutable
10	urease	0.000	0.000	0.003	substitutable
11	ribonucleoside hydrolase	0.000	0.000	0.066	substitutable
12	nucleotidase	0.000	0.000	0.066	substitutable
13	triosephosphate isomerase	0.000	-0.003	0.000	substitutable
14	cystathionine gamma synthase	0.000	0.000	0.041	substitutable
15	N-carbamoylputrescine amidase	0.000	0.000	0.003	substitutable
16	hypoxanthine phosphoribosyltransferase	0.000	0.000	0.066	substitutable
17	agmatine deiminase	0.000	0.000	0.003	substitutable
18	Adenine phosphoribosyltransferase	0.000	0.000	0.066	substitutable
19	adenosine nucleosidase	0.000	0.000	0.066	substitutable
20	5'-nucleotidase	0.000	0.000	0.066	substitutable
21	agmatinase	0.000	0.000	0.003	substitutable
22	arginine decarboxylase	0.000	0.000	0.003	substitutable

	plastidic variable reactions	original solution	FVA		variability type
			min	max	
1	malate dehydrogenase (NADP)	7.759	2.667	7.813	essential
2	DHAP phosphate transporter	0.005	0.005	0.002	essential
3	glutamate-prephenate aminotransferase	0.016	0.016	0.057	essential
4	malate dehydrogenase	4.026	3.972	9.118	essential
5	zeaxanthin epoxidase (NADP, antheraxanthin producing)	2.349	0.000	2.349	substitutable
6	homoserine dehydrogenase (NAD)	0.027	0.000	0.027	substitutable
7	zeaxanthin epoxidase (NADP, violaxanthin producing)	2.702	0.000	2.702	substitutable
8	aromatic-amino-acid transaminase	0.041	0.000	0.041	substitutable
9	dihydrodipicolinate reductase (NAD)	0.027	0.000	0.027	substitutable
10	prephenate dehydrogenase	0.041	0.000	0.041	substitutable
11	triosephosphate isomerase	0.003	0.003	0.000	substitutable
12	homoserine dehydrogenase (NADP)	0.000	0.000	0.027	substitutable
13	dihydrodipicolinate reductase-(NADP)_p	0.000	0.000	0.027	substitutable
14	zeaxanthin epoxidase (NAD, violaxanthin producing)	0.000	0.000	2.702	substitutable
15	zeaxanthin epoxidase (NAD, antheraxanthin producing)	0.000	0.000	2.349	substitutable
16	GAP phosphate transporter	0.000	0.003	0.000	substitutable
17	arogenate dehydrogenase	0.000	0.000	0.041	substitutable

	mitochondrial variable reactions	original solution	FVA		variability type
			min	max	
1	2-OG - MAL exchanger	7.416	7.416	7.4416	essential
2	OAA-MAL exchanger	2.544	2.519	2.5444	essential
3	malate phosphate transporter	0.140	0.114	0.1400	essential
4	2OG - SUCCINATE exchanger	0.026	0.000	0.0256	substitutable
5	OAA-SUCCINATE exchanger	0.000	0.000	0.0256	substitutable
6	succinate phosphate exchanger	0.000	0.000	0.0256	substitutable

Table 4.7. Energy budget for MG-BR and BR-TU. Fluxes for production and consumption of ATP and reductant for all compartments predicted during both transitions are shown. Fluxes are in units of μmol/gFW/day.

MG-BR				BR-TU			
ATP CONSUMING		**ATP PRODUCING**		**ATP CONSUMING**		**ATP PRODUCING**	
CYTOSOL				**CYTOSOL**			
glycolysis	60.24	glycolysis	12.51	export to peroxisome	14.72	import from mitochondria	40.33
phloem unloading	21.14	import from mitochondria	92.75	MEV pathway	14.02		
metabolite storage	11.51			phloem unloading	5.32		
export into peroxisome	6.22			metbaolite storage	4.38		
MEV pathway	2.99			export to plastid	1.10		
exported into plastid	1.66			others	0.56		
chlorophyll degradation	1.32			glycolysis	0.23		
other cytosolic reactions	0.17						
total	**105.25**	**total**	**105.25**	**total**	**40.33**	**total**	**40.33**
MITOCHONDRIA				**MITOCHONDRIA**			
export to cytosol	92.75	oxidative phosphorylation	96.8369	export to cytosol	40.33	oxidative phosphorylation	40.50
adenyl kinase	2.73			others	0.17		
chlorophyll degradation	1.37						
total	**96.84**	**total**	**96.84**	**total**	**40.50**	**total**	**40.50**
PLASTID				**PLASTID**			
MEP pathway	37.42	glycolysis	36.53	ornithine accumulation	0.68	import from cytosol	1.10
others	0.60	import from cytosol	1.66	maltose accumulation	0.18		
glycolysis	0.18			others	0.11		
				threonine accumulation	0.08		
				tyrosine degradation	0.06		
total	**38.19**	**total**	**38.19**	**total**	**1.10**	**total**	**1.10**
PEROXISOME				**PEROXISOME**			
MEV pathway	4.90	import from cytosol	6.22	MEV pathway	14.72	import from cytosol	14.72
chlorophyll degradation	1.32						
total	**6.22**	**total**	**6.22**	**total**	**14.72**	**total**	**14.72**
NADH CONSUMING		**NADH PRODUCING**		**NADH CONSUMING**		**NADH PRODUCING**	
CYTOSOL				**CYTOSOL**			
malate dehydrogenase	13.04	glycolysis	12.38	malate dehydrogenase	16.15	transhydrogenase	15.97
glycerate accumulation	0.01	MEV pathway	0.32			MEV pathway	0.09
glycerol-3-phosphate accumulatior	0.003	myo-inositol accumulation	0.26			amino acid metabolism	0.04
		amino acid metabolism	0.05			ascorbate accumulation	0.03
		ascorbate accumulation	0.04			glycolysis	0.02
total	**13.05**	**total**	**13.05**	**total**	**16.15**	**total**	**16.15**
MITOCHONDRIA				**MITOCHONDRIA**			
electron transport chain	37.838	TCA cycle	37.48	electron transport chain	10.24	TCA cycle	7.44
		others	0.36			GABA degradation	2.68
total	**37.838**	**total**	37.84			amino acid metabolism	0.12
				total	**10.24**	**total**	**10.24**
PLASTID				**PLASTID**			
malate dehydrogenase	29.33	glycolysis	36.53	carotenogenesis	4.26	malate dehydrogenase	4.03
MEP pathway	12.47	others	6.74	amino acid metabolism	0.06	amino acid metabolism	0.16
carotenogenesis	1.05	OPP	0.16			pyruvate dehydrogenase	0.08
chlorophyll degradation	0.35	pyruvate dehydrogenase	0.09			OPP pathway	0.06
carotenogenesis	0.33			**total**	**4.32**	**total**	**4.32**
total	**43.53**	**total**	**43.53**				
PEROXISOME							
malate dehydrogenase	11.89	chlorophyll degradation	11.89				
total	**11.89**	**total**	**11.89**				
NADPH CONSUMING		**NADPH PRODUCING**		**NADPH CONSUMING**		**NADPH PRODUCING**	
CYTOSOL				**CYTOSOL**			
amino acid metabolism	6.992	MEV pathway	6.402	MEV pathway	18.22	malic enzyme	15.27
MEV pathway	4.903	malic enzyme	5.553	transhydrogenase	15.97	MEV pathway	11.72
others	0.052	OPP pathway	0.012	amino acid metabolism	1.02	isocitrate dehydrogenase	8.52
proline accumulation	0.012			succinate accumulation	0.29		
sorbitol accumulation	0.007			sorbitol accumulation	0.0003		
total	**11.967**	**total**	**11.967**	**total**	**35.50**	**total**	**35.51**
PLASTID				**PLASTID**			
carotenogenesis	16.55	malate dehydrogenase	22.45	carotenogenesis	7.35	malate dehydrogenase	7.76
MEP pathway	12.47	malic enzyme	6.70	others	0.33	malic enzyme	0.17
amino acid metabolism	0.27	OPP pathway	0.16	caffeatte accumulation	0.19	OPP pathway	0.06
caffeatte accumulation	0.01			amino acid metabolism	0.12		
others	0.01						
total	**29.30**	**total**	**29.30**	**total**	**7.99**	**total**	**7.99**

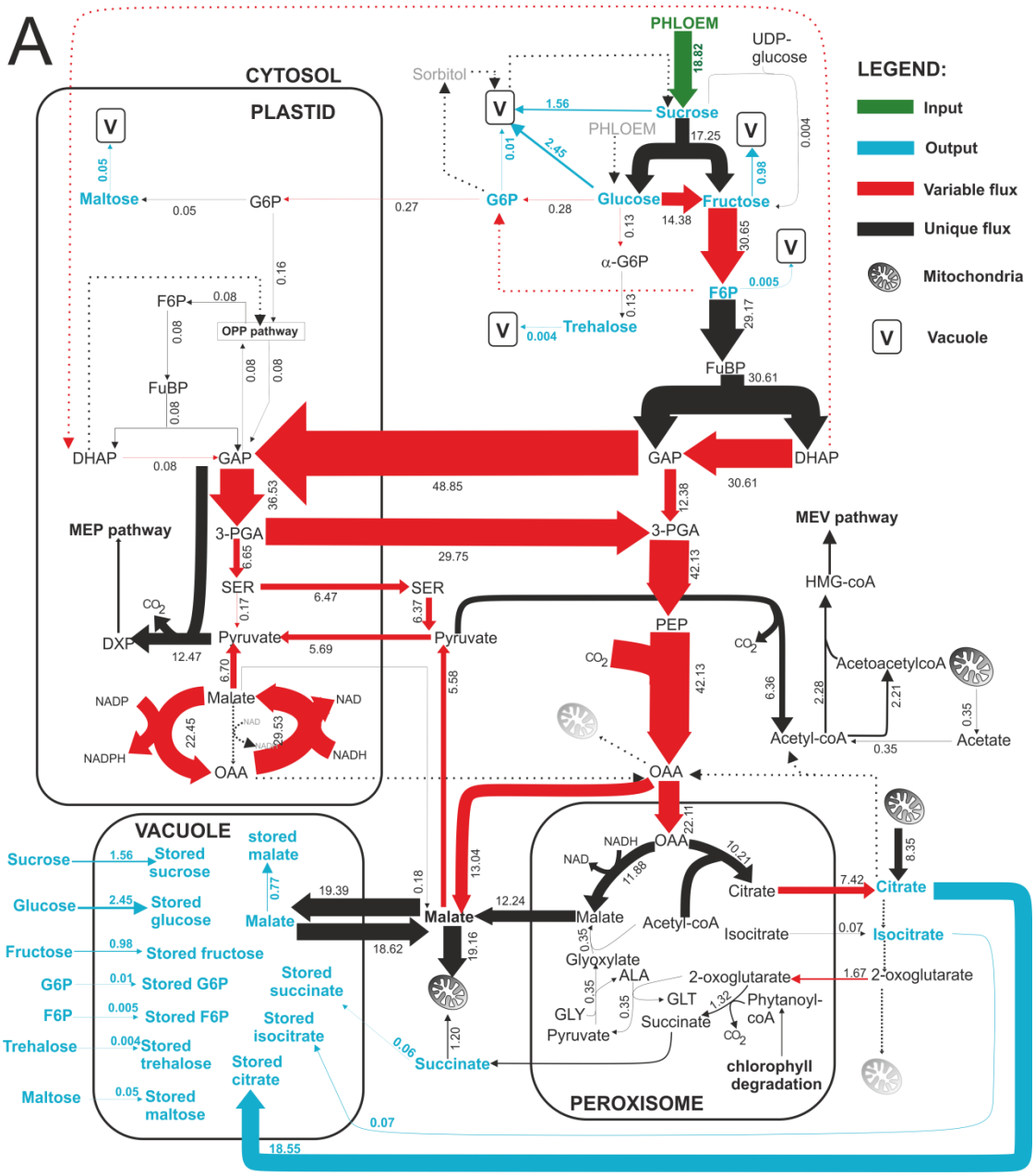

Figure 4.3. **Cytosolic and plastidic flux distribution during (A) MG-BR and (B) BR-TU stages of ripening.** Flux flow from the cytosol, plastid, peroxisome, and vacuole is shown. (A) Glycolysis was shown to operate in both cytosol and plastid, carrying dominant fluxes that supplied precursors for secondary metabolite biosynthesis and storage metabolites during MG-BR. (B) Citrate was shown to be the main carbon input during BR-TU. Fluxes for mitochondrial and secondary metabolite biosynthesis reactions are shown in figures 4.4 and 4.5 respectively. Flux variability analysis (FVA) was carried out for both of the ripening stages to identify variable fluxes and reactions with variable flux values are highlighted in red. These reactions are either essential, by which the reaction must carry flux to reach optimality, or substitutable, by which the reaction can carry zero flux and substituted with another reaction(s). Model inputs and

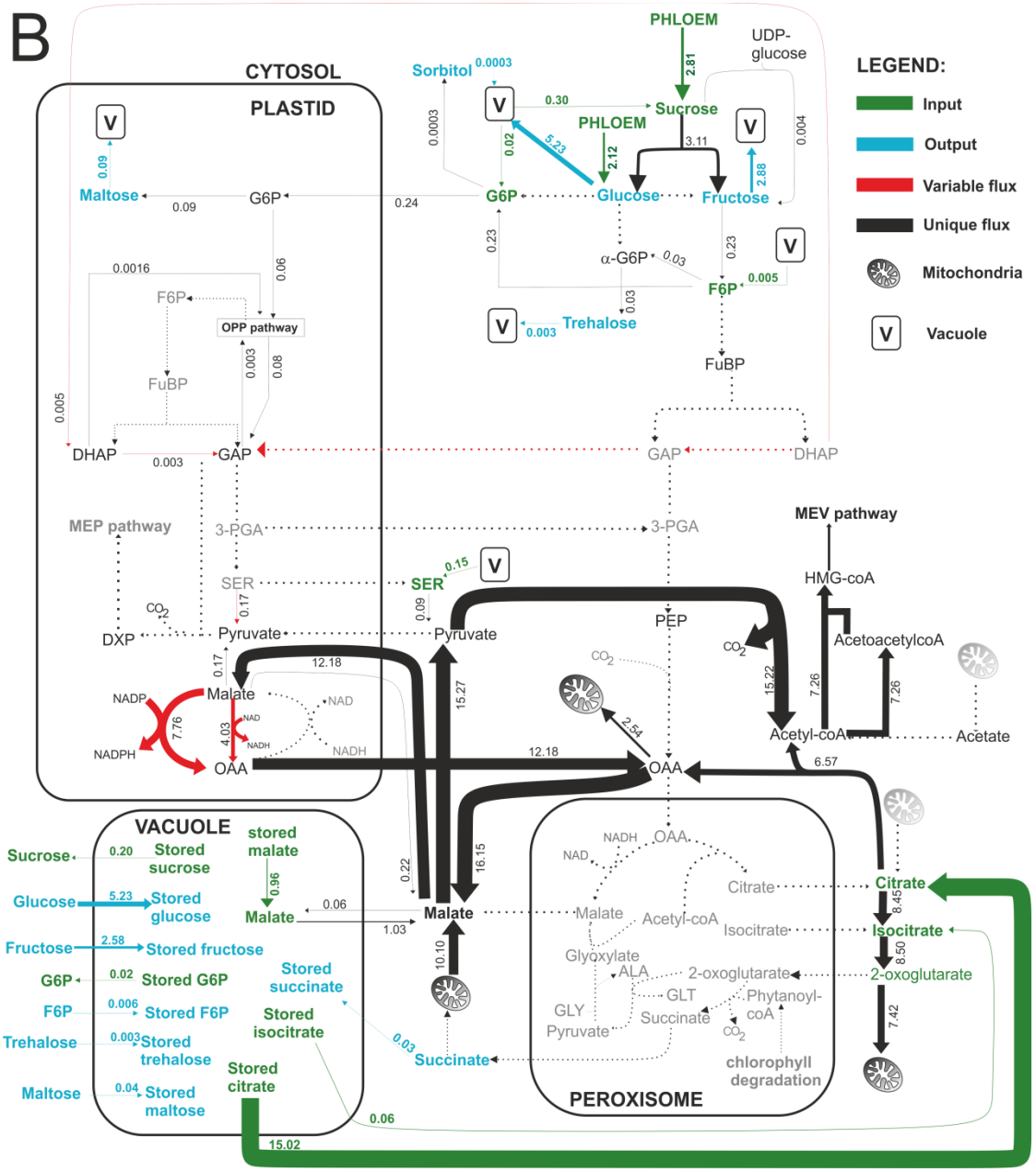

outputs for these simulations are colour coded as green and blue respectively. Dotted lines represent the reactions that were not active in that particular ripening stage. The numbers adjacent to the arrows represent the flux value obtained from the first optimal solution. A range of flux values allowable for these reactions are listed in Table 4.5 for MG-BR and Table 4.6 for BR-TU. This diagram does not represent the whole metabolic network and is not carbon balanced. The thickness of the arrows has been scaled to the flux magnitude. Multiple small vacuoles are shown for purposes of clarity and do not represent separate organelles. Fluxes are in units of μmol/gFW/day.

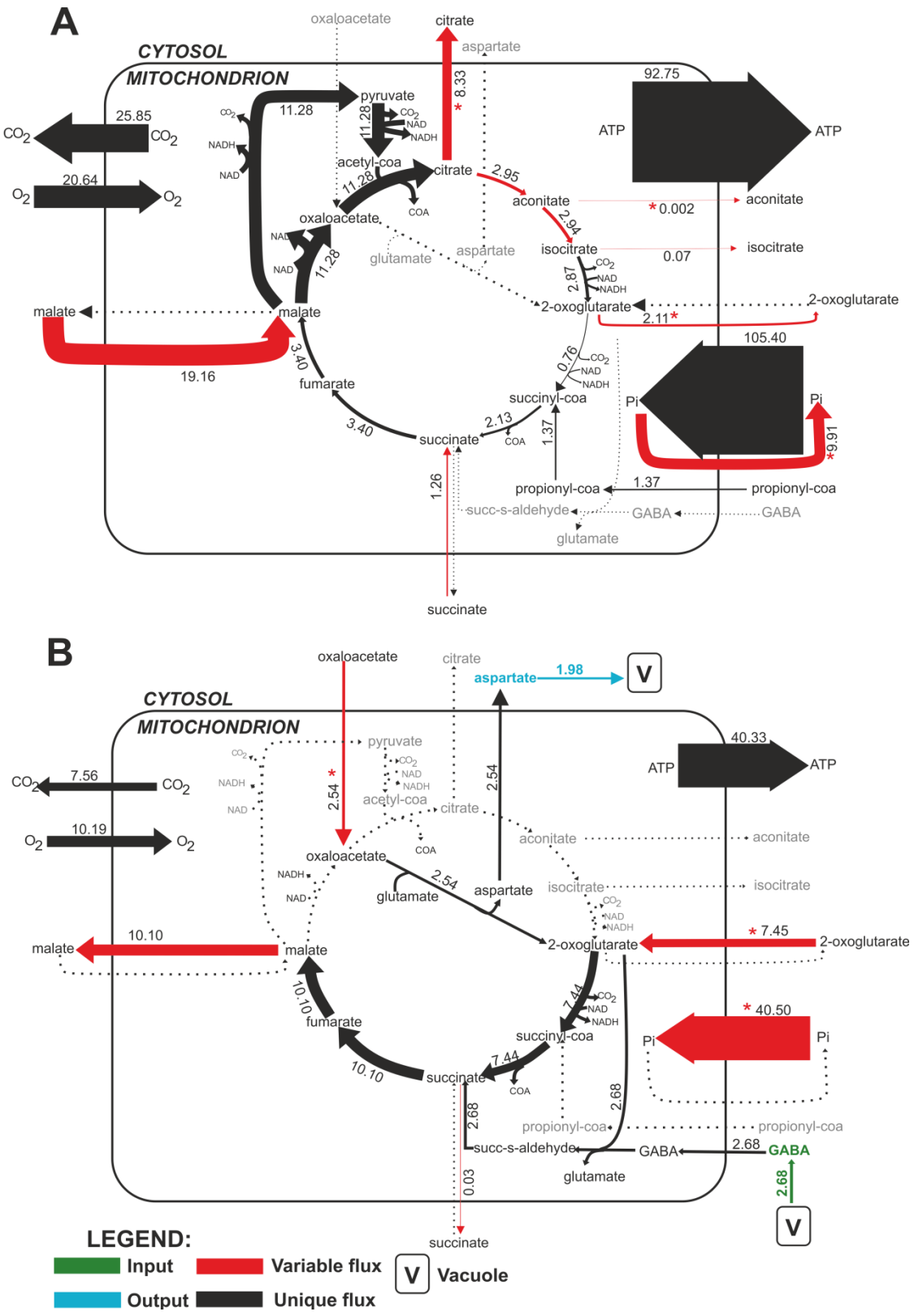

Figure 4.4. Mitochondrial flux modes during (A) MG-BR and (B) BR-TU stages of tomato fruit ripening. Influx and efflux of metabolites between the mitochondrion and cytosol is shown. A complete TCA cycle and significant ATP production was predicted for MG-BR whereas a partial cycle was predicted for BR-TU. Red asterisks denote the metabolites that are exchanged for the import or export of malate. Flux variability analysis (FVA) was carried out on both stages and variable fluxes are highlighted in red. Dotted lines represent the fluxes that were not active during that particular stage. Inputs and outputs are colour coded as green and blue respectively. This diagram does not represent all of the mitochondrial reactions and is not flux balanced. The thickness of the arrows has been scaled to the flux magnitude.

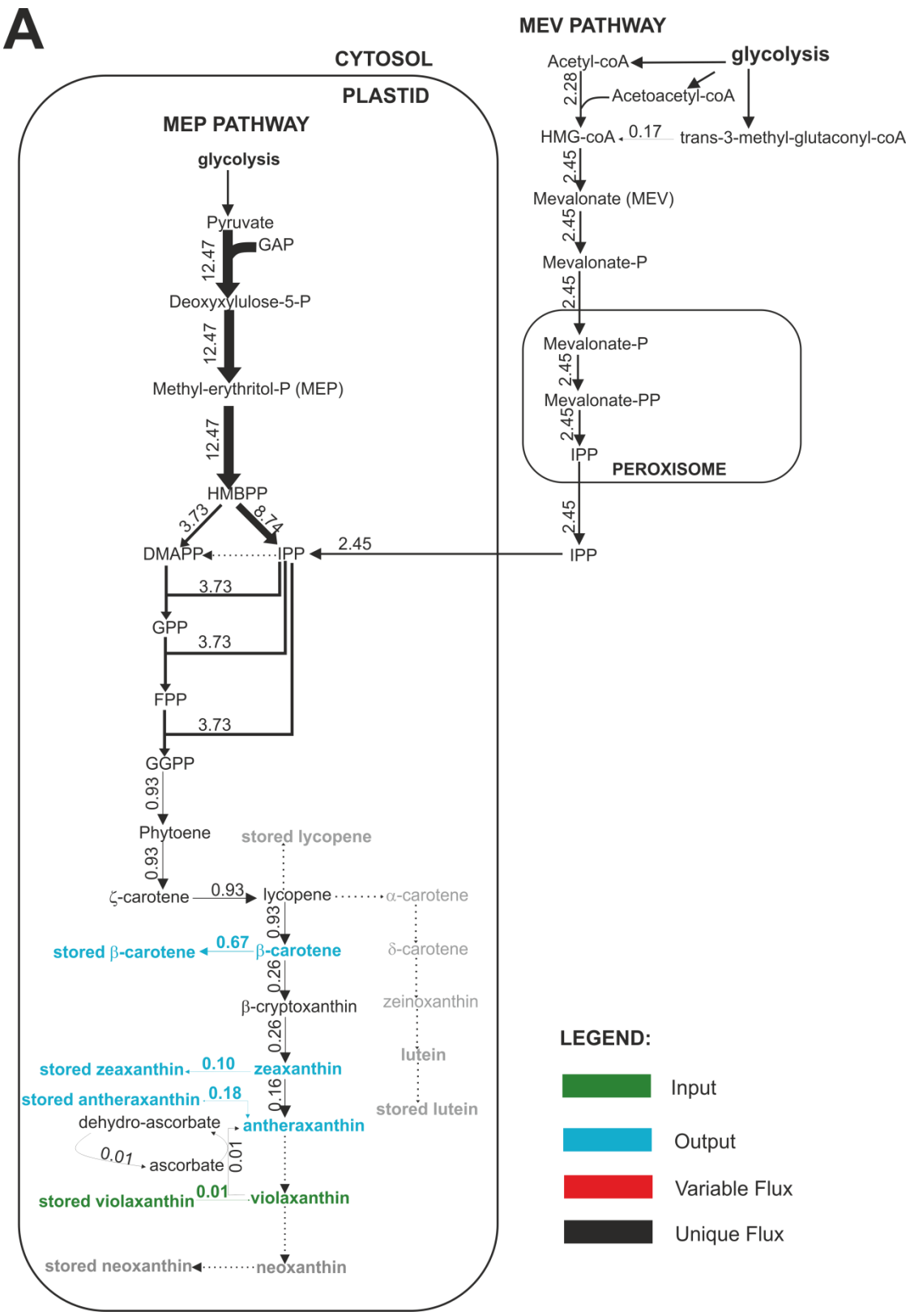

Figure 4.5. Flux modes for secondary metabolite biosynthesis during (A) MG-BR and (B) BR-TU of ripening. Both plastidic 2-methyl-D-erythritol-phsophate (MEP) and cytosolic mevalonate (MEV) pathways were operating during MG-BR and only the MEV pathway was operating during BR-TU. Dotted lines represent reactions that carried no flux in that particular stage. Precursors for these pathways were supplied by glycolysis, which was shown in Figure 4.2. Flux variability analysis was carried out on both stages and variable fluxes identified for these pathways are highlighted in red. Variable reactions are either essential, by

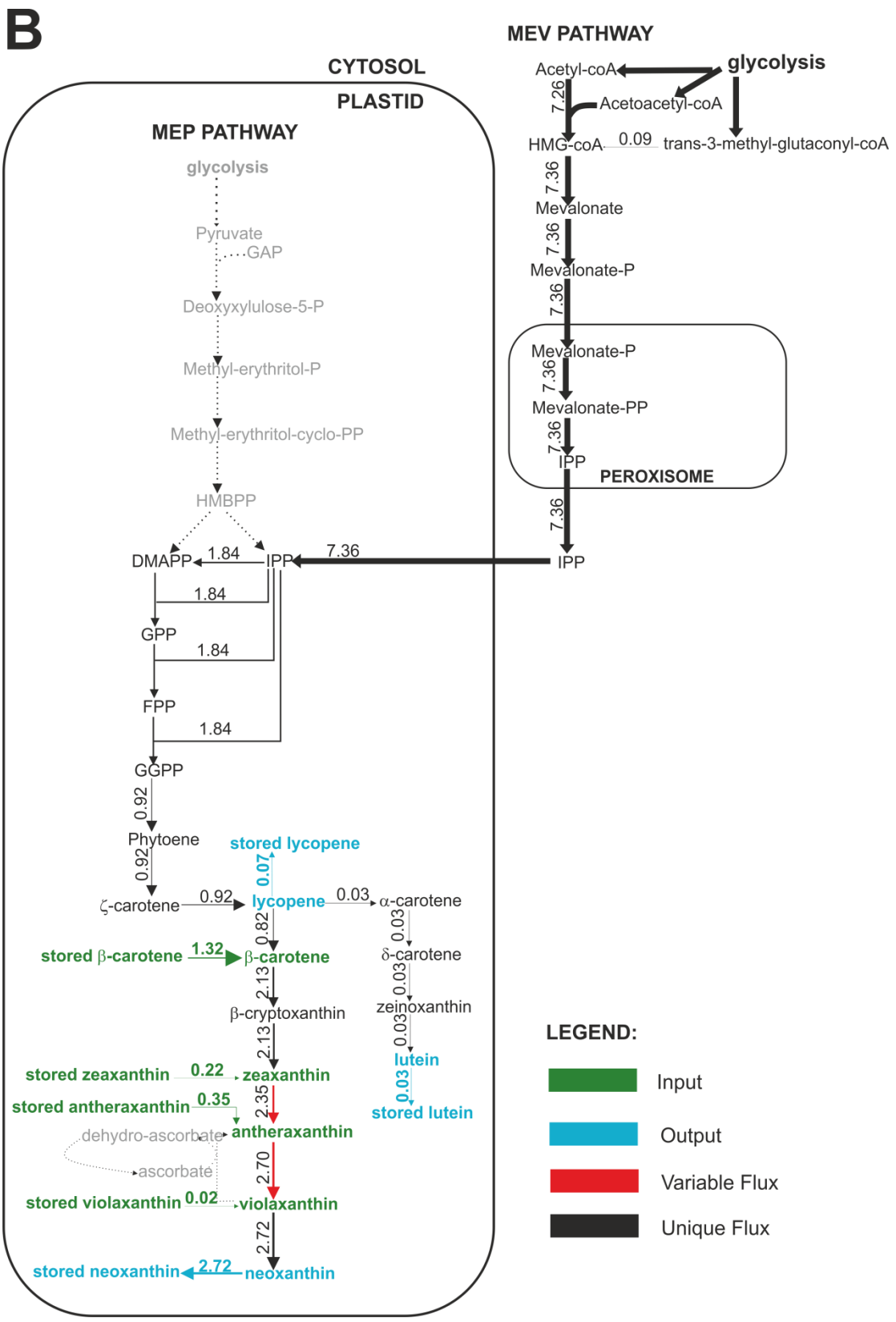

which the reaction must carry flux to reach optimality, or substitutable, by which the reaction can carry zero flux and substituted with another reaction(s). For these pathways, only zeaxanthin epoxidases during BR-TU were shown to be variable. For clarity purposes, not all steps in these pathways are shown. This diagram does not represent the whole network and it is not flux balanced. The thickness of the arrows has been scaled to the flux magnitude. Inputs and outputs are colour coded as green and blue respectively.

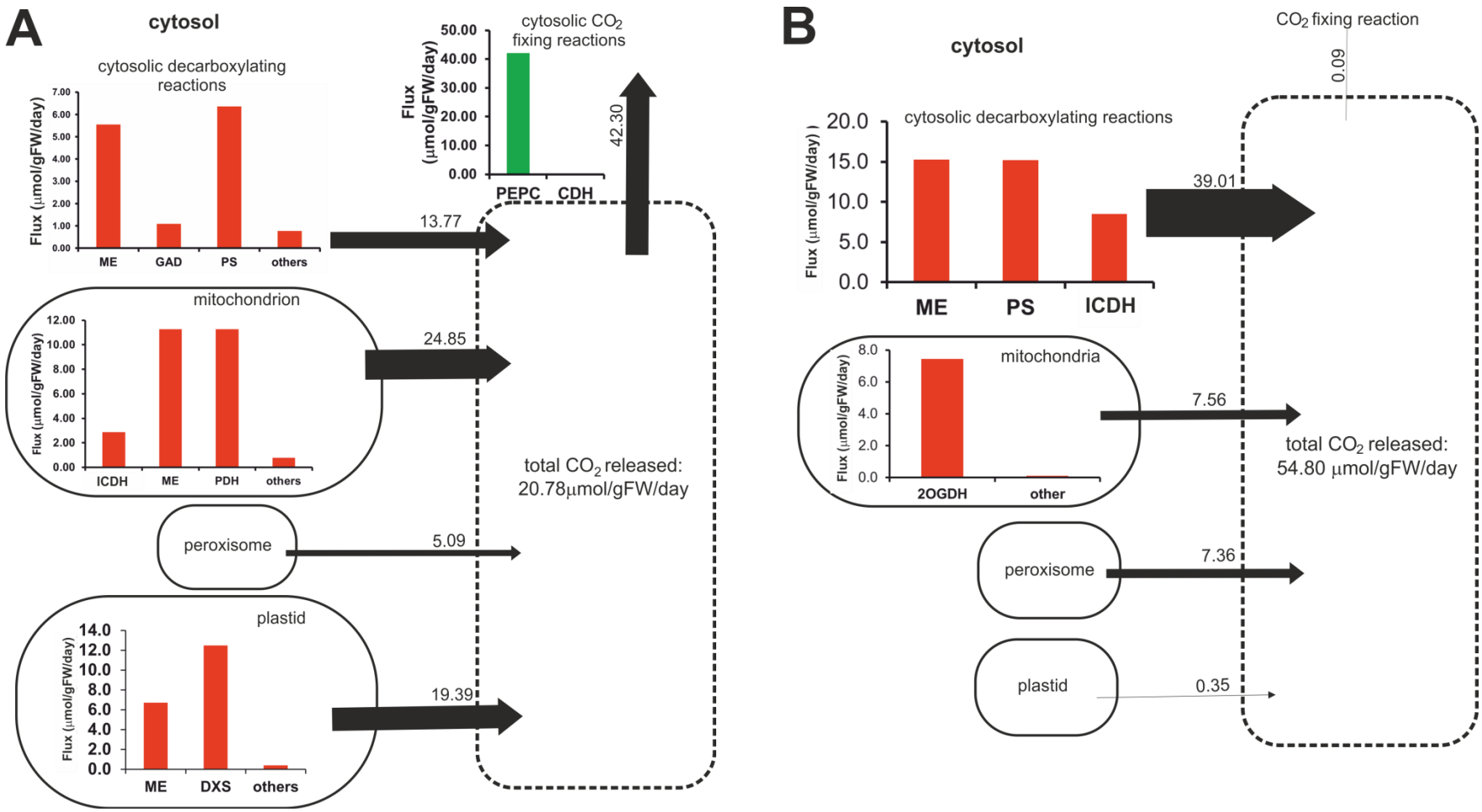

Figure 4.6. Total carbon release during tomato fruit ripening. CO_2 flux from different subcellular compartments into the cytosol is shown for (A) MG-BR; and (B) BR-TU stages of ripening. Higher carbon loss was predicted for BR-TU. Red bars shows flux levels for decarboxylating reactions and green bars represent flux levels for CO_2 fixing reactions. Abbreviations: PEPC (phospho*enol*pyruvate carboxylase); CDH (carbonic anhydrase); ME (malic enzyme); GAD (glutamate decarboxylase); PS (pyruvate synthase); ICDH (isocitrate dehydrogenase); PDH (pyruvate dehydrogenase); DXS (deoxyxylulose-5-phosphate synthase). The thickness of the arrows has been scaled to the flux magnitude.

Table 4.8. Closed system modelling of MG-BR with weighting factors of 1. The table below lists the fluxes predicted for the inputs and outputs during MG-BR when no additional influx of sugars and amino acids were allowed to enter the system. The objective function used during this modelling was minimisation of the sum of fluxes, and weighting factors of 1 were assigned to all of the reactions by default. No feasible flux distribution were found when both inputs and outputs were fixed with a single flux value and thus the constraints were relaxed by allowing flux ranges. The outputs were allowed a broad flux range of 0.0001mmol/gFW/day to infinity while the inputs were constrained with the same fluxes used during 'open system' modelling. 'Open system' column shows the fluxes used when modelling MG-BR with additional influx of carbons from the phloem. The value 'none' in the 'closed system' column means that the corresponding metabolite was not able to accumulate without additional carbon influx.

	input	open system	closed system
1	chlorophyll a	0.973	0.973
2	chlorophyll b	0.348	0.348
3	alanine	0.127	0.127
4	valine	0.092	0.092
5	leucine	0.074	0.074
6	lysine	0.052	0.052
7	methionine	0.051	0.051
8	threonine	0.043	0.043
9	arginine	0.038	0.038
10	tyrosine	0.026	0.026
11	histidine	0.014	0.014
12	asparagine	0.009	0.009
13	glycine	0.006	0.006
14	violaxanthin	0.005	0.005

	output	open system	closed system
1	citrate	18.551	0.001
2	glucose	2.4485	**none**
3	sucrose	1.5595	**none**
4	β-carotene	1.3413	0.027
5	GABA	1.0857	0.001
6	fructose	0.9848	**none**
7	malate	0.7700	0.001
8	glutamine	0.7450	0.001
9	aspartate	0.3654	0.508
10	glutamate	0.3391	0.001
11	antheraxanthin	0.3360	0.004
12	phenylalanine	0.2722	**none**
13	zeaxanthin	0.1932	0.001
14	putrescine	0.1867	0.001
15	myoinositol	0.1270	**none**
16	isocitrate	0.0699	0.001
17	succinate	0.0564	5.398
18	cysteine	0.0510	0.051
19	maltose	0.0504	**none**
20	serine	0.0478	0.001
21	shikimate	0.0371	**none**
22	ornithine	0.0347	0.037
23	dehydroascorbate	0.0332	**none**
24	glucose-6-phosphate	0.0087	**none**
25	sorbitol	0.0067	**none**
26	proline	0.0062	0.001
27	ribose	0.0060	**none**
28	glycerate	0.0058	0.001
29	caffeatte	0.0051	0.0473
30	isoleucine	0.0051	0.094
31	ascorbate	0.0049	**none**
32	fructose-6-phosphate	0.0048	**none**
33	fumarate	0.0044	0.001
34	trehalose	0.0041	**none**
35	myoinositol-1-phosphate	0.0031	**none**
36	glycerol-3-phosphate	0.0027	**none**
37	aconitate	0.0020	0.001
38	2-oxoglutarate	0.0009	0.001

Table 4.9. Closed system modelling of BR-TU with weighting factors of 1. The table below lists the fluxes predicted for the inputs and outputs during BR-TU when no additional influx of sugars and amino acids were allowed to enter the system. The objective function used during this modelling was minimisation of the sum of fluxes, and weighting factors of 1 assigned to all of the reactions by default. No feasible flux distribution were found when both inputs and outputs were fixed with a single flux value and thus flux ranges were used to allow more network flexibility. The outputs were allowed a broad flux range of 0.0001mmol/gFW/day to infinite while the inputs were constrained with the same fluxes used during 'open system' modelling. 'Open system' column shows the fluxes used when modelling BR-TU with additional influx of carbons from the phloem.

	input	open & closedsystem
1	citrate	15.024
2	GABA	2.684
3	beta carotene	1.317
4	malate	0.964
5	glutamine	0.521
6	antheraxanthin	0.352
7	sucrose	0.297
8	zeaxanthin	0.217
9	serine	0.153
10	myoinositol	0.127
11	glycine	0.115
12	valine	0.076
13	phenylalanine	0.071
14	isocitrate	0.064
15	shikimate	0.057
16	asparagine	0.034
17	mannitol	0.023
18	leucine	0.018
19	violaxanthin	0.018
20	glucose-6-phosphate	0.017
21	fructose-6-phosphate	0.006
22	glycerol-3-phosphate	0.005
23	fumarate	0.005
24	glycerate	0.004
25	histidine	0.003
26	arginine	0.003
27	tyrosine	0.003
28	aconitate	0.002
29	2-oxoglutarate	0.001

	output	open system	closed system
1	glucose	5.231	0.296
2	fructose	2.877	0.297
3	aspartate	1.989	0.001
4	glutamate	1.411	4.237
5	putrescine	0.202	0.001
6	alanine	0.176	0.001
7	maltose	0.090	0.001
8	methionine	0.080	0.001
9	lycopene	0.075	0.014
10	caffeatte	0.070	0.128
11	isoleucine	0.067	0.001
12	ribose	0.066	0.001
13	tyramine	0.044	0.003
14	threonine	0.035	0.001
15	lutein	0.030	0.001
16	ornithine	0.027	0.001
17	lysine	0.027	0.001
18	dehydroascorbate	0.026	0.001
19	cysteine	0.026	0.001
20	succinate	0.026	15.001
21	proline	0.011	0.001
22	neoxanthin	0.005	1.904
23	ascorbate	0.005	0.001
24	trehalose	0.003	0.001
25	sorbitol	0.000	0.042
26	myoinositol-1-phosphate	0.000	0.127

4.3 Discussion

4.3.1 Additional inputs required to model MG-BR and BR-TU

There was no feasible flux distribution found when both MG-BR and BR-TU were modelled in a closed system. The results of this work show that additional influx of sugars and amino acids were required for both MG-BR and BR-TU in order to find an optimal flux distribution that satisfied the objective function within the applied constraints. A possible explanation for this is that FBA relies on balancing metabolic fluxes and it is based on fundamental law of mass conservation, where the total amount of any compound being produced must be equal to the total amount being consumed at steady state. Hence, the metabolic network needed to balance as a constraint to the system in order to find an optimal flux distribution. In order to assess how additional influxes of sugars and amino acids balance the network, carbon fluxes for each input and output were calculated. Carbon fluxes are calculated by multiplying the number or carbon atoms in a compound with its degradation or accumulation rates. Tables 4.1, 4.2, 4.3 and 4.4 show the number of carbon atoms each input and output has and the corresponding carbon fluxes. A substantial amount of additional sugars and amino acids were required for MG-BR relative to BR-TU. This result can be explained by looking at the number of outputs and inputs during this transition. The outputs during this transition outnumbered the inputs by more than half. This in turn results in carbon imbalance to the metabolic network. The sum of carbon fluxes for the outputs was 226.34% greater than the inputs during MG-BR. As a consequence, a high influx of sugars and amino acids were required to match the difference. In contrast, in BR-TU the number

of inputs outnumbered the outputs by only two compounds and the total carbon flux difference between them was only 4.17%. As a consequence, BR-TU required a much smaller influx of amino acids and sugars than MG-BR.

4.3.2 Glycolytic flux during MG-BR and BR-TU

High glycolytic flux to supply intermediates and support energy demand during MG-BR

It was predicted that predominant fluxes were of those in glycolysis during MG-BR. This is consistent with experimental data, which show that glycolysis is upregulated in fruits that are yellow or colour breaking. For example, the abundance of transcripts encoding glycolytic enzymes increased both in non-climacteric fruits such as pineapples (*Ananas comosus*) (Koia et al., 2012), and in climacteric fruits such as papayas (*Carica papaya L*.) (Fabi et al., 2012) and tomatoes (Steinhauser et al., 2010). In these studies, it was suggested that the upregulation of glycolysis-related genes was linked to energy costs for phloem unloading of sugars and their storage in the vacuole. Furthermore, a study in ripening avocadoes (*Persea americana*) found that there were large increases in ATP production during ripening (Bennett et al., 1987). These findings suggests that high glycolytic activity during MG-BR may be due to a) accumulation of sugars for storage; b) the energetic costs to unload sugars from the phloem and their storage in the vacuole; and c) the energy demand for the metabolic processes occurring during MG-BR. In order to assess the extent to which glycolysis provides energy for these processes in the model, an energy budget was calculated. This is presented in Table 4.7. Cytosolic reactions were shown to consume the majority of the ATP produced

during MG-BR. Significantly, 56% of the total ATP produced in the cytosol was for the conversion of fructose into fructose-1,6-bisphosphate (FUBP). Further, 31% of the total ATP produced in the cytosol was used for phloem unloading and metabolite storage in the vacuole. Only 6 % of the ATP in the cytosol was exported into the plastid and peroxisome and the remaining ATP was consumed for other cytosolic metabolic processes. Meanwhile, phosphoglycerate kinase was responsible for the production of 12% of the total cytosolic ATP and the remaining 88% of cytosolic ATP was supplied by the mitochondria (Table 4.7). These findings may explain the correlation between high glycolytic flux predicted with the high influx of sugars from the phloem and the storage of metabolites in the vacuole. It is also interesting to note that the predicted glycolytic flux was distributed into two subcellular locations. This could suggest that the cytosolic glycolysis pathway alone might not be sufficient to support flux from 3-PGA to PEP required for storage metabolite accumulation during MG-BR. However, given that most of the GAP imported into the plastid was subsequently exported back into the cytosol as 3PGA, it is more likely that plastidic glycolysis mainly serves to supply a) ATP by phosphoglycerate kinase; and b) the intermediate for the synthesis of the MEP pathway precursor, DXP. This is in accordance with the physiological demands during MG-BR that accumulates carotenoids in preparation for BR-TU. The total amount of ATP produced in the plastid was 38.19 μmol/gFW/day and only 4.34% of that was imported from the cytosol. The majority of ATP was supplied by glycolysis. Significantly, 97% of this plastidic ATP was consumed for the reactions involved in MEP pathway. Indeed, it is not surprising that glycolysis can occur both in plastids and cytosol for higher plants. However, the extent to which reactions

are occurring in the plastid or/and in the cytosol depends on the physiological function of the cell (Andriotis et al., 2010; Munoz-Bertomeu et al., 2010; Prabhakar et al., 2010).

High glycolytic flux was not essential for the processes during BR-TU

In contrast to MG-BR, a low glycolytic flux was predicted for BR-TU. There are several explanations for this result. Firstly, the breakdown of citrate provides the carbon input for mitochondrial respiration, energy production and glutamate synthesis during BR-TU, large bypassing glycolysis. 100% of the ATP consumed by cytosolic reactions was derived from mitochondria. In terms of reductant, the cytosolic isocitrate dehydrogenase (ICDH) provided 23% of the NADPH consumed in the cytosol. The action of ICDH also participated in the conversion of citrate into glutamate, which was accumulated during BR-TU. This accords with the observation made by Gallardo et al. (1995) who hypothesised that upregulation of ICDH is connected to the accumulation of glutamate in ripe tomatoes (Gallardo et al., 1995). However, that study hypothesised that the main route to glutamate accumulation was through glutamate synthase (GOGAT). In the model, glutamate was mainly predicted to produce from cytosolic glutamate dehydrogenase, which also takes 2OG as its substrate. The accumulation of glutamate during fruit ripening was also associated with the synthesis of GABA through the GABA shunt (Cercós et al., 2006; Katz et al., 2011). Glutamate is converted into GABA, which is then converted into succinate that enters the TCA cycle (Figure 4.4). However, the BR-TU model did not reproduce this feature of metabolism, due the experimental constraints: GABA was constrained as an input during this

transition. However, glutamate was shown to convert into GABA through glutamate decarboxylase (GAD) during MG-BR where GABA was then accumulated (Table 4.2).

Another explanation for the low glycolytic flux in BR-TU is that the 20 out of the 29 inputs constrained during BR-TU were outputs during MG-BR. So while these metabolites were accumulating during MG-BR, necessitating a high glycolytic flux (Figure 4.3A), they are now going to be degraded during the next transition ensuring a lower glycolytic flux. The two most abundant metabolites accumulated during BR-TU were glucose and fructose and the production of these two sugars accounts for the majority of the flux in the upper part of glycolysis predicted during this transition. This is expected as sugar is an important constituent to the end fruit quality and has been shown to accumulate well into the ripe stage in tomato fruits (Carrari et al., 2006; Centeno et al., 2011; Roessner-Tunali et al., 2003).

4.3.3 Different ATP and metabolic demands between MG-BR and BR-TU led to contrasting TCA cycle flux modes

Cyclic TCA cycle during MG-BR

As discussed in section 4.3.2, glycolytic reactions during MG-BR had high demands for energy and consumed 69% of the total ATP produced during that transition (Table 4.7). However, the glycolytic reactions were not sufficient to supply all of the ATP required during this transition with only 12.50 μmol/gFW/day of ATP being produced accounting for only 8.7% of total ATP. Not surprisingly, the majority (92%) of ATP produced during MG-BR was

supplied by mitochondria (Table 4.7). The TCA cycle is widely known for its role in the generation of ATP through oxidative phosphorylation and to provide carbon skeletons for metabolic processes such amino acid and secondary metabolites synthesis. As such, a complete TCA cycle was predicted during this transition. It is interesting to note that the reactions in the cycle were predicted to carry different flux values. It was established that different parts of the TCA cycle contributed to different aspects of metabolism when it is embedded in a wider metabolic network (Sweetlove et al., 2010). Significantly higher flux was predicted for reactions between malate and citrate of the cycle suggesting that this part of the TCA cycle is mainly responsible for the NADH supply required for ATP synthesis and also to convert malate to citrate, which was the primary metabolite being exported from the mitochondria and also as the most abundant metabolite accumulated during this transition. Beyond citrate, the TCA cycle provided 2-OG, an important substrate for amino acid synthesis, such as glutamate that are accumulated during this transition. A much lower flux was predicted for these reactions between citrate and 2-OG and this might be due to the nature of the constraints in the transition, which had a higher rate of accumulation of citrate than glutamate. Another interesting finding from this predicted flux distribution is that malate was used as a substrate instead of pyruvate. This was also predicted by Steuer et al. (2007) in a model of TCA cycle metabolism who found that malate was favoured instead of pyruvate as it gave dynamic stability to the system. Indeed, when FVA was carried out for MG-BR, the malate-phosphate exchanger and the malate-citrate exchanger, the transporters that supplied the majority of the mitochondrial malate were identified as essential reactions. In further support of this idea, mitochondrial

variable reactions identified through FVA did not result in a different flux mode (ie non-cyclic flux or alternative TCA cycle substrate).

Non-cyclic TCA cycle flux during BR-TU

In contrast to MG-BR, a partial TCA cycle was predicted during BR-TU. As glycolytic flux was low during this transition, the cytosolic ATP demand was less than half relative that during MG-BR. Correspondingly, a partial TCA cycle was predicted during BR-TU. These findings are consistent with those found in an Arabidopsis model in which it was observed that a non-cyclic TCA cycle flux mode was predicted at low ATP demands and a complete cyclic flux mode was predicted when the ATP demand was increased (Poolman et al., 2009). In that study, the varying ATP demands were shown to be connected to glycolysis and the TCA cycle where more carbon was routed into these pathways when ATP demand was increased (Poolman et al., 2009). Non-cyclic flux modes were also shown to occur in other model (Poolman et al., 2009) as well as real systems (Rocha et al., 2010; Schwender et al., 2006) of higher plants subjected to different physiological demands. In roots of *Lotus japonicus* under hypoxia, a non-cyclic TCA cycle was observed and it was thought to be linked with amino acid accumulation and GABA degradation (Rocha et al., 2010). In that study, only the TCA cycle reactions between 2-OG and succinate, and malate dehydrogenase (in the direction of OAA to malate) were active. These reactions were linked to alanine accumulation by: a) pyruvate-dependent GABA transaminase (GABA-TP), which transaminated GABA into alanine; and b) alanine transaminase which converted pyruvate and glutamate into 2-OG and alanine. The production alanine was able to conserve a nitrogen store under

hypoxia and the partial TCA cycle was able to produce the ATP required for survival. The findings in that study are interesting because a) they suggest how a non-cyclic TCA cycle complements the metabolic network when constrained; and b) they showed how GABA degradation is linked with amino acid accumulation in the metabolic network. These observations also hold true in my model. In my model, 2-OG dependent GABA transaminase (GABA-TK) was predicted to be active during BR-TU instead of GABA-TP. GABA-TK enabled GABA to be transaminated into glutamate, which was then converted into OAA and aspartate through the action of aspartate aminotransferase (Figure 4.4). This allowed aspartate to accumulate during BR-TU, in which this metabolite was the highest amino acid to accumulate (Table 4.4) The preference for GABA-TK predicted during BR-TU for GABA degradation also accords with the observation by Akihiro *et al* (2008) who showed that GABA-TK was used instead of GABA-TP for GABA degradation in tomatoes (Akihiro et al., 2008).

In addition to amino acid accumulation, it has also been suggested that GABA degradation can contribute to organic acid accumulation (Yin et al., 2010). One route suggested involves the conversion of GABA into succinate via succinate-semialdehyde. Succinate was then able to convert into malate in the TCA cycle and exported to the cytosol to form pyruvate, which was then imported back into the mitochondria to be converted into citrate for storage (Yin et al., 2010). In my model, it was shown that succinate was converted into malate but instead of forming citrate it was converted into acetyl-coA in the cytosol for secondary metabolism during BR-TU. It is therefore likely that the fate of GABA and its degradation mechanism depends on the precise physiological demands of the cell. During BR-TU, aspartate and glutamate were

required to accumulate and precursor supply for secondary metabolism is critical. This combination of findings demonstrates that the model was useful to clarify uncertainties in the literature and suggests the most likely routes for a metabolic network optimised for resource-use efficiency

4.3.4 The MEP pathway is not the dominant pathway to produce secondary metabolites

One unanticipated finding was that the MEV pathway was predicted to be the sole IPP contributor for carotenoid biosynthesis during BR-TU. It is often observed in higher plants that the MEV pathway operates in parallel with the plastidic MEP pathway and usually the MEP pathway is dominant one (Bick & Lange, 2003; Lois et al., 2000; Rodríguez-Concepción et al., 2001; 2010). In fact, the MEP pathway was shown to be able to operate without the cytosolic MEV pathway in tomato seedlings when it was found that carotenoids were still produced when the MEV pathway was inhibited. However, carotenoids were not able to be produced when the MEP pathway was inhibited (Rodríguez-Concepción, 2010). Furthermore, expression of the gene for MEV decarboxylase was shown to be downregulated in yellow papaya fruits, which suggests that the MEV pathway is not dominant in ripening fruits (Fabi et al., 2012). A study in *Euglena gracilis* provides a rare example of MEV pathway as the sole route towards secondary-metabolite synthesis, in this case for phytol biosynthesis (Kim et al., 2004). As such, it was surprising to find MEV pathway as the dominant pathway to produce carotenoids during BR-TU. There are several possible explanations for this result. Firstly, carotenoids such as beta-carotene, zeaxanthin and violaxanthin are already produced during MG-BR thus

reducing the fluxes that would be needed to synthesise these products during BR-TU. Secondly, beta carotene, zeaxanthin and violaxanthin were constrained as inputs during BR-TU, supplying sufficient carbon inputs to produce neoxanthin at the downstream part of the carotenoid synthesis pathway. This in turn allows a lower supply of IPP for carotenoid synthesis and it was sufficient to produce all the carotenoids during BR-TU with only one pathway. Thirdly, on the question of why MEV was chosen as the predominant pathway instead of MEP pathway during BR-TU, it is likely that this is due to the objective function used during modelling. The objective to minimize the sum of fluxes tends to minimize the number of reactions during modelling. The minimum total number of steps to synthesise plastidic IPP from cytosolic pyruvate in the MEP and MEV pathway is 12 and 10 respectively. Furthermore, the MEP pathway requires cofactors such as oxidised and reduced ferredoxins, cytidine monophosphate (CMP), and cytidine triphosphate (CTP), which would require more fluxes to generate them. As such, if MEP pathway was to carry flux during BR-TU, fluxes were required to be routed into the plastid, which may result in increase of the total flux.

4.3.5 Climacteric respiration

Significantly higher CO_2 release was predicted during BR-TU relative to MG-BR. This is not surprising as respiration is known to rise at mature green stage and peak at breaker stage before declining as the ripe stage approaches in climacteric fruits such as tomatoes (Abdul-Baki et al., 1965), apples (Hulme et al., 1963), bananas (Hubbard et al., 1990) and avocadoes (Bennett et al., 1987). The respiratory climacteric rise is typically associated with the production

of ATP during ripening and hence past studies have suggested that the respiration rise during climacteric ripening is attributable to the increase in glycolytic and TCA cycle activity. However, contrary to expectations, the mitochondrial reactions were not the major CO_2 contributor during BR-TU in the model. Instead, cytosolic malic enzyme (ME), pyruvate synthase (PS) and ICDH contributed most of the CO_2 although low glycolytic flux was predicted during this transition (Figure 4.6). PS, which is the second highest cytosolic CO_2 contributor converts pyruvate into acetyl-coA and the reaction is not known to exist in higher plants but it is typically found in bacteria. The main acetyl-coA supplier in plants is thought to be ATP-citrate lyase (ACL), which also carried flux in this transition but much lower relative to PS. The presence of the PS reaction in the model is likely a result of a genome annotation error and should therefore be considered an artefact. Nevertheless, the presence of this reaction does not impact the current CO_2 release result greatly as BR-TU would still show to release higher CO_2 than MG-BR in the absence of PS, and indeed this was observed when both MG-BR and BR-TU were modelled without PS. Another important finding was that the lower CO_2 release during MG-BR was due to CO_2-fixing phospho*enol*pyruvate carboxylase (PEPC) in the cytosol. PEPC was predicted to carry high flux during MG-BR and thus fixed a considerable amount (67%) of CO2 produced during MG-BR. Unlike MG-BR, PEPC did not carry flux during BR-TU. Therefore, BR-TU was found to release higher CO_2 although MG-BR produced 13% more CO_2 but most of the CO_2 was fixed by PEPC. Thus the model provides new insight into the nature of the climacteric, suggesting that it may not be due to increased TCA cycle flux, but rather the result of a rebalancing between CO_2-evolving and CO_2-fixing

reactions in the cytosol. This emphasises that CO_2 production is a network property and does not necessarily reflect only TCA cycle flux (Sweetlove et al., 2013)

4.3.6 Closed system modelling of MG-BR and BR-TU predicted an altered metabolite composition for ripening tomato fruits

Glucose, sucrose and fructose were not able to accumulate during MG-BR when no additional influxes of carbon were allowed to enter the metabolic network (Table 4.8). During BR-TU, however, glucose and fructose were able to accumulate but with significantly low fluxes. This indicates that sugars are neither accumulating nor degrading during MG-BR and slightly increased during BR-TU. Together, these findings suggest that in off-vine ripening tomatoes, where no additional carbons are supplied to the fruit, sugar content is likely to remain constant or accumulate at low rates during ripening. It also suggests that sugar composition in off-vine ripened tomatoes is significantly different and may result in a significantly lower sugar content than on-vine ripened tomatoes. Consistent with this prediction, a metabolic profiling study of on- and off-vine ripened tomatoes found that sugars are significantly reduced in off-vine ripened tomatoes (Sorrequieta et al., 2013).

Another significant finding from modelling MG-BR and BR-TU in a closed system is that succinate was predicted to accumulate at the highest rate of all accumulated metabolites. During MG-BR, this may be the result of chlorophyll degradation as succinate is the end product of phytol degradation during BR-TU, high accumulation of succinate may be due to citrate and GABA

degradation. High accumulation of glutamate during this transition further corroborates this idea. However, these findings were not in agreement with the metabolic profiles studied in off-vine ripened tomatoes. Succinate was found to be at very low levels and GABA was present at relatively high levels, indicating that GABA was not degraded rapidly as shown for on-vine ripened tomatoes (Sorrequieta et al., 2013).

4.4 Summary

This chapter has demonstrated that the tomato metabolic model has all the reactions needed to represent the known metabolic process during ripening. The purpose of the chapter was to model the metabolic processes that occur during MG-BR and BR-TU. It was shown that additional influx of sugars and amino acid was required to obtain an optimal flux distribution that satisfied the objective function within the applied constraints. It was also shown that both ripening transitions showed markedly different flux distributions and it was attributable to its different metabolic requirement. The results of this study indicate that the flux distribution for MG-BR was centred on the glycolytic pathway and TCA cycle, which provided the necessary intermediates and energy for the metabolic processes occurring during this transition. It was also shown that different metabolic demand of the transition predicted contrasting flux distribution. This is the first study to report the predicted underlying metabolic changes during tomato fruit ripening using a metabolic model.

Chapter 5: Modelling the metabolic changes when lycopene accumulation is increased during BR-TU

5.1 Introduction

Carotenoids have antioxidant properties that have been shown to reduce the risk of cardiovascular diseases, cancer and other chronic diseases (Agarwal & Rao, 2000; Krinsky & Johnson, 2005; Rao & Rao, 2007; Voutilainen et al., 2006). Carotenoids are responsible for the yellow to red colour in some fruits and vegetables that are central to the human diet (Voutilainen et al., 2006). In tomatoes, lycopene is the most abundant carotenoid and there has been heightened interest in increasing the production of this compound in tomatoes and other organisms such as *Escherichia coli* (*E. coli*), for its health benefits (Agarwal & Rao, 2000; Fraser et al., 2007, 2002; Rao & Rao, 2007; Yoon et al., 2006).

Carotenoids, such as β-carotene, lycopene, lutein and xanthophylls such as zeaxanthin, antheraxanthin and violaxanthins are synthesised from the universal terpenoid precursors isopentenyl diphosphate (IPP) and dimethylallyl diphosphate (DMAPP). These precursors can be produced from two independent terpenoid synthesis pathways: a) the plastidic methylerythritol phosphate (MEP) pathway; and b) the cytosolic mevalonate (MEV) pathway. Certain algae and higher plants such as tomatoes contain both biosynthetic pathways, while bacteria contain either the MEP or the MEV pathway such as in *E. coli* and in gram-positive coccis respectively (Eisenreich et al., 2001; Lois et al., 2000; Wilding et al., 2000).

Several studies have manipulated these biosynthetic pathways to increase the accumulation of desired terpenes or carotenoids. For example, the MEP pathway was manipulated by overexpressing genes that encode for deoxyxylulose-5-phosphate synthase (DXS) (Kim & Keasling, 2001; Matthews & Wurtzel, 2000) and deoxyxylulose-5-phosphate reductase (DXR) (Kim & Keasling, 2001), which led to increased production of deoxyxylose-5-phosphate (DXP) and MEP respectively in *E. coli*. Increased flux through the MEP pathway and thus increased supply of IPP and DMAPP enabled lycopene to accumulate more than six-fold higher than in the control strain (Kim & Keasling, 2001). In another study, the entire MEP pathway was reconstructed in *E.coli* to produce lycopene (Farmer & Liao, 2001, 2000). In this engineered *E.coli* strain, the production of lycopene was further increased by overexpressing the gene encoding phospho*enol*pyruvate synthase (PPS). This redirected metabolic flux towards the production of glyceraldehyde-3-phosphate (GAP), increasing its level (Farmer & Liao, 2001). The hypothesis was that the levels of the MEP pathway precursors – pyruvate and GAP – were imbalanced and this resulted in low lycopene production in *E. coli*. Thus, by elevating GAP levels, the precursors become balanced, which resulted in increased fluxes through the MEP pathway. However, redistributing the fluxes for pyruvate production and overexpressing the glycolytic gene must have had a limiting effect on the network.

To overcome these limitations, another carotenoid engineering strategy adopted was to bypass the native MEP pathway by cloning and expressing the MEV pathway genes as shown in *E. coli* (Martin et al., 2003; Pitera et al., 2007; Yoon et al., 2006; Zurbriggen et al., 2012) and *Synechocystis sp.* PCC 6803

(Bentley et al., 2014). This was first achieved by Martin et al. (2003) by expressing the MEV pathway genes from *Saccharomyces cerevisiae* in *E. coli* and increasing the production of amorphadiene, the precursor for the antimalarial drug artemisinin. Because all terpenoids are derived from the universal precursors IPP and DMAPP, expression of the MEV pathway in *E. coli* was able to significantly increase supply to the precursor pool when MEV was introduced exogenously. It was shown that levels of amorphadiene increased significantly in *E. coli* to such a high level that cell growth was inhibited. An adverse effect on growth was also shown in another study that adopted the same terpene engineering strategy.

In higher plants, more limited genetic engineering has been implemented, mainly focusing on manipulation of the reactions beyond IPP and DMAPP. For example, the phytoene synthase gene (*psy*) has been constitutively expressed in tomatoes to increase the accumulation of lycopene and other carotenoids (Fraser et al., 2007, 2002; Fray et al., 1995). This directly increased the levels of terpenoid precursors farnesyl diphosphate (FPP), geranyl diphosphate (GPP) and geranylgeranyl diphosphate (GGPP) and thus enabled increased carotenoid production. Although the general phenotype of the fruit was not altered, dramatic changes in pigmentation were exhibited at the mature green stage instead of breaker stage. Hence, the genetic manipulation must have altered the metabolic composition of the fruit and may result in a lower fruit quality.

These genetic manipulation strategies mentioned above only focused on a small part of the network. Some have shown adverse effects on growth

despite the increased abundance of terpenoids (Fraser et al., 2007; Martin et al., 2003; Yoon et al., 2006). More extensive network manipulation has been shown to improve terpenoid production and reduce the pleiotropic effects on the organism. For example, metabolic flux imbalances- where metabolites produced were not consumed elsewhere in the network- were observed in *E. coli* engineered to contain the MEV pathway (Ma et al., 2011; Pitera et al., 2007). To alleviate the metabolic bottleneck, the hydroxymethylglutaryl-coA reductase (*HMGR*) gene was expressed to allow endogenous acetyl-coA to be consumed by the MEV pathway, thus increasing mevalonate production and restoring metabolic balance to the network (Ma et al., 2011; Pitera et al., 2007).

These observations show that by manipulating only a small part of the metabolic network, other parts of the network may be affected and altered, causing adverse effects on growth. However, it is impossible to predict these effects on a larger network scale without computational power. One study used a Flux Balance Analysis (FBA) model to design its genetic manipulation strategy (Alper et al., 2005). They used a genome-scale model of *E.coli* to identify optimal gene knockouts by modelling the network to increase the production of lycopene with minimal metabolic rearrangements, which minimises the adverse effect on growth. The model predicted three-gene knockouts, which they tested experimentally and yielded a 37% increase in lycopene production relative to the parental strain (Alper et al., 2005).

Minimising adverse effects to growth and phenotypes is important for engineered crop plants such as tomatoes. This is because good overall fruit quality is highly sought by consumers. Hence, it is important to minimise

alterations to the metabolic composition yet increase the compounds which are beneficial to health. Modelling the tomato metabolic network can be the first step to obtaining a systems perspective on the changes that can occur when lycopene production is increased.

In my study, the tomato metabolic network was used to observe underlying metabolic changes that occur when lycopene production is forced to increase during BR-TU. BR-TU was chosen as it is established that lycopene begins to accumulate during breaker and is abundant during the turning stage in ripening tomatoes (Baxter et al., 2005; Carrari et al., 2006). Therefore, BR-TU was modelled with the specific combination of constraints described in Chapter 4. Varying lycopene accumulation rates were imposed to further constrain the network.

5.2 Results

5.2.1 Modelling approach

The 'lycopene scan'

The aim of the work in this chapter was to predict the metabolic changes that occur during BR-TU when the lycopene accumulation rate was increased. A 'lycopene scan' was set up where the BR-TU transition was modelled iteratively using a different fixed value for the lycopene accumulation rate for each iteration. An optimal flux distribution was predicted for each successful iteration in the lycopene scan, which satisfied the objective function to minimise the sum of fluxes within the applied constraints. Lycopene accumulation rates used for the scan were from 0.0746 to 1.5 μmol/gFW/day. This starting rate of 0.0746 μmol/gFW/day was chosen as this was the experimental lycopene accumulation flux value used to model BR-TU in Chapter 4. Although the maximum limit for the scan was set to 1.5 μmol/gFW/day, the rate of lycopene accumulation of 0.9909 μmol/gFW/day was the maximum rate which could be obtained within the constraint imposed on the model: higher lycopene accumulation rates did not yield a solution to the modelling problem.

Metabolic constraints

The metabolites used to constrain BR-TU in this work are the same as those used for modelling BR-TU in Chapter 4. For clarity, the optimal flux distribution obtained from modelling BR-TU in Chapter 4 is referred to as 'normal' BR-TU from here onwards. When BR-TU was constrained with a

lycopene accumulation rate greater than 0.0746 μmol/gFW/day and the inputs and outputs were constrained with a fixed flux rate as described for 'normal' BR-TU, no feasible flux distribution could be found. As a result, with the exception of lycopene accumulation rate, the metabolic inputs and outputs were allowed to vary within 10% of the experimental flux (Figures 5.1 and 5.2). The 10% range was chosen as it was deemed to be wide enough to allow flexibility to the network to produce more lycopene, but small enough to maintain the metabolic composition.

Flux variability analysis (FVA)

To identify variable fluxes in the predicted flux distributions, FVA was carried out for each lycopene accumulation rate used in this work. In this analysis, all inputs and outputs during BR-TU were allowed to vary within a 10% range of the experimental flux, except for lycopene accumulation which was fixed with a single flux value corresponding to the value used in the lycopene scan. Variable reactions are highlighted as dashed lines in the flux maps presented in this chapter.

5.2.2 A 13.2-fold increase in lycopene accumulation was achieved

From the main lycopene scan, 0.9909 μmol/gFW/day was shown to be the maximum lycopene accumulation rate for which it was possible to satisfy the objective function within the applied constraints. This resulted in a 13.2-fold increase in lycopene accumulation. No feasible flux distribution could be found for a greater lycopene accumulation rate in the scan. Figure 5.3 summarises the result of the lycopene scan using the aforementioned constraints. As is shown

in the figure, 13 optimal flux distributions with changing objective values were predicted in the scan. For future reference, selected optimal flux distributions in the lycopene scan were marked with A to G and will be referred to as 'flux distribution A' to 'flux distribution G' respectively (Figure 5.3).

5.2.3 Lycopene can accumulate to the 'normal' level with a lower sum of flux

Both normal BR-TU and flux distribution A generated the same lycopene accumulation rate of 0.0746 μmol/gFW/day. However, a lower objective value (sum of flux) was predicted for flux distribution A (Figure 5.3). This was expected as the constraints were allowed to vary in the lycopene scan thus creating more flexibility in the metabolic network to distribute the fluxes. In order to assess how a lower objective value can be achieved with the same lycopene accumulation rate, optimal flux distributions of normal BR-TU and flux distribution A were compared. Table 5.1 lists the numbers of reactions with altered fluxes between two flux distributions in the lycopene scan. Flux was increased for only five reactions, while flux decreased for 86 reactions for flux distribution A relative to normal BR-TU. Ten reactions were labelled 'switched on' as they only carried flux at flux distribution A while eight reactions were labelled 'switched off' as they only carried flux during normal BR-TU. Fluxes of the remaining 229 reactions did not change between normal BR-TU and flux distribution A. The top five inputs (citrate, GABA, β-carotene, malate, sucrose (from the phloem) and glucose (from the phloem), and the top four outputs (glucose, fructose, neoxanthin and aspartate) all had decreased flux at flux distribution A (Figures 5.1 and 5.2). Only glutamine (input) and glutamate

(output) were found to increase their fluxes while the remaining constraints did not change their fluxes (Figures 5.1 and 5.2).

The decrease of fluxes from the main constraints resulted in a decrease in the predominant fluxes in the cytosol, plastid and mitochondria for flux distribution A as shown in Figures 5.4 and 5.5, which suggests how a lower objective value (sum of flux) at flux distribution A was achieved. It is evident in Figure 5.4 that the decrease in the citrate input flux (13.52 μmol/gFW/day at flux distribution A from 15.02 μmol/gFW/day during normal BR-TU) resulted in decreased fluxes into the mitochondria via OAA and 2-OG (Figure 5.4). In the mitochondria, fluxes through the partial TCA cycle were reduced, resulting in 10.4% lower mitochondrial ATP production (36.14 μmol/gFW/day at flux distribution A in relation to 40.33 μmol/gFW/day at normal BR-TU) (Figure 5.5). The decrease in mitochondrial fluxes also reduced fluxes of malate exported into the cytosol (9.00 μmol/gFW/day at flux distribution A from 10.10 μmol/gFW/day during normal BR-TU), which in turn decreased fluxes towards production of cytosolic MEV pathway precursors (Figures 5.4 and 5.5). Reduced fluxes through the MEV pathway were sufficient to produce lycopene at 0.0746 μmol/gFW/day as the accumulation of neoxanthin was also reduced, diminishing the need for higher fluxes in the carotenoid synthesis pathway (Figure 5.6). The only reaction that significantly increased was the plastidic NAD-dependent malate dehydrogenase (6.01 μmol/gFW/day at flux distribution A in relation to 4.03 μmol/gFW/day during normal BR-TU) that produced plastidic OAA to compensate for the reduced flux of the plastidic NADP dependent malate dehydrogenase (Figure 5.7).

5.2.4 Up to 5-fold increase in lycopene accumulation was achieved with minimal flux changes.

Lycopene accumulation increased 5-fold with a lower objective value

Between flux distributions A and B, lycopene accumulation increased 5-fold. It is interesting to note that the objective value at flux distribution B was actually slightly lower than at flux distribution A. This is unexpected- it would seem more likely that the sum of fluxes would increase with increasing lycopene accumulation. Table 5.1 shows that when comparing flux distribution A to flux distribution B, only 20 reactions had different flux values. Seven reactions had increased fluxes while eight reactions had decreased fluxes at flux distribution B in relation to flux distribution A. Figure 5.8 compares these fluxes in flux distribution A and in flux distribution B. Three of the reactions with increased fluxes are involved in producing cytosolic NADP and oxidised thioredoxin. Figure 5.8 shows that by increasing these three reactions to supply the cytosolic reductants and co-factors, the network was able to reduce the fluxes of eight other reactions (highlighted in purple). In turn, input fluxes of β-carotene, zeaxanthin and antheraxanthin were increased in the lower part of the carotenoid synthesis pathway to satisfy the constraint of neoxanthin accumulation. This allowed the accumulation of lycopene to be increased without changing the fluxes of the upper part of the carotenoid synthesis pathway and the MEV pathway.

This suggests that by allowing the constraints to vary within a range, the network fluxes can be more optimally distributed to achieve the objective function, which was to minimise the total fluxes required and to satisfy the

applied constraints during BR-TU. In this instance, not only do these changed fluxes account for only a small portion (18%) of the overall fluxes at flux distribution B, they allowed the network to maintain its cytosolic reductant and cofactor pool while increasing lycopene accumulation within a lower objective value than A (Figure 5.3).

Lycopene accumulation increased 2.2-fold with constant objective values

As already mentioned, it would be expected that the objective value would change with increasing lycopene accumulation in the lycopene scan. Therefore, it was interesting to find that a constant objective value was obtained for three optimal flux distributions that saw a 2.2-fold increase of lycopene accumulation between them (Figure 5.3). Further analysis of the reactions in these three flux distributions (marked with an asterisk in Figure 5.3) revealed that they not only share the same active reactions (reactions that carried flux) but that the flux values were identical in all three distributions, except for just four reactions. These four reactions are in the carotenoid synthesis pathway – a lycopene transporter, a β-carotene transporter and two lycopene β-cyclases that form γ- and β-carotene respectively (Figure 5.9). As is shown in this figure, the flux of both lycopene β-cyclases was reduced. Conversely, the β-carotene input flux increased with lycopene accumulation in the three flux distributions. These findings suggest that lycopene is accumulated at the expense β-carotene production. However, the increased input flux of β-carotene was able to compensate for the reduced fluxes and supplied up to 57% of the fluxes required to accumulate neoxanthin within the three flux distributions (Figure 5.9). These findings were not surprising as these flux distributions were

constrained by changes in biomass components as well as the objective function which aimed to minimise the sum of fluxes.

5.2.5 MEP pathway is activated when lycopene accumulation increased 9.2-fold.

There was up to 7.8-fold increase of lycopene accumulation for flux distribution C compared with normal BR-TU (see Figure 5.3), the MEV pathway was shown to be the sole contributor of IPP and DMAPP for carotenoid biosynthesis. However, at 1.2-fold higher lycopene accumulation (flux distribution D), the MEP pathway was active and operated alongside the MEV pathway to supply DMAPP (Figure 5.10). This suggests that the MEV pathway has reached its threshold within the applied constraints at flux distribution D to supply the precursors for carotenoid synthesis. However, the MEP pathway at flux distribution D only supplied DMAPP and at a relatively lower flux than the MEV pathway (Figure 5.10). The MEP pathway supplied only 5% of the total DMAPP, the rest being supplied by the MEV pathway. The fluxes to produce lycopene increased 11% at flux distribution D in relation to flux distribution C. This enabled 65% of the flux from lycopene to be distributed towards storage and the remaining fluxes to be routed to the lower part of the carotenoid biosynthesis pathway.

Interestingly, fluxes in the lower part of the carotenoid synthesis pathway at flux distribution D did not change in relation to flux distribution C (Figure 5.10). A possible explanation for this might be that the input fluxes of β-carotene, zeaxanthin, antheraxanthin and violaxanthin were already sufficient to

supply fluxes to produce neoxanthin for storage (Figure 5.10). These findings suggest that the MEP pathway was required to increase supply of the precursor pool with increasing lycopene accumulation at flux distribution D onwards.

5.2.6 Increased demand for reductant when lycopene accumulation increased 13.2-fold leads to a radically altered flux distribution

A substantial increase of objective value was observed when lycopene accumulation increased to 13- and 13.2 fold at flux distributions F and G respectively (Figure 5.3). Figure 5.11 compares the plastidic, cytosolic and mitochondrial reactions at flux distribution F and G. It is apparent from this figure that the predominant fluxes that increased in flux distribution G were of cytosolic and mitochondrial aminotransferases. This result may be explained by the fact that the metabolic network was constrained to an objective function which minimised the sum of fluxes while satisfying the demand to increase mitochondrial ATP and plastidic reductants (Figure 5.11).

In Figure 5.11, the dominant route for the uptake of Pi into the mitochondria was shown to change at flux distribution F and G. At flux distribution F, the predominant fluxes for the uptake of Pi into mitochondria was in exchange with proton (40.90 μmol/gFW/day) but at flux distribution G, this flux decreased significantly to 2.22 μmol/gFW/day and the main route for the uptake of Pi into mitochondria was replaced with an OAA transporter, which carried 46.93 μmol/gFW/day. This switch in the routes for Pi uptake decreases the requirement for available mitochondrial proton at flux distribution G and this lead to the decrease of fluxes through the electron transport chain (ETC).

Interestingly, the mitochondrial ATP generated at flux distribution G was 2% higher than at flux distribution F. This suggests that the amount of proton was reduced to an amount sufficient for mitochondrial ATP production and that the change in the route of how Pi enters the mitochondria was a way to minimise the fluxes in the mitochondria, a mechanism to cope with increasing fluxes in other parts of the network.

At flux distribution G, the uptake of Pi into the mitochondria in exchange with OAA has led to a radical distribution of high fluxes that involved several mitochondrial and cytosolic aminotransferases (Figure 5.11). The change in the plastidial flux distribution at flux distribution E and F suggests that the increased supply for cytosolic OAA is linked with the increased demand for plastidial reductant as lycopene accumulation is increased (Figure 5.12). The increased pool of cytosolic OAA is then used to produce malate, which is imported into the plastid to generate plastidial reductants.

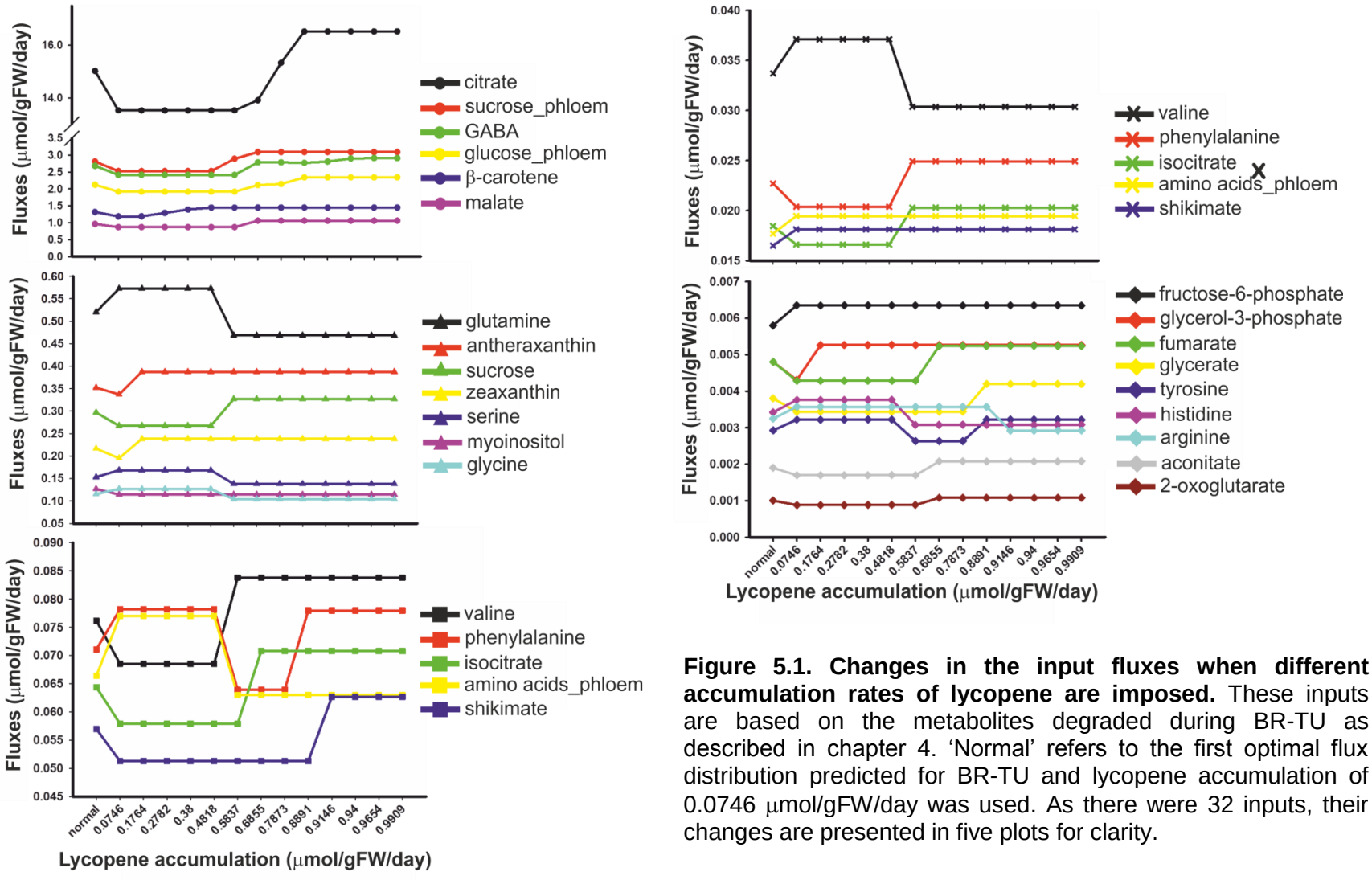

Figure 5.1. Changes in the input fluxes when different accumulation rates of lycopene are imposed. These inputs are based on the metabolites degraded during BR-TU as described in chapter 4. 'Normal' refers to the first optimal flux distribution predicted for BR-TU and lycopene accumulation of 0.0746 μmol/gFW/day was used. As there were 32 inputs, their changes are presented in five plots for clarity.

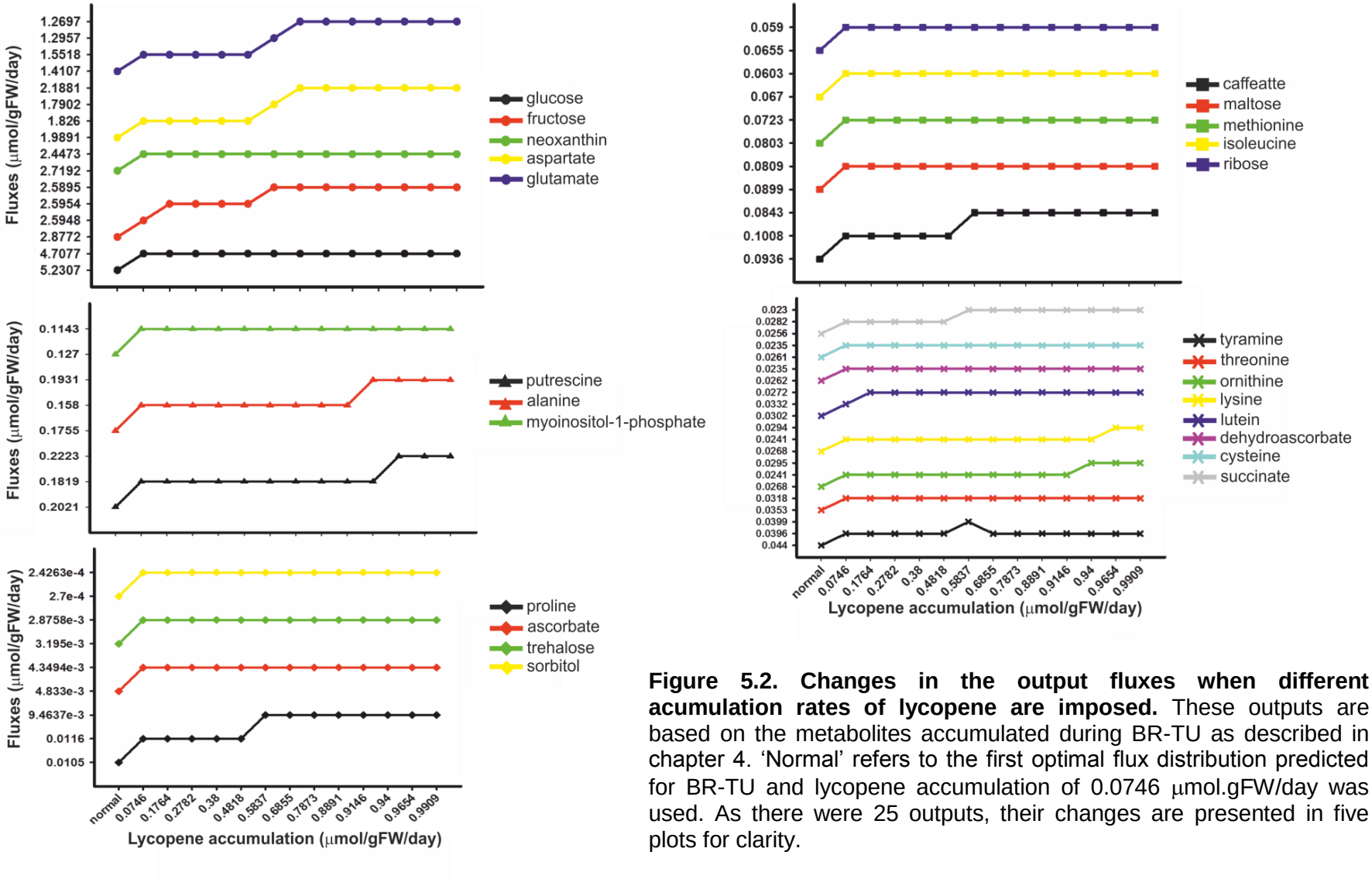

Figure 5.2. Changes in the output fluxes when different acumulation rates of lycopene are imposed. These outputs are based on the metabolites accumulated during BR-TU as described in chapter 4. 'Normal' refers to the first optimal flux distribution predicted for BR-TU and lycopene accumulation of 0.0746 μmol.gFW/day was used. As there were 25 outputs, their changes are presented in five plots for clarity.

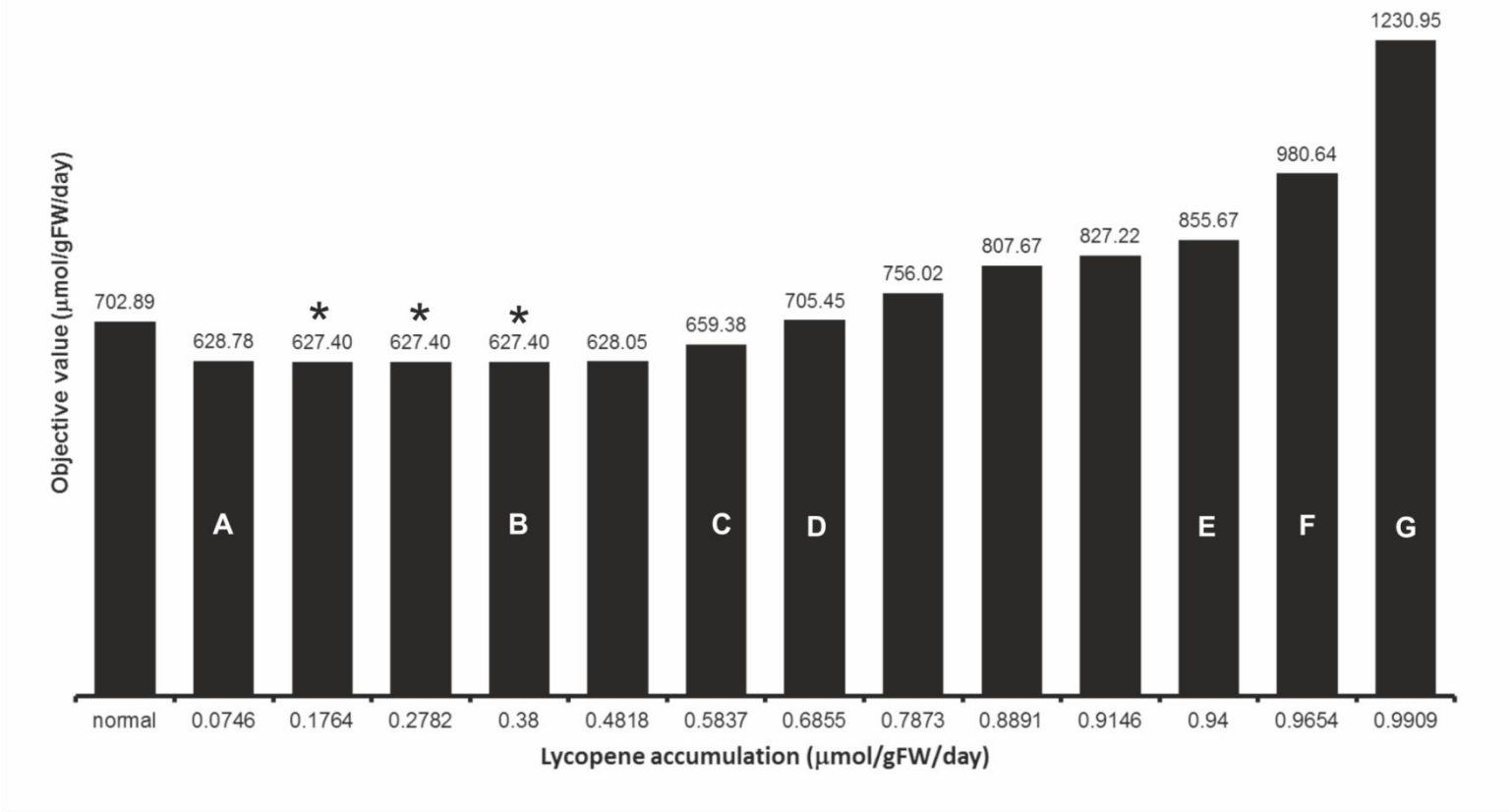

Figure 5.3. The objective value (sum of fluxes) at different lycopene accumulation rates. 'Normal' is the optimal flux distribution obtained when BR-TU was modelled with fixed input and output fluxes as described in Chapter 4. In this lycopene scan, BR-TU was modelled with varying lycopene accumulation rates starting from 0.0746 μmol/gFW/day, which was the lycopene accumulation rate used during normal BR-TU. Highest lycopene accumulation was at 0.9909 μmol/gFW/day and no feasible flux could be found thereafter. The inputs and outputs in this lycopene scan were allowed to vary within a 10% range of the experimental flux. Asterisk (*) marks three flux distributions with constant objective value. For clarity, selected optimal flux distributions were marked with A – G to represent its corresponding section when it is discussed in the text.

Table 5.1. Number of reactions that changed when two flux distributions with different lycopene accumulation rates is compared to each other. The selected optimal flux distribution is as marked in Figure 5.3. For columns two to six, the flux change categories presented here corresponds to the change that was observed in the flux distribution with a higher lycopene accumulation rate except for column 'normal/A'. For example in the 'A/B' column, 7 reactions had higher fluxes in flux distribution B in relation to flux distribution A. For column 'normal/A', these results correspond to flux distribution A. 'Switched on' means that the reactions are only active in in the flux distribution with higher lycopene accumulation while 'switched off' means the reactions are only active in the flux distribution with lower lycopene accumulation.

Flux change categories	Lycopene scan optimal flux distributions (see Figure 5.3)				
	normal / A	A / B	C / D	E/ F	F / G
constant	229	310	214	230	276
increased	5	7	85	51	44
decreased	86	13	21	43	21
switched on	10	0	21	17	0
switched off	8	0	7	22	0

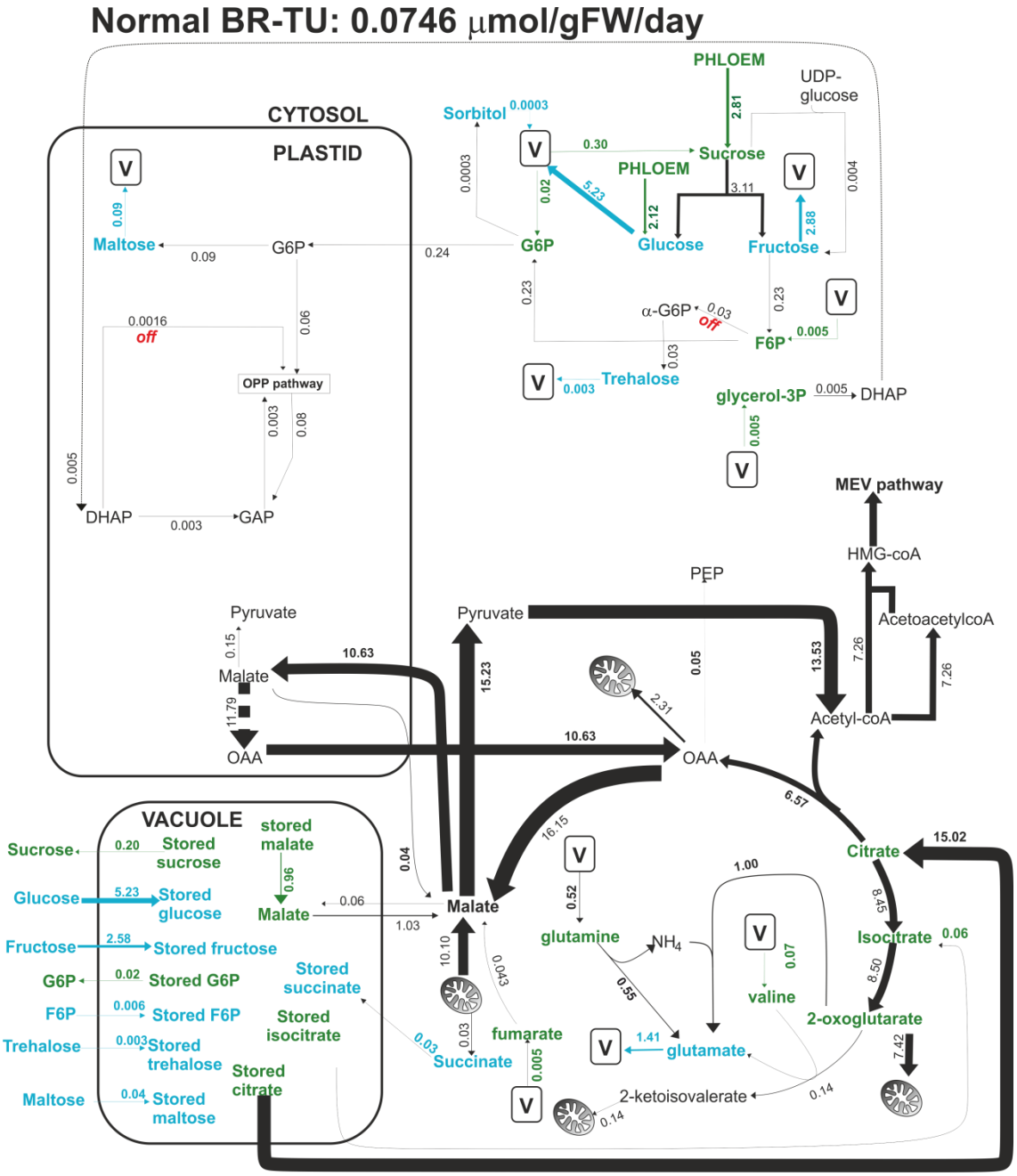

Figure 5.4. Glycolytic and plastidic fluxes that changed at flux distribution A relative to normal BR-TU. Both normal BR-TU and flux distribution A accumulate lycopene at 0.0746 μmol/gFW/day. However a lower objective value was predicted for flux distribution A. The thickness of these arrows is scaled to the flux magnitude. Inputs and outputs are colour coded as green and blue respectively. Reactions that increased and decreased at flux distribution A are coloured orange and purple respectively. Reactions labelled 'off' in 'normal' BR-TU means that the reaction is not carrying flux in flux distribution A while reactions labelled 'on' in flux distribution A means that the reaction did not carry flux in 'normal' BR-TU. For clarity, small mitochondrias and

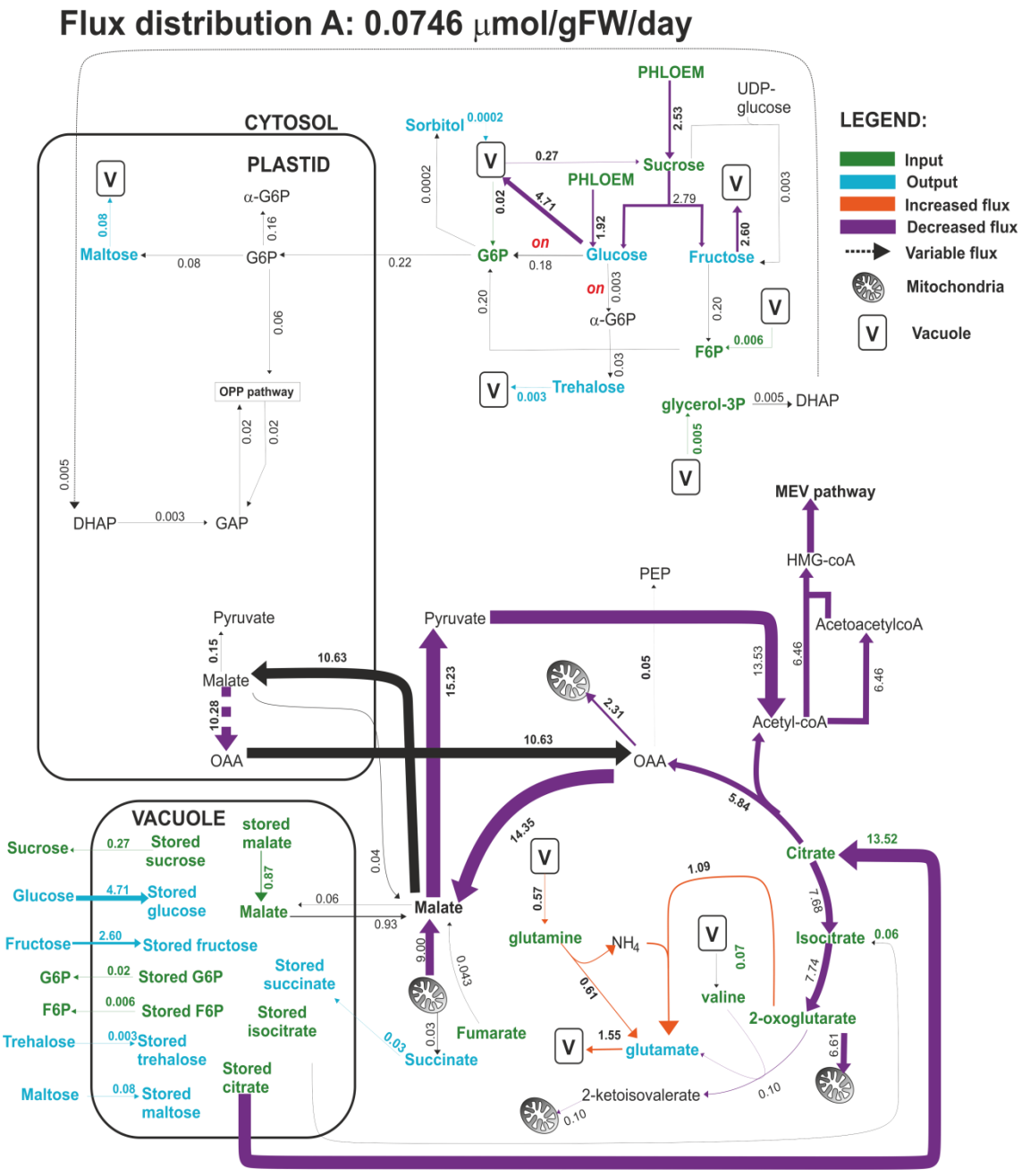

vacuoles are used: they do not represent separate organelles. Reactions that are identified to be variable from FVA are represented with dashed arrows. Abbreviations: G6P (glucose-6-phosphate); OPP (oxidative pentose phosphate); DHAP (dihydroxyacetone phosphate); GAP (glyceraldehyde-3-phosphate); OAA (oxaloacetate); F6P (fructose-6-phosphate); glycerol-3P (glycerol-3-phosphate); HMG-coA (hydroxymethylglutaryl-coA; PEP (phospho*enol*pyruvate); MEV (mevalonate)

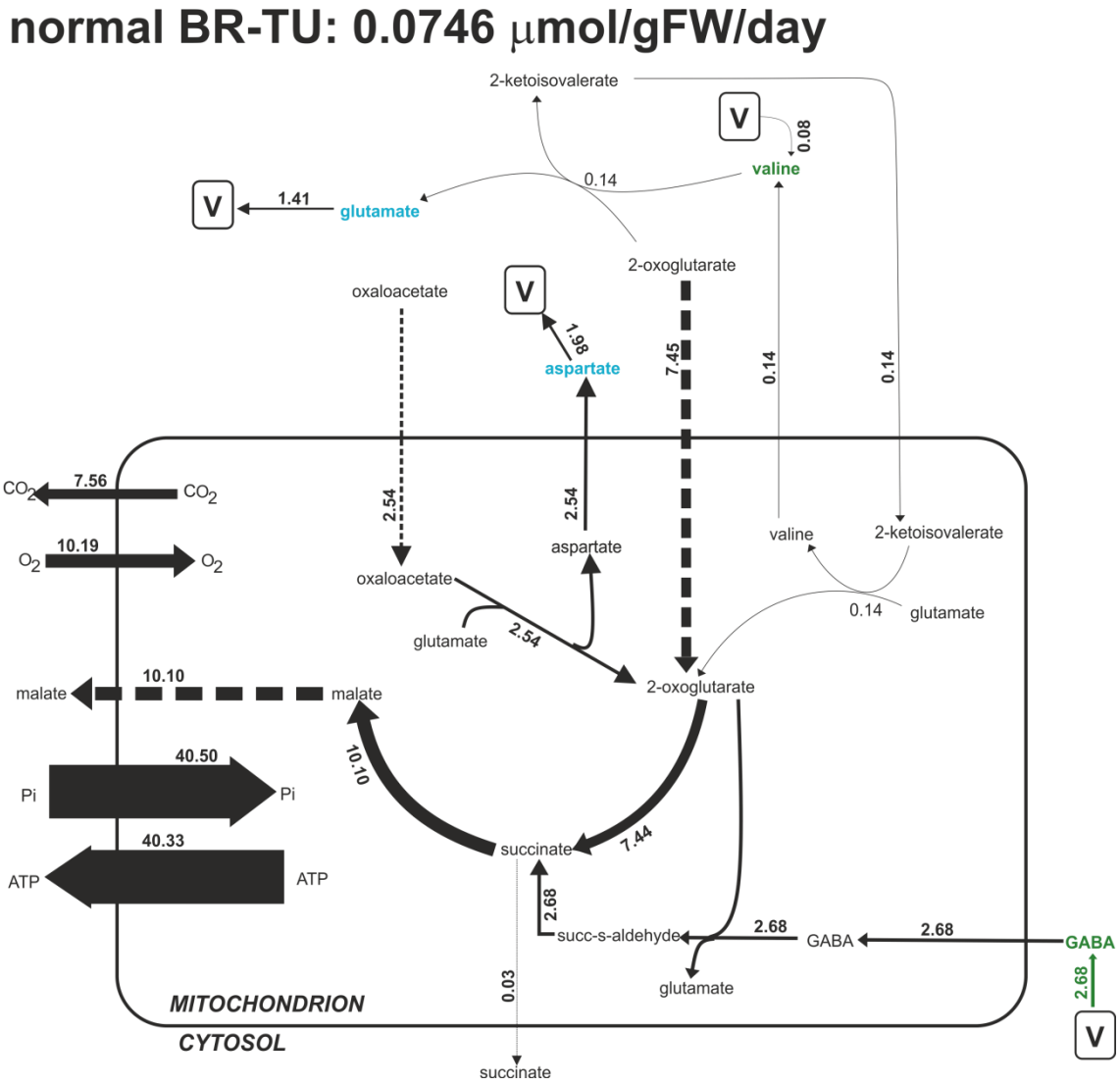

Figure 5.5. Mitochondrial fluxes that changed at flux distribution A relative to normal BR-TU. Both normal BR-TU and flux distribution A accumulate lycopene at 0.0746 mmol/gFW/day but flux distribution A led to a lower sum of fluxes. Relevant mitochondrial fluxes are shown. The thickness of the arrows is scaled to the flux magnitude. Inputs and outputs of the model are colour coded as green and blue

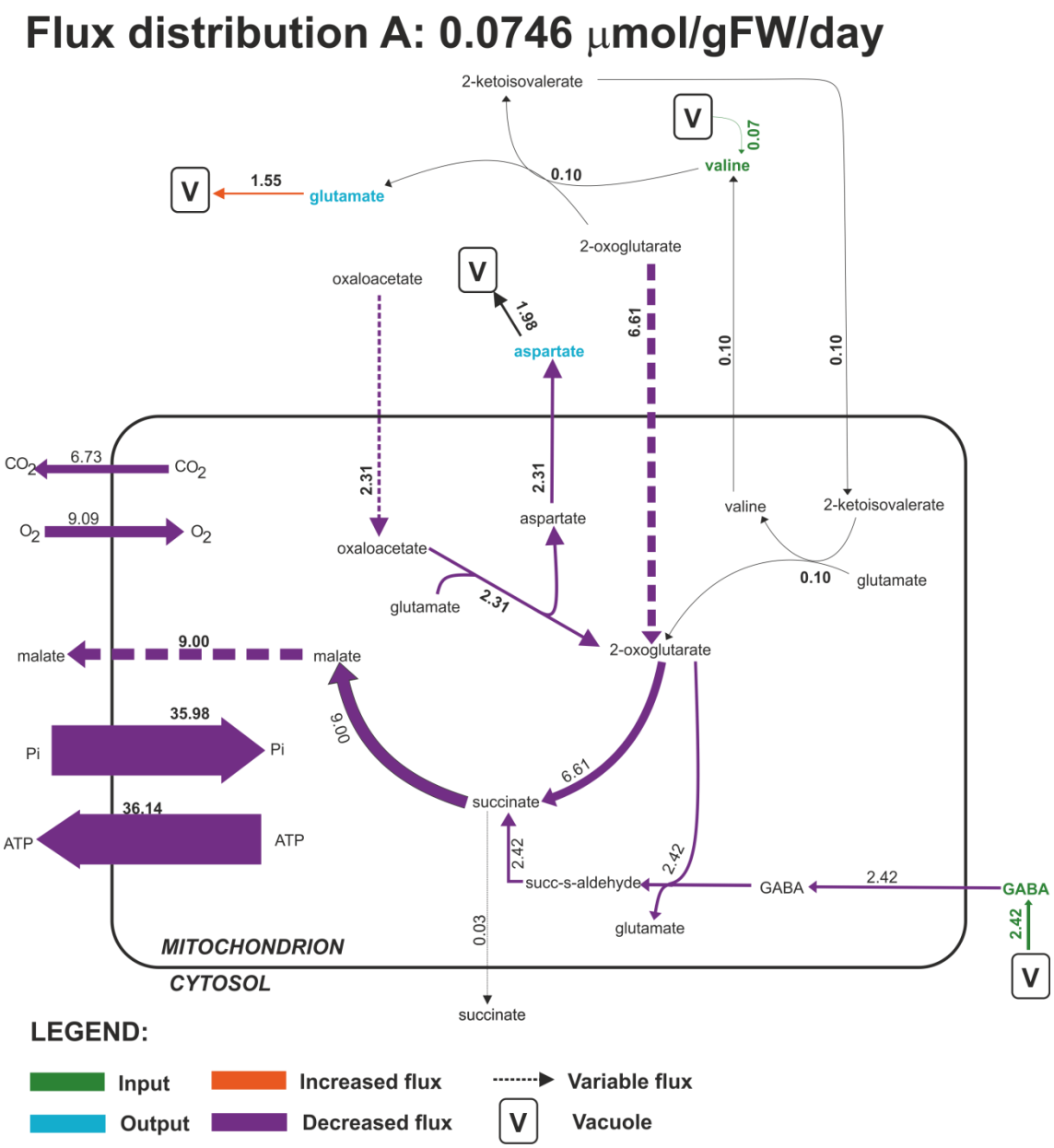

respectively while increased and decreased fluxes at flux distribution A are colour coded as orange and purple respectively. The reactions that are identified as variable through FVA are represented as dashed lines. Small vacuoles are used for clarity and do not represent separate organelles.

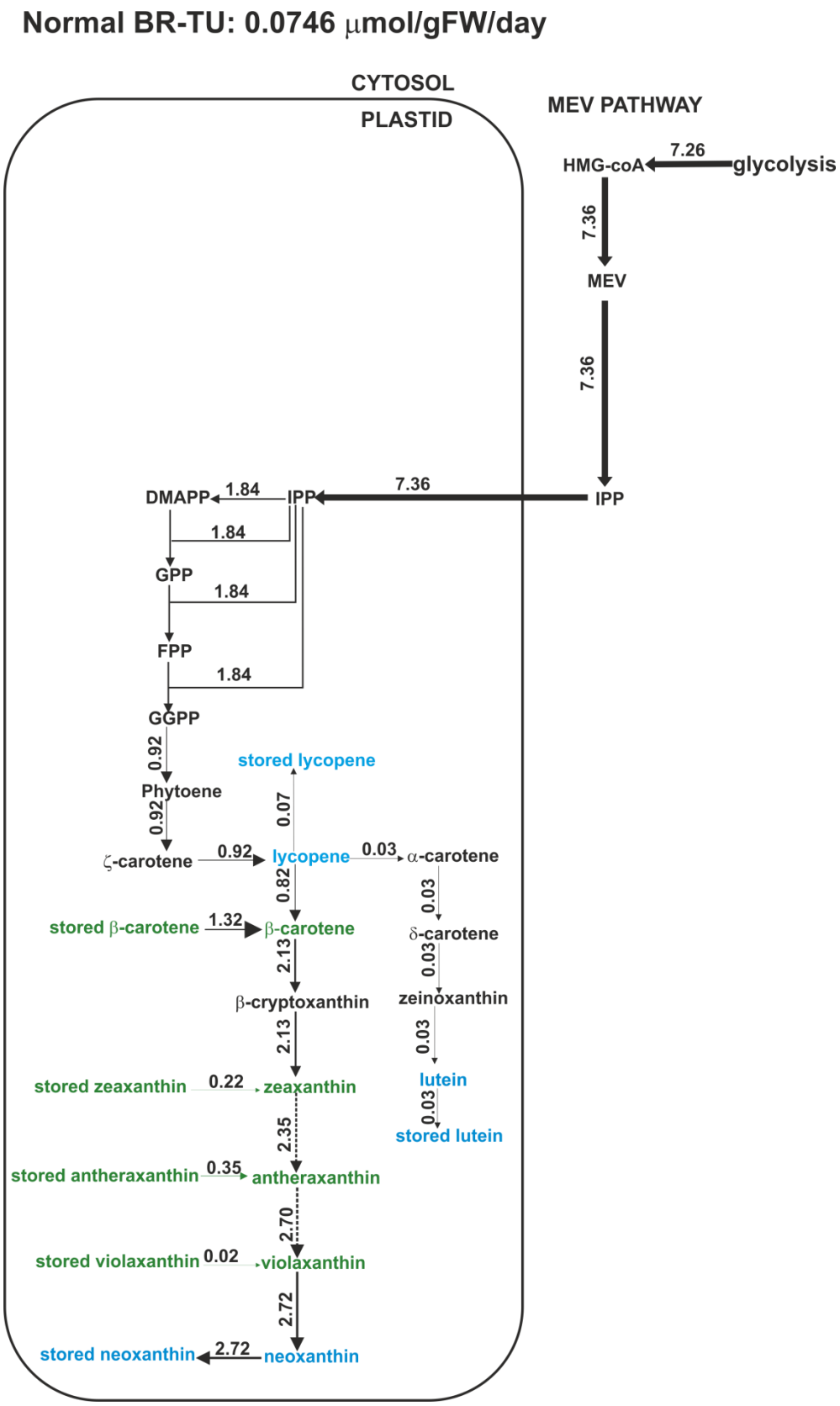

Figure 5.6. The changes in the secondary metabolite synthesis pathway in flux distribution A when compared to normal BR-TU. Only the MEV pathway carried flux in these two flux distributions. The thickness of the arrows has been scaled to the flux

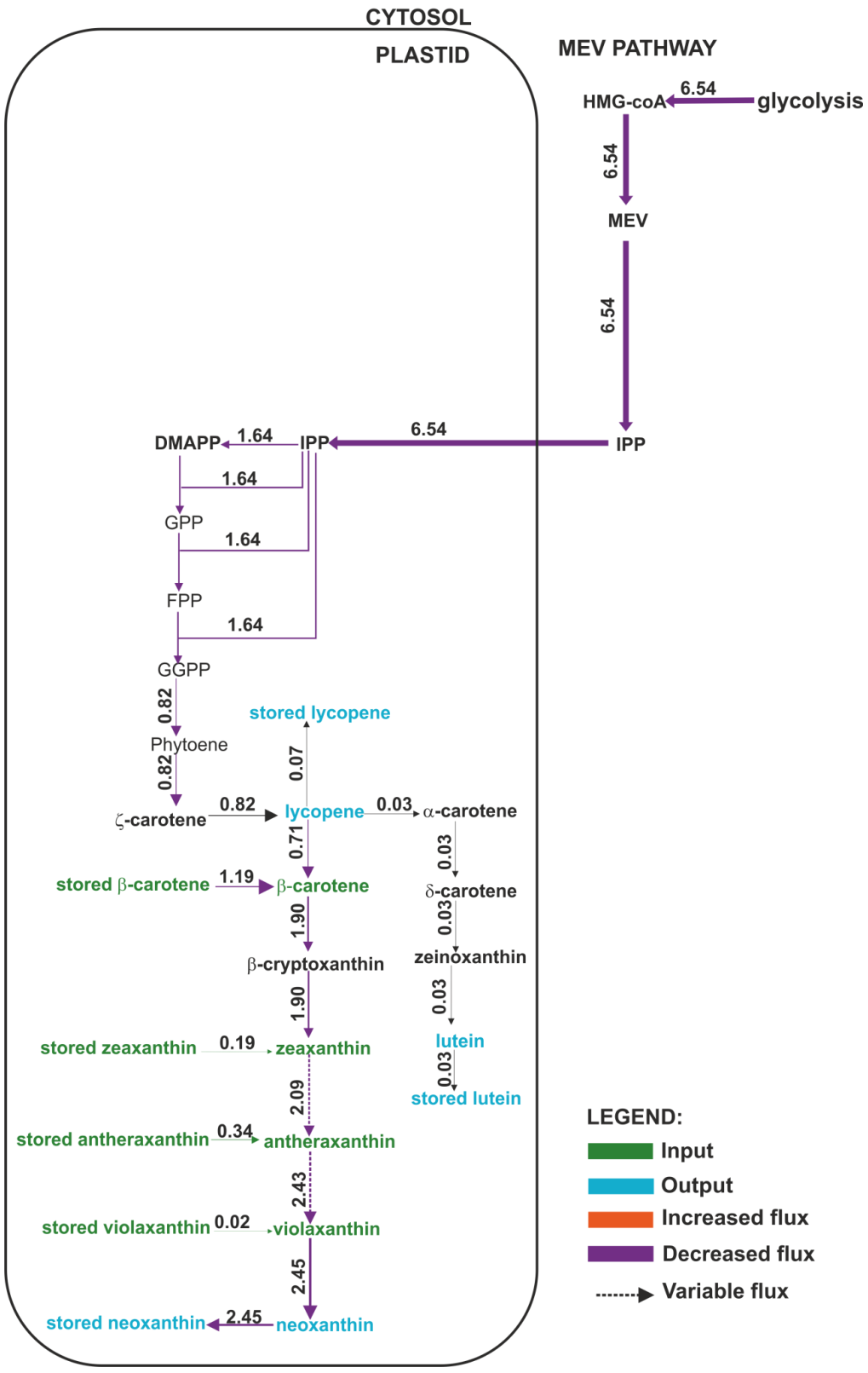

magnitude. Abbreviations: MEV (mevalonate); HMG-coA (hydroxymethylglutaryl-coA); IPP (isopentenyl diphosphate); DMAPP (dimethylallyl diphosphate); GPP (geranyl diphosphate); FPP (farnesyl diphosphate); GGPP (geranylgeranyl diphosphate).

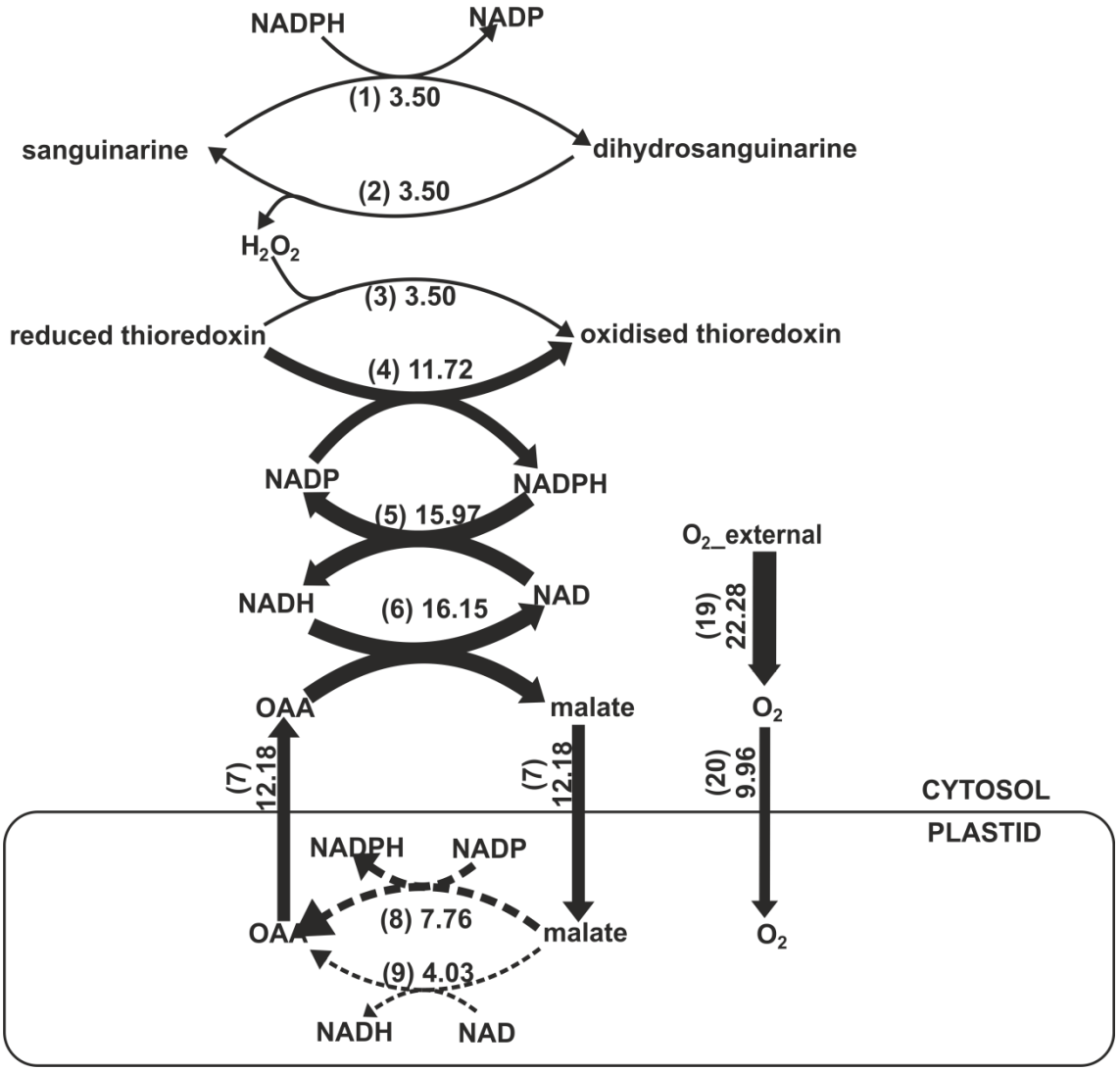

Figure 5.7. Reactions that changed at flux distribution A relative to normal BR-TU. The reduced fluxes in flux distribution A were also of those involved in the synthesis of co-factors and reductants as presented above. The thickness of the arrows has been scaled to the flux magnitude. Bracketed numbers represent reactions as follows: (1) NADP-dependent sanguinarine reductase; (2) dihydrobenzophenanthridine oxidase; (3) thioredoxin peroxidase; (4) NADPH-dependent thioredoxin reductase; (5) NAD(P) transhydrogenase; (6) cytosolic malate dehydrogenase; (7) OAA- malate plastidic exchanger; (8) plastidic NADP-dependent malate dehydrogenase; (9) plastidic NAD-dependent malate dehydrogenase; (19) external oxygen transporter; (20) plastidic

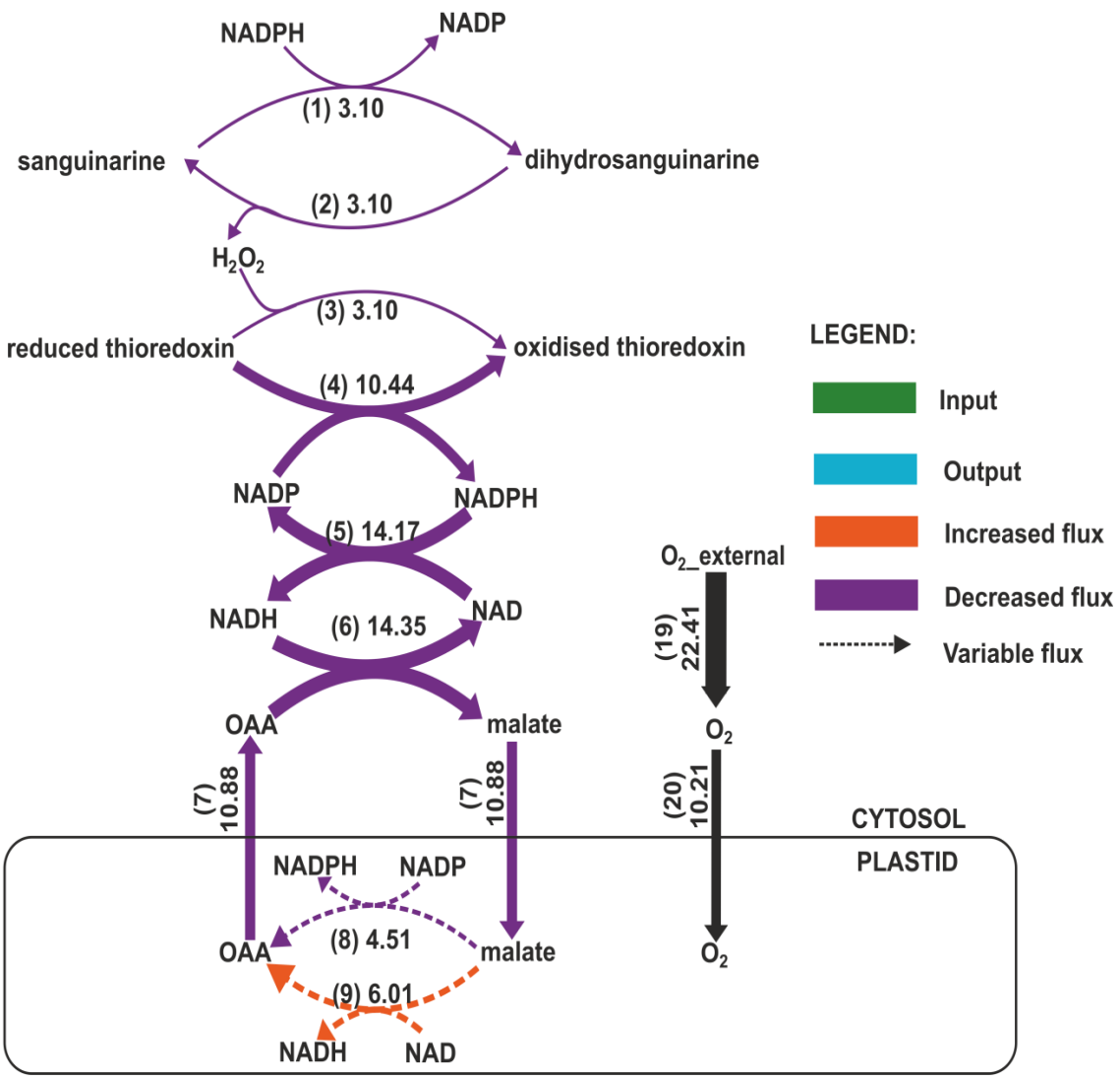

oxygen transporter; and (21) neoxanthin transporter. External oxygen transporter is a transporter that supplies oxygen to the cytosol and is labelled external for modelling purposes. This figure does not represent the whole network and is not carbon balanced. It only illustrates a total of 11 reactions that changed in fluxes at flux distribution A relative to 'normal' BR-TU. Two reactions ((8) and (9)) were identified to be variable at both flux distributions as shown with dashed lines above.

Point A: 0.0746 μmol/gFW/day

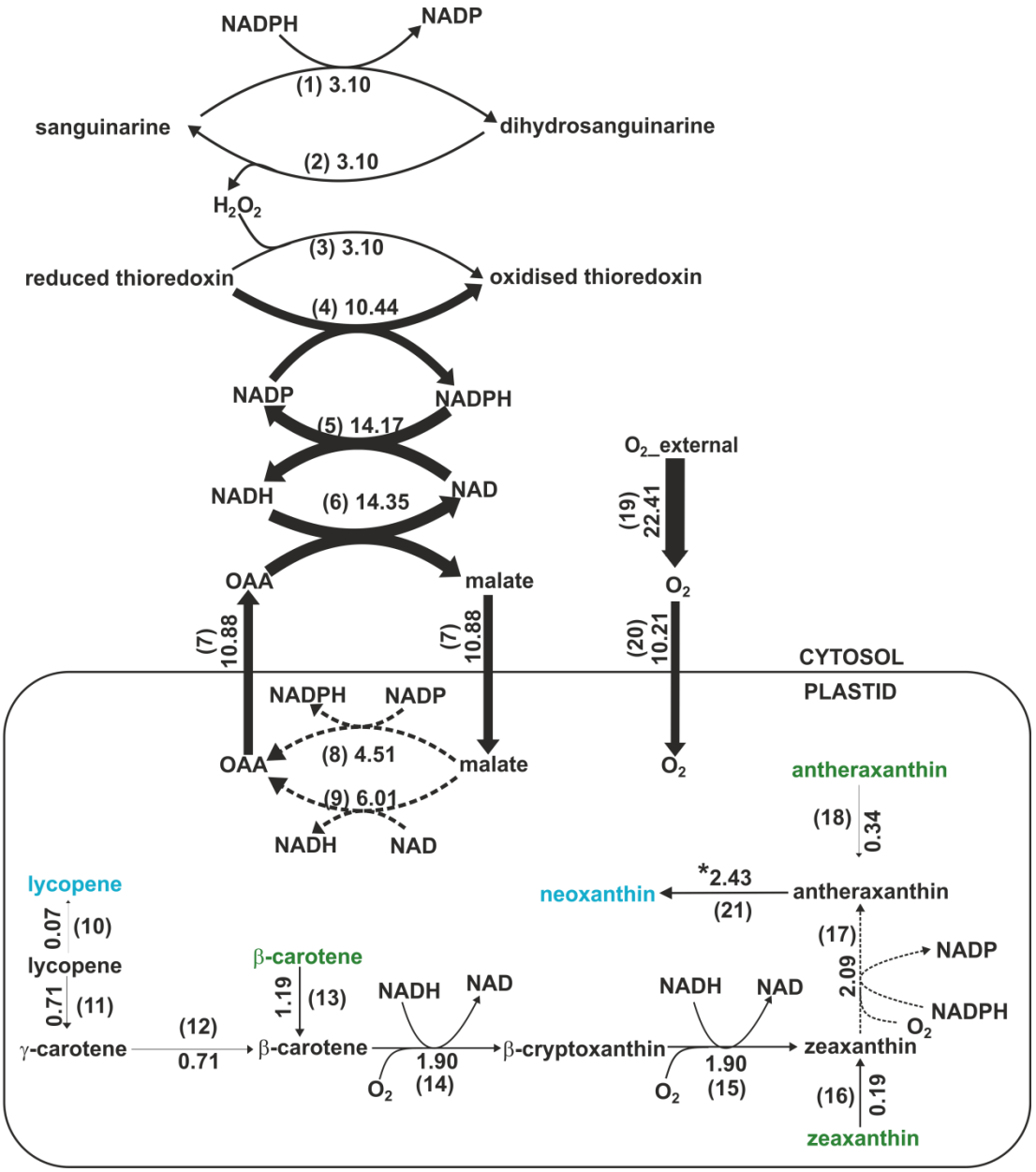

Figure 5.8. Fluxes that changed at flux distribution B relative to flux distribution A. This figure shows the reactions that had their fluxes either increased or decreased when lycopene accumulation have increased 5-fold. Flux values on the arrows are in units of μmol/gFW/day and the thickness of these arrows has been scaled to flux magnitude. Bracketed numbers represent reactions as follows: (1) NADP-dependent sanguinarine reductase; (2) dihydrobenzophenanthridine oxidase; (3) thioredoxin peroxidase; (4) NADPH-dependent thioredoxin reductase; (5) NAD(P) transhydrogenase; (6) cytosolic malate dehydrogenase; (7) OAA- malate plastidic exchanger; (8) plastidic NADP-dependent malate dehydrogenase; (9) plastidic NAD-dependent malate dehydrogenase; (10) lycopene transporter; (11) lycopene β-cyclase; (12) lycopene β-cyclase; (13) β-carotene transporter; (14) β-carotene hydroxylase; (15) β-cryptoxanthin hydroxylase; (16) zeaxanthin transporter; (17)

Flux distribution B: 0.3801 μmol/gFW/day

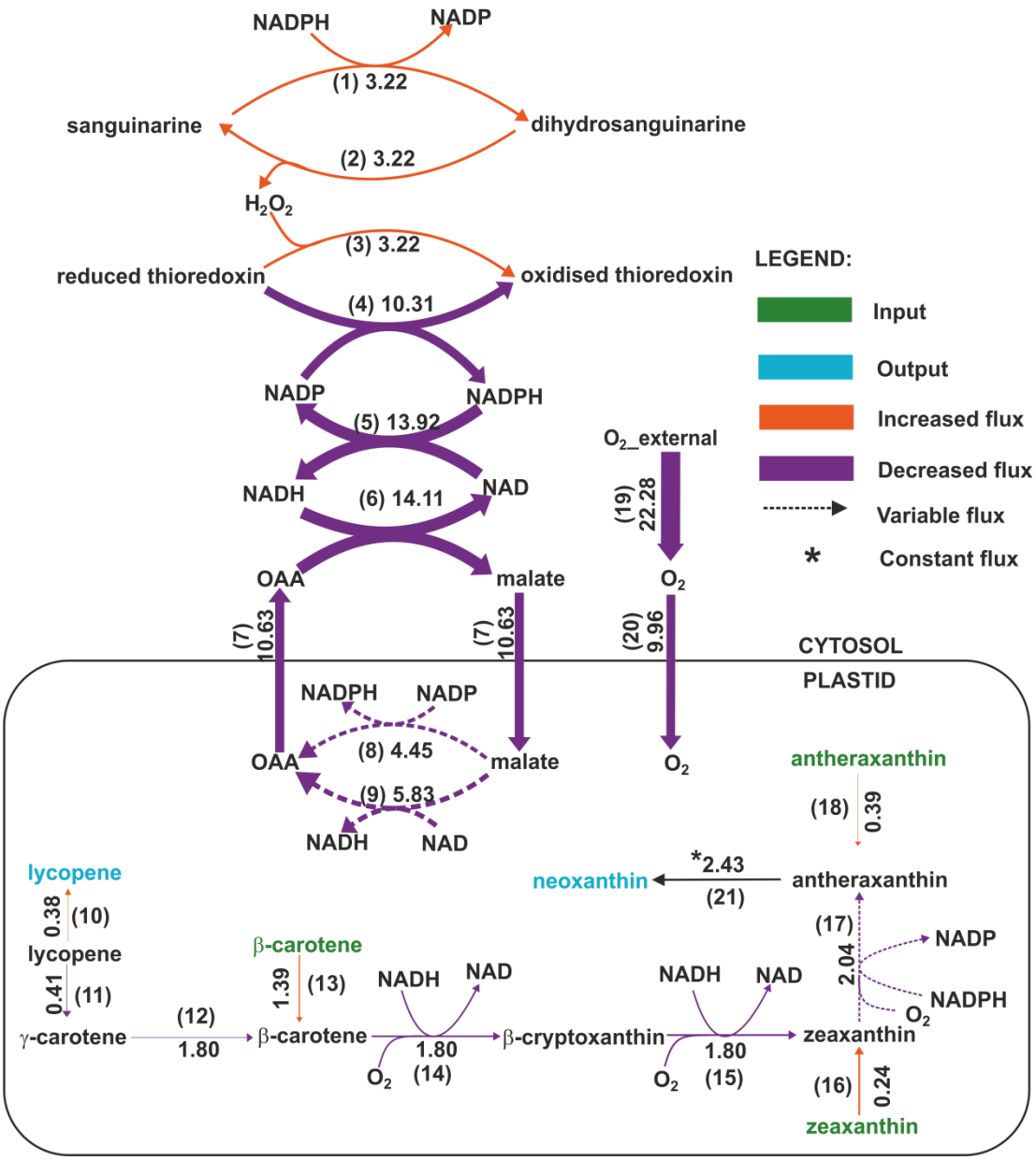

NADPH-dependent zeaxanthin epoxidase; (18) antheraxanthin transporter; (19) external oxygen transporter; (20) plastidic oxygen transporter; and (21) neoxanthin transporter. External oxygen transporter is a transporter that supplies oxygen to the cytosol and is labelled external for modelling purposes. This figure does not represent the whole network and is not carbon balanced. It only illustrates a total of 20 reactions that changed in fluxes at flux distribution B relative to flux distribution A and one constant reaction which accumulated neoxanthin (reaction (21)). Three reactions ((8), (9) and (17)) were identified to be variable at both flux distributions as shown with dashed lines above. Both plastidic malate dehydrogenases (reactions (8) and (9)) were essential whereas NADPH-dependent zeaxanthin epoxidase (reaction (17)) was substitutable with a NAD-dependent zeaxanthin epoxidase.

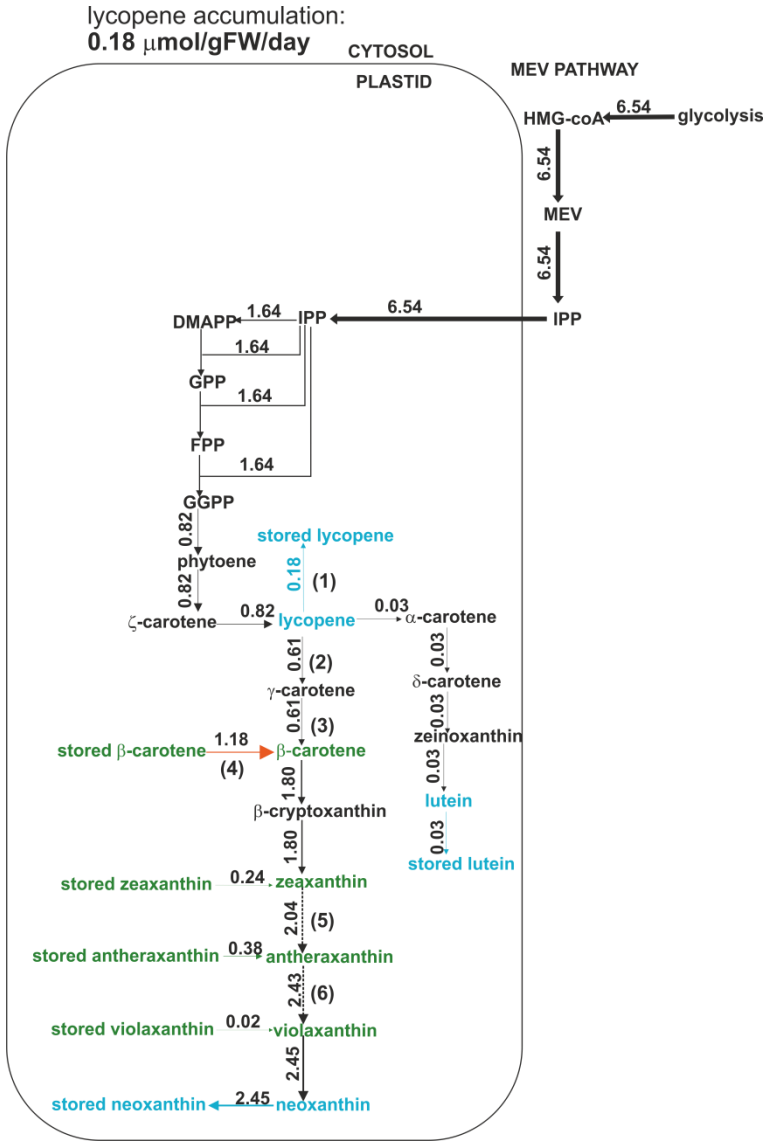
lycopene accumulation:
0.18 μmol/gFW/day
CYTOSOL
PLASTID
MEV PATHWAY
HMG-coA
6.54
glycolysis
6.54
MEV
6.54
IPP
DMAPP
1.64
IPP
6.54
1.64
GPP
1.64
FPP
1.64
GGPP
0.82
stored lycopene
phytoene
0.18
(1)
0.82
ζ-carotene
0.82
lycopene
0.03
α-carotene
0.03
δ-carotene
0.61
(2)
γ-carotene
0.61
0.03
zeinoxanthin
(3)
stored β-carotene
1.18
β-carotene
(4)
0.03
lutein
1.80
β-cryptoxanthin
1.80
0.03
stored lutein
stored zeaxanthin
0.24
zeaxanthin
2.04
(5)
stored antheraxanthin
0.38
antheraxanthin
2.43
(6)
stored violaxanthin
0.02
violaxanthin
2.45
stored neoxanthin
2.45
neoxanthin

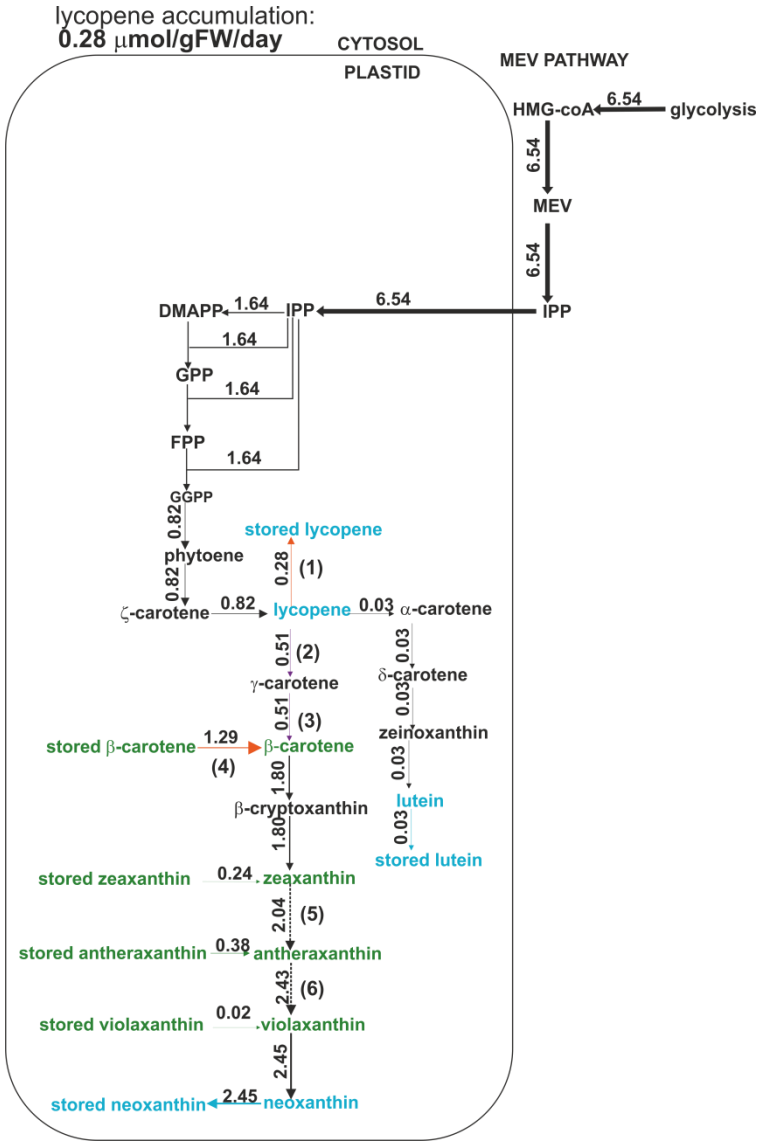
lycopene accumulation:
0.28 μmol/gFW/day
CYTOSOL
PLASTID
MEV PATHWAY
HMG-coA
6.54
glycolysis
6.54
MEV
6.54
IPP
DMAPP
1.64
IPP
6.54
1.64
GPP
1.64
FPP
1.64
GGPP
0.82
stored lycopene
phytoene
0.28
(1)
0.82
ζ-carotene
0.82
lycopene
0.03
α-carotene
0.03
δ-carotene
0.51
(2)
γ-carotene
0.51
0.03
zeinoxanthin
(3)
stored β-carotene
1.29
β-carotene
(4)
0.03
lutein
1.80
β-cryptoxanthin
1.80
0.03
stored lutein
stored zeaxanthin
0.24
zeaxanthin
2.04
(5)
stored antheraxanthin
0.38
antheraxanthin
2.43
(6)
stored violaxanthin
0.02
violaxanthin
2.45
stored neoxanthin
2.45
neoxanthin

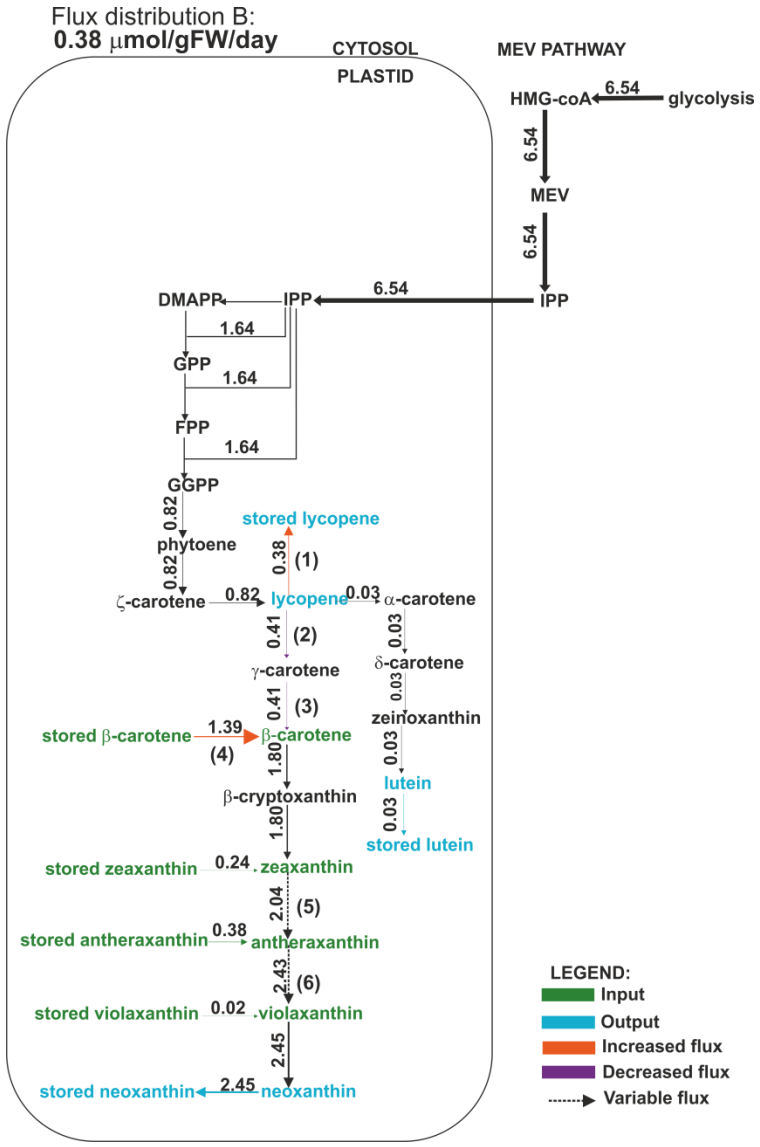

Figure 5.9. Three flux distributions with constant objective values. The thickness of the arrows has been scaled to the flux magnitude. Bracketed number represent reactions as follows: (1) lycopene transporter; (2) γ-carotene-forming lycopene β-cyclase; (3) β-carotene-forming lycopene β-cyclase; (4) β-carotene transporter; (5) antheraxanthin-forming zeaxanthin epoxidase (NADP dependent); and (6) violaxanthin-forming zeaxanthin epoxidase (NAD dependent). Only four reactions changed in these flux distributions and they are marked with bracketed numbers (1) to (4). Reactions (1) and (4) increases while reactions (2) and (3) decreases in these three flux distributions. FVA was carried out on these flux distributions and reactions (5) and (6) were identified as substitutable. They can be substituted with a NAD- and NADP dependent zexanthin epoxidases respectively. Abbreviations: MEV (mevalonate); HMG-coA (hydroxymethylglutaryl-coA); IPP (isopentenyl diphosphate); DMAPP (dimethylallyl diphosphate); GPP (geranyl diphosphate); GGPP (geranylgeranyl diphosphate).

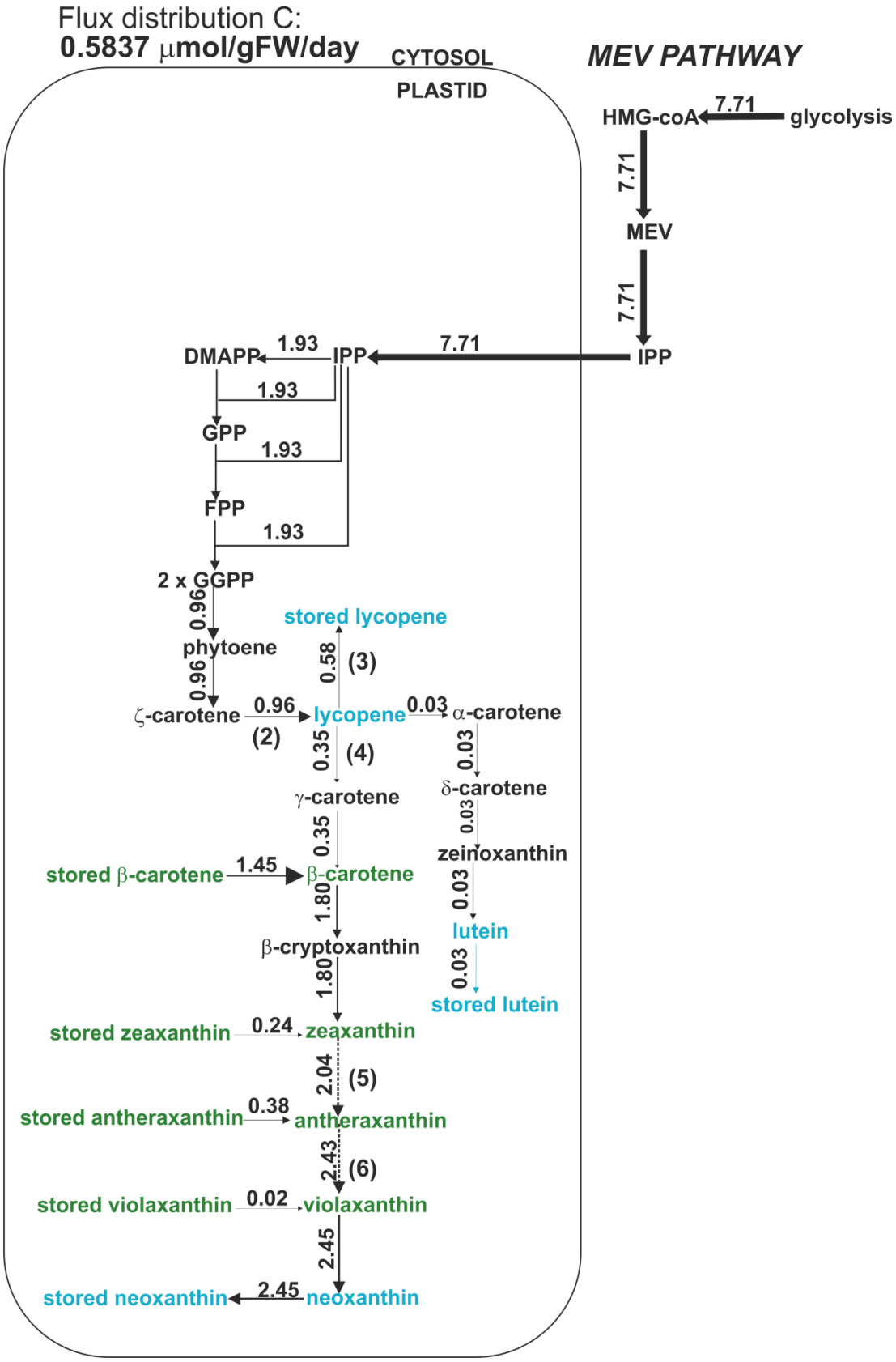

Figure 5.10. MEP pathway activates in flux distribution D. The thickness of the arrows has been scaled to the flux magnitude. The bracketed numbers represent reactions as follows: (1) HMBPP reductase; (2) ζ-carotene desaturase ; (3) lycopene transporter; (4) lycopene β-cyclase; (5) antheraxanthin-forming zeaxanthin epoxidase

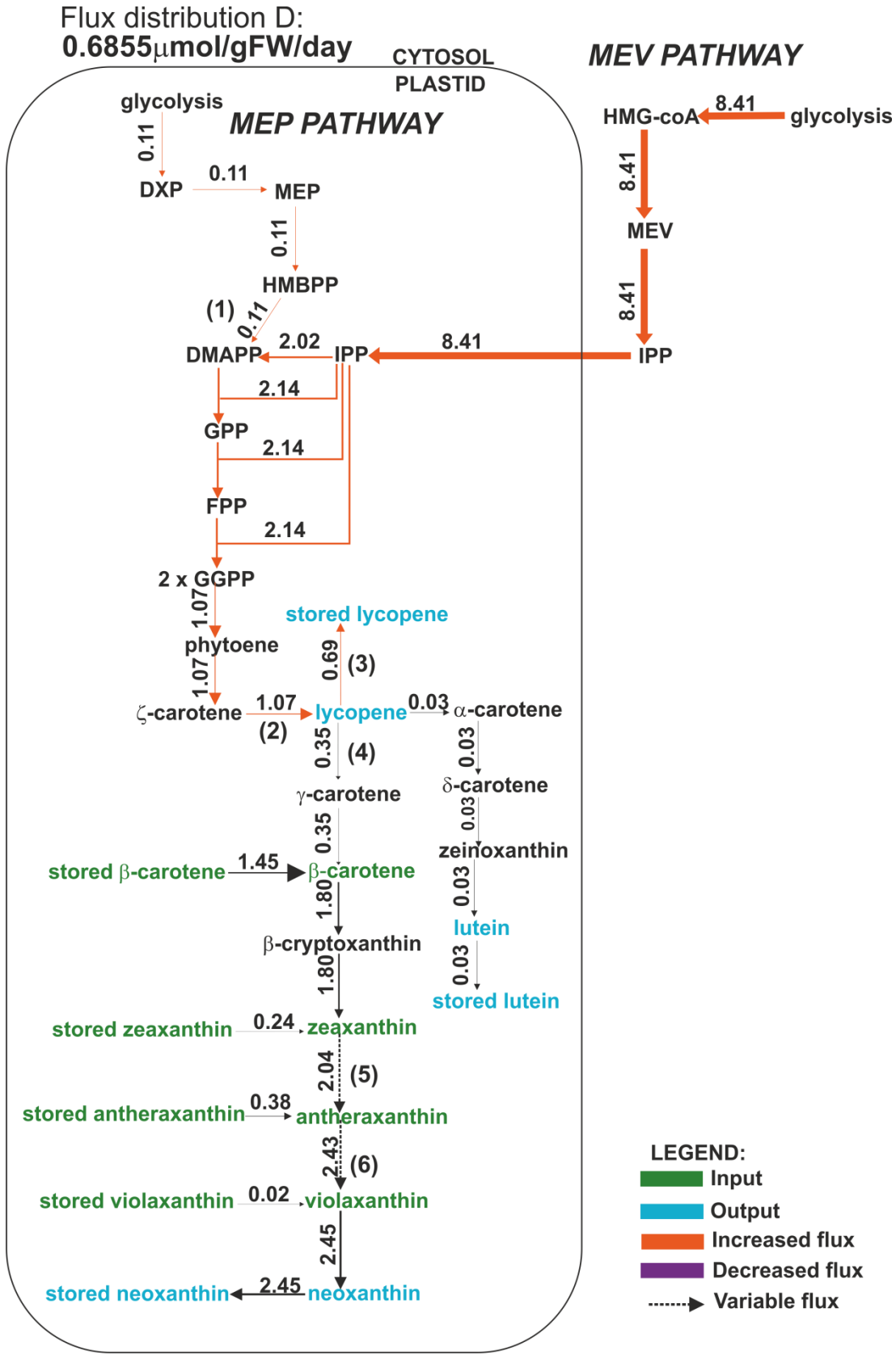

(NADP dependent); and (6) violaxanthin-forming zeaxanthin epoxidase (NAD dependent). Reactions (5) and (6) were identified to be variable reactions through FVA. Abbreviations: MEV (mevalonate); HMG-coA (hydroxymethylglutaryl-coA); IPP (isopentenyl diphosphate); DMAPP (dimethylallyl diphosphate); GPP (geranyl diphosphate); GGPP (geranylgeranyl diphosphate).

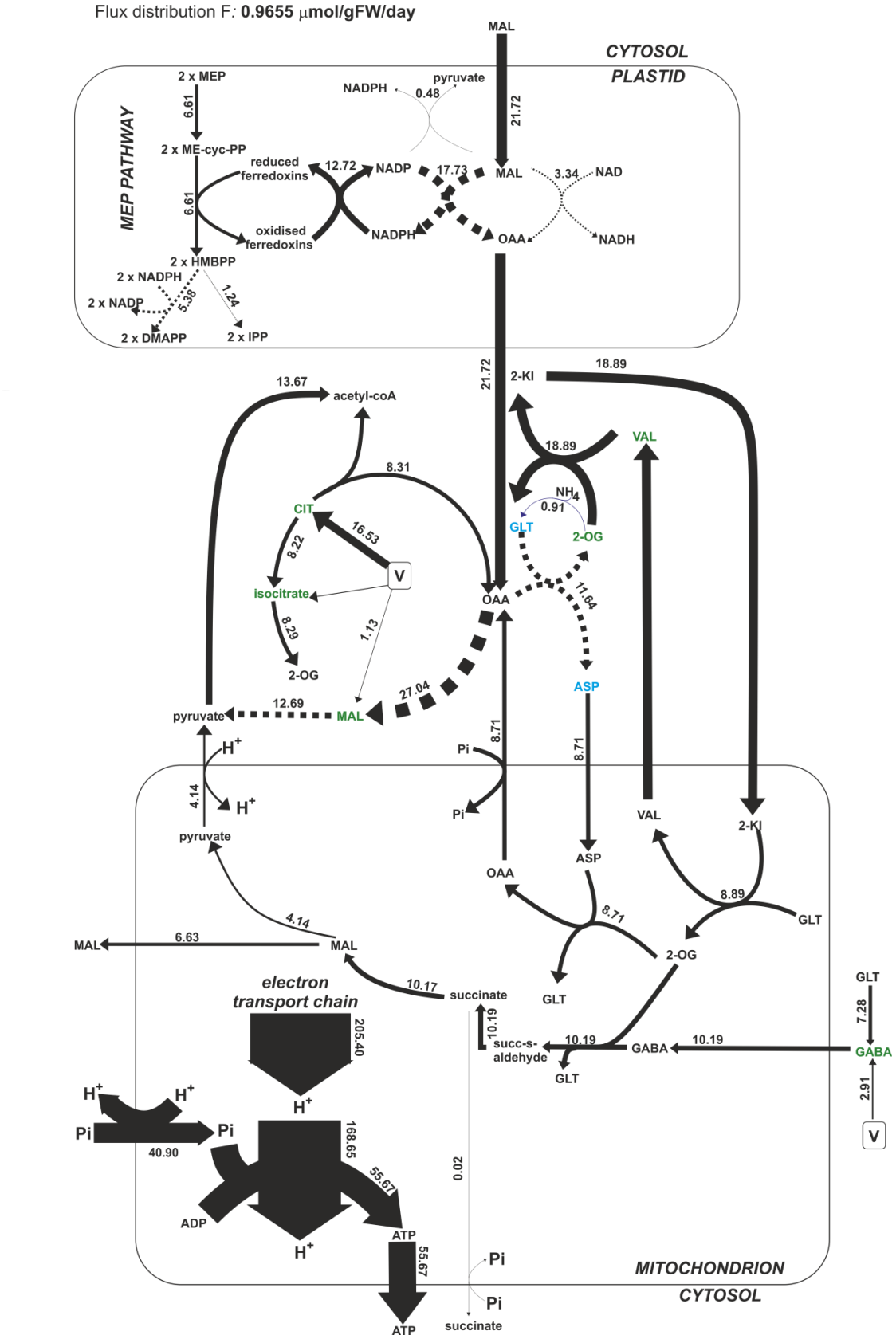

Figure 5.11. Predominant fluxes when lycopene accumulation increased 13-fold. The thickness of the arrows has been scaled to the flux magnitude. Abbreviations: MEP (methylerythritol phosphate); ME-cyc-PP (methylerythritol cyclodiphosphate); HMBPP (hydroxymethyl butenyl diphosphate); IPP (isopentenyl

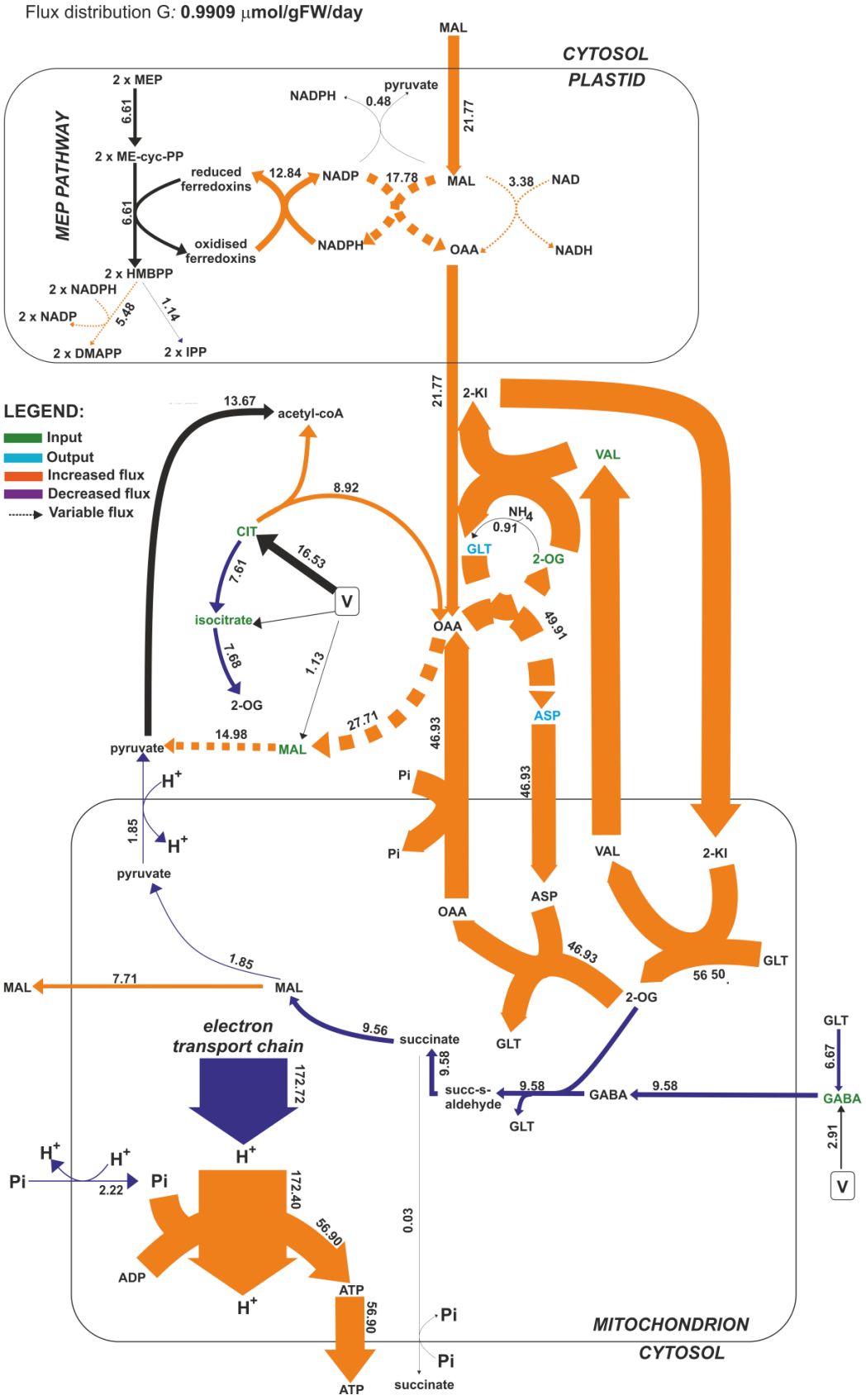

diphosphate); DMAPP (dimethylallyl diphosphate); MAL (malate); OAA (oaxaloacetate); 2-KI (2-ketoisovalerate); 2-OG (2-oxoglutarate); CIT (citrate); GLT (glutamate); ASP (aspartate); VAL (valine); GABA (γ-aminobutyrate).

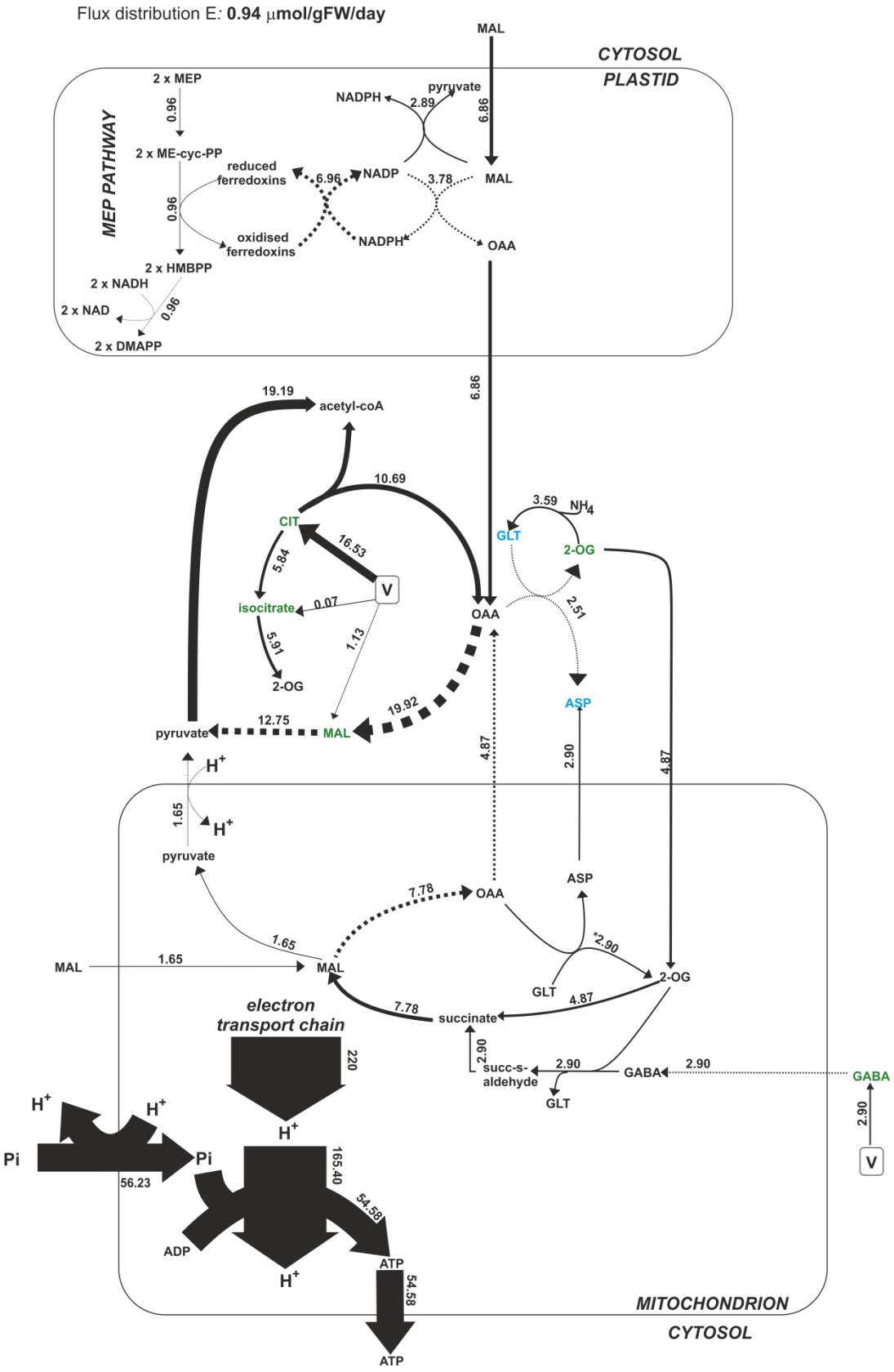

Figure 5.12. Predominant fluxes when lycopene accumulation increased 12.6-fold. The sum of fluxes begins to increase markedly at flux distribution F and the relevant fluxes that have changed is shown. The thickness of the arrows has been scaled to the flux magnitude. Abbreviations: MEP (methylerythritol phosphate); ME-

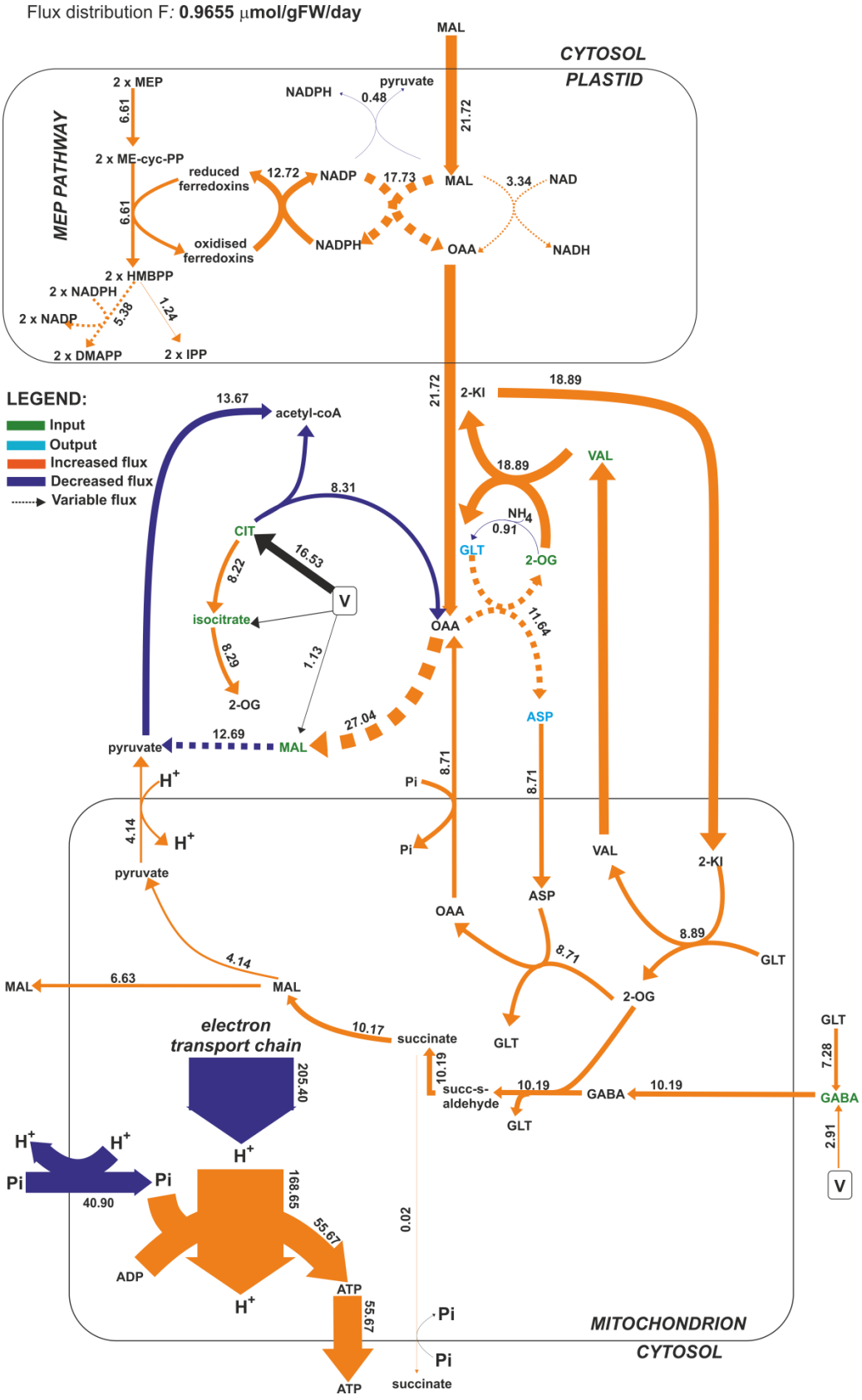

cyc-PP (methylerythritol cyclodiphosphate); HMBPP (hydroxymethyl butenyl diphosphate); IPP (isopentenyl diphosphate); DMAPP (dimethylallyl diphosphate); MAL (malate); OAA (oaxaloacetate); 2-KI (2-ketoisovalerate); 2-OG (2-oxoglutarate); CIT (citrate); GLT (glutamate); ASP (aspartate); VAL (valine).

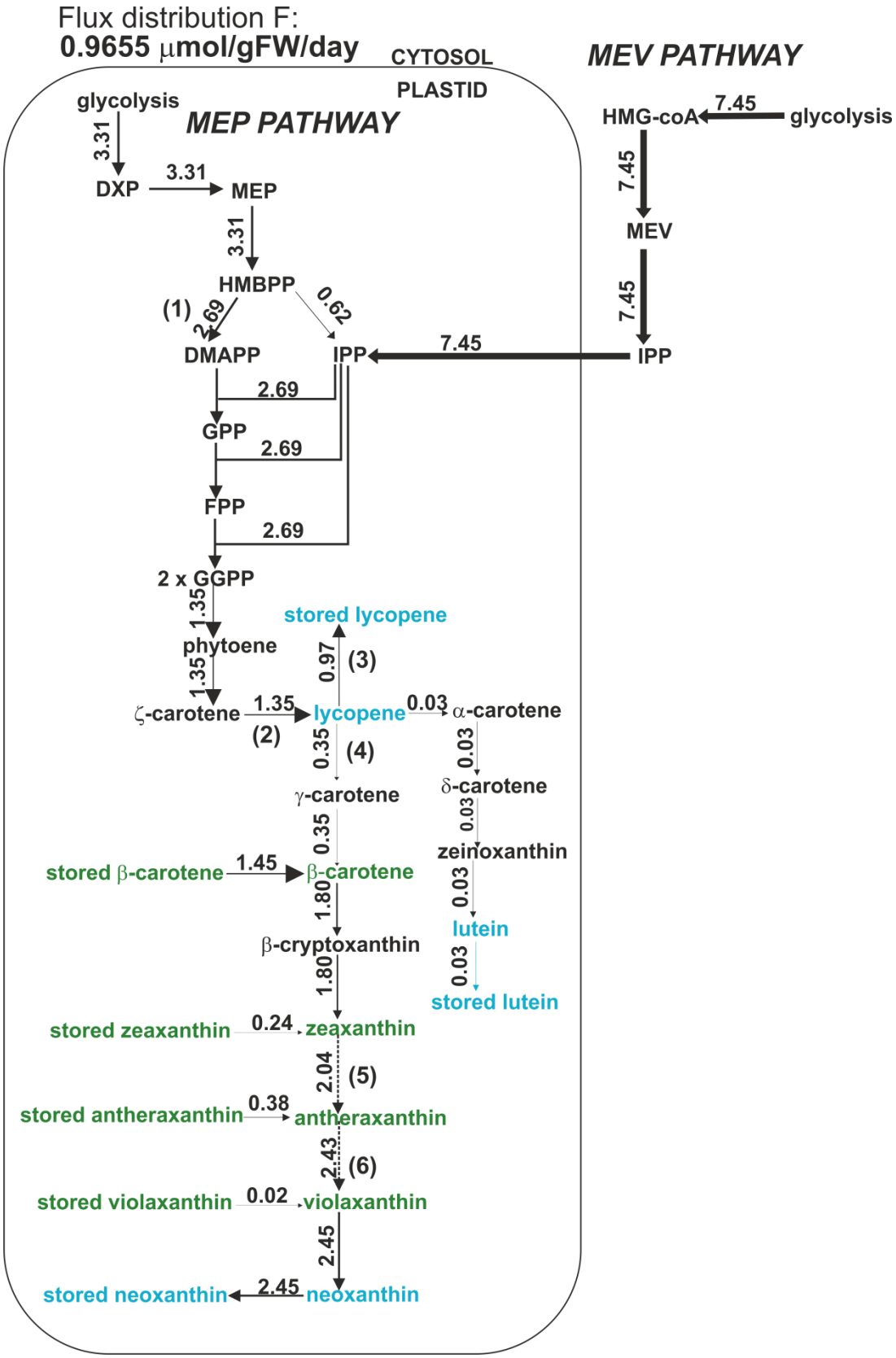

Figure 5.13. The change in the secondary metabolite synthesis pathway fluxes in flux distribution F and G. The MEV pathway increased to supply more precursors towards lycopene accumulation. The thickness of the arrows has been scaled to the flux magnitude. Abbreviations: MEV (mevalonate); MEP (methylerythritol phosphate); DXP (deoxyxylulose-5-phosphate);

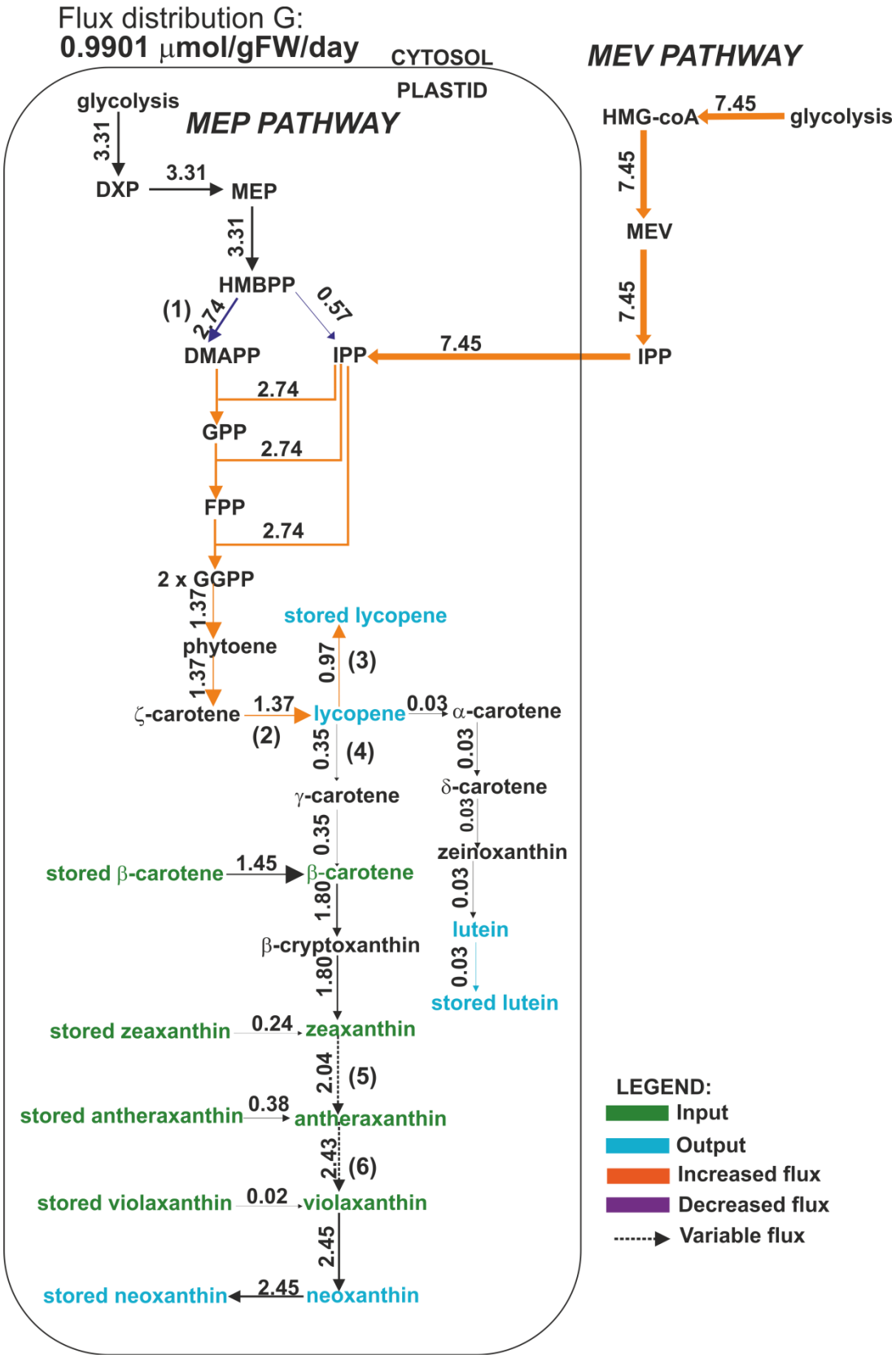

HMBPP (hydroxymethylbutenyl diphosphate); IPP (isopentenyl diphosphate); DMAPP (dimethylallyl diphosphate); GPP (geranyl diphosphate); FPP (farnesyl diphosphate); GGPP (geranylgeranyl diphosphate).

5.3 Discussion

5.3.1 Allowing constraints to vary within a 10% range introduced more flexibility to the metabolic network

Lycopene accumulation increased 13.2-fold

The results of the lycopene scan show that the highest lycopene accumulation rate possible was 0.9909 μmol/gFW/day and no feasible flux distribution could be found for a greater lycopene accumulation rate (Figure 5.1). This 13.2-fold increase limit was likely determined by the input and output constraints on the network. Confirming this, another lycopene scan using a 50% range for the constraints was carried out. The highest lycopene accumulation rate predicted was 1.308 μmol/gFW/day, a 17.5-fold increase than the normal level.

5.3.2 Lycopene accumulation increased at the cost of reduced β-carotene production

The fluxes towards the production of β-carotene were shown to reduce 2-fold as lycopene accumulation was increased in the scan. This is because more fluxes were routed towards the storage of lycopene than towards the production of other carotenoids, as evident in Figure 5.9. There are two types of lycopene cyclase in the plastidic carotenoids synthesis pathway: a) lycopene β-cyclase which produces β-carotene and xanthophylls; and b) lycopene ε-cyclase which produces α-carotene and lutein (Cunningham et al., 1996; Ronen et al., 1999). In the lycopene scan, fluxes of lycopene β-cyclase were shown to reduce

whereas the fluxes of lycopene ε-cyclase did not change with increasing lycopene accumulation (Figures 5.6, 5.9 and 5.10). These findings seem to be consistent with other research that found that the accumulation of lycopene was at the expense of reduced β-carotene synthesis (Fraser et al., 1994; Ronen et al., 1999). One study, in which the *CrtL-e* gene encoding lycopene ε-cyclase from tomato was cloned, found that the down-regulation of both lycopene cyclases played an important role in lycopene accumulation during tomato fruit ripening (Ronen et al., 1999). Furthermore, in another study on ripening tomato fruit, it was found that a significantly higher amount of lycopene was found in relation to β-carotene (Fraser et al., 1994).

Reducing the fluxes of one or more reactions in order to reroute more carbon towards the synthesis of a target metabolite has been shown in a number of metabolic engineering studies. For example, FBA modelling of *E. coli* using the OptForce procedure suggested that the TCA cycle flux was reduced in order to improve the production of naringenin (Xu et al., 2011). Accordingly, succinyl CoA synthethase was eliminated to reroute acetyl-coA towards the production of malonyl-coA, the precursor for naringenin, rather than towards the synthesis of TCA cycle intermediates. This gene deletion, in cooperation with other genetic changes identified through the OptForce procedure, successfully improved the production of naringenin by 560% (Xu et al., 2011). Similarly, another FBA analysis employing a minimization of metabolic adjustment (MOMA) algorithm in a genome-scale model of *E.coli* suggested that deletion of malate dehydrogenase, pyruvate dehydrogenase and phosphofructokinase would lead to increased production of L-valine (Park et al., 2007). These

deletions significantly increased the pyruvate pool by rerouting carbon away from the TCA cycle and increasing the availability of NADPH by pushing more carbon into the pentose phosphate pathway. The triple knockout strain successfully improved the production of L-valine by 45.5% (Park et al., 2007).

5.3.3 Lycopene accumulation can be improved by increasing the supply for precursors and reductants

The results in this study indicate that the precursor pool needs to be increased to promote lycopene accumulation. This is evident when lycopene accumulation increased 9.2-fold and the MEP pathway was required to operate alongside the MEV pathway to increase the DMAPP pool (Figure 5.10). Furthermore, as lycopene accumulation increased 12.9-fold, the MEP pathway also supplied IPP in addition to DMAPP (Figure 5.13). These results are consistent with those of secondary metabolite engineering studies in *E.coli* (Martin et al., 2003; Pitera et al., 2007; Yoon et al., 2006) and *Synechosystis sp.* PCC 6803 (Bentley et al., 2014), which found that the production of the target metabolite improved by increasing the flux towards the synthesis of DMAPP and IPP. This was done by bypassing the native MEP pathway by routing metabolic fluxes through the MEV pathway, which was heterologously incorporated. In these transformants, it was shown that accumulation of terpenoids such as isoperene (Bentley et al., 2014; Zurbriggen et al., 2012), amorphadiene (Martin et al., 2003; Pitera et al., 2007) and lycopene (Vadali et al., 2005; Yoon et al., 2006) increased between 2- to 800-fold.

However, in a broader perspective, reactions in a metabolic pathway are interconnected (Sweetlove & Fernie, 2005) and the increase of fluxes in one pathway leads to the decrease or increase of fluxes in another pathway. Thus, increasing fluxes towards precursor biosynthesis goes beyond just increasing fluxes of the MEP and MEV pathway. This observation was shown in my model when lycopene accumulation increased 13-fold (Figure 5.11). In order to push fluxes into the MEP pathway to supply IPP and DMAPP and increase the required reductants, TCA cycle fluxes were reduced and cytosolic reaction fluxes were increased (Figure 5.11). One possible explanation for this finding is that the production of 2-OG was routed towards the cytosolic reactions rather than towards the synthesis of TCA cycle intermediates. This is because 2-OG was predicted to be consumed and produced by a chain of aminotransferase reactions in flux distributions F and G. This increased the availability of cytosolic OAA and malate, which pushed fluxes into the MEV and plastidic MEP pathway. Another possible explanation for the reduced TCA cycle fluxes when lycopene accumulation increased 13-fold is to reduce the demand for mitochondrial reductants to generate more ATP and cytosolic intermediates. As is shown in Figure 5.12, although fluxes between succinate and malate increased, the reactions between 2-OG and succinate did not carry any flux in flux distribution F when compared to flux distribution E. This reduces the supply of NADH for the ETC, which was also reduced. This was due to increased fluxes in the cytosolic aminotransferase chain that increased the intake of Pi into the mitochondria in exchange for OAA, which reduces the fluxes to import Pi in exchange of H^+. This consequently reduced the demand for H^+ to be

pumped across the mitochondrial membrane and thus reduced the cost to run the ETC (Figure 5.12).

The need to increase the supply of precursors and reductants was also shown to improve the production of non-secondary products in other studies. In *E. coli,* the production of naringenin (Xu et al., 2011) and phlogucinol (Zha et al., 2009) improved markedly by increasing the availability of the malonyl-CoA as the precursor. In *Corynebacterium glutamicum,* the overproduction of L-lysine was achieved by increasing the availability of reductants (Becker et al., 2011). It was shown in these studies that a reduction in TCA cycle fluxes was required to reroute carbon fluxes towards the synthesis of precursor malonyl CoA (Xu et al., 2011; Zha et al., 2009) and an increase in pentose phosphate pathway activity was required to increase reductant availability (Becker et al., 2011).

5.4 Summary

This chapter has given an account of the reasons for the underlying metabolic changes that occurred when lycopene accumulation is increased in a ripening tomato fruit. This study has shown that in order to improve the production of lycopene, the metabolic fluxes needs to be changed towards increasing the availability of reductants and precursors. This includes increasing the fluxes of the cytosolic reactions and reducing the fluxes of the TCA cycle to increase the availability of important intermediates such as OAA and malate.

Chapter 6: General discussion

6.1 Summary of the work in this thesis

The aim of the work presented in this thesis was to construct a metabolic model of a ripening tomato fruit and use the model to investigate the changes that occurred when the tomato metabolic network is engineered to accumulate high levels of lycopene. Using a semi-automated approach based on the tomato metabolic database LycoCyc 3.0 a genome-scale model was constructed consisting of 2500 reactions and 2366 metabolites. To model two ripening transitions (mature green to breaker stages (MG-BR) and breaker to turning stages (BR-TU)), on-vine ripened tomato metabolite composition data at these stages (Baxter et al., 2005; Carrari et al., 2006; Valle et al., 1998) were converted into degradation and accumulation rates and were used to constrain the model. I found additional influx of sugars and amino acids were required to satisfy the constraints, confirming that the tomato was required to ripen on-vine to reproduce the metabolite composition.

To investigate how network fluxes are remodelled when the network is engineered for increased lycopene production, varying lycopene accumulation rates were imposed onto the model on top of the other input and output constraints of BR-TU. In relation to the other flux distributions with lower lycopene accumulation rates, the flux distribution with the maximum 13.2-fold increase in lycopene accumulation showed dramatic changes, which involved high fluxes through several cytosolic and mitochondrial aminotransferases. This dramatic change in flux distribution was a way for the network to cope with the increased demand for reductants at high lycopene accumulation while still

maintaining the metabolite composition imposed. Increasing lycopene accumulation was achieved in part at the expense of β-carotene accumulation. The results suggested that in order to improve the production of lycopene, the network was required to rearrange in order to meet the reductants and energy demands, which came at a cost of a lower accumulation of other secondary metabolites.

6.2 Unique modelling approaches using FBA

6.2.1 Constraining both inputs and outputs

In this thesis, Flux Balance Analysis (FBA) was chosen as the modelling technique. The technique has been shown to be useful in a number of plants systems such as Arabidopsis (Cheung et al., 2014, 2013; Dal'Molin et al., 2010; Mintz-Oron et al., 2012; Poolman et al., 2009), rice (Poolman et al., 2013), barley seeds (Grafahrend-Belau et al., 2009), maize (Saha et al., 2011) and rapeseeds (Pilalis et al., 2011). However, the way the model was constrained in my work is unique. All other plant models to date have considered the conversion of a small number of inputs (typically a sugar and inorganic nitrogen supply) into the precursors for the bulk biomass polymers (protein, cell wall, lipid and starch). However, my model was concerned with the interconversion of one set of metabolites into another, leading to the decline in some stored metabolites and the accumulation of others during ripening. This represents not only a different set of outputs from the conventional biomass precursors but also the model has a large number of different inputs. Hence my model was constrained from both ends, with individual metabolic degradation and

accumulation rates as inputs and outputs respectively. This created a highly constrained network with a low degree of flexibility for metabolite conversion.

In plants systems, FBA models are constrained by fixing the rates of either the inputs or the outputs or both. Examples of inputs used for these FBA studies include glucose uptake rates (Poolman et al., 2009), sucrose and oxygen uptake rates (Grafahrend-Belau et al., 2009) or photons (Poolman et al., 2013; Saha et al., 2011). Meanwhile, for outputs, FBA models are typically constrained with a biomass equation, a reaction that equates total biomass production as the sum of lipids, carbohydrates, amino acids, and organic acids production in a specific composition (Saha et al., 2011). However, this approach may be restrictive when performing modelling tasks as all the biomass components were fixed in a composition with no degree of flexibility. Setting the accumulation of biomass components as individual transporters, however, is a more convenient approach as the fluxes for these components can be set independently (Poolman et al., 2013). The same approach was applied in this thesis, where all inputs and outputs were set as individual transporters and the fluxes could be set independently. This has allowed certain transporters such as for cysteine, caffeate and neoxanthin to have flexibility with their degradation rates, and this allowed a feasible flux distribution to be found when modelling the ripening transitions.

6.2.2 Modelling ripening transitions using static FBAs

This thesis also demonstrated that fruit development can be modelled using separate static FBAs instead of using dynamic modelling approaches

such as kinetic modelling and dynamic FBA (DFBA), which required kinetic values as model parameters. In other fruit development modelling studies, a process-based modelling approach was used. The approach has been applied to model the fruit development stages of peaches (*Prunus persica)* (Génard et al., 2003), grapes (*Vitis vinifera*) (Dai et al., 2010), and tomatoes (*Solanum lycopersicum)* (Bertin et al., 2003; Liu et al., 2007).

The framework of a process-based model is a set of differential and algebraic equations that represents the amount of carbon change in compounds such as sugars over time and/or the change of respiration flow of carbon, for example (Génard et al., 2003; Génard & Souty, 1996). Thus this modelling technique require parameters such as metabolite transfer function coefficient, compound carbon content, and growth respiration coefficient to constrain the model, which consist of processes that are known to occur during fruit development such as transpiration, respiration, and photosynthesis (Génard et al., 2003; Génard & Souty, 1996). These data can be obtained from published literature as demonstrated by Génard and Souty (1996), who modelled the final rapid growth stage of peach using this approach. Although the model only consisted of five equations, reducing the difficulties and the need to find a large amount of parameter data, it could not provide a detailed map of the carbon flows through the metabolic network as is possible with FBA. Nevertheless, the model was useful to predict plant responses such as the changes in sugar content, to environmental changes such as water content and temperature (Génard & Souty, 1996).

Due to limited quantitative studies on the regulation of secondary metabolism, these process-based model were not able to simulate the production of secondary compounds such as carotenoids which are essential for the nutritional quality of fruits (Génard et al., 2007). Thus, process-based models usually tend to reproduce the early stages of fruit development, such as modelling the dynamic behaviour of cell proliferation during the early stages of tomato fruit development (Bertin et al., 2003). This emphasises the practicality of FBA as the technique to model plant metabolic networks as the appropriate data needed for this approach is more widely available at the moment.

6.3 Understanding fruit biology

This thesis has shown that by using modelling to study the predicted flux distributions during ripening, it was possible to connect underlying metabolic mechanisms to the known metabolic processes that happen during the later stages of fruit development. This is helpful as metabolite profiles have revealed that metabolites in a common pathway or group of reactions tend to change in a concerted fashion but is unable to provide greater information on how and why they are interdependent on each other (Carrari et al., 2006).

The approach also provided an insight into the underlying mechanisms of the processes that happens during tomato fruit ripening. For example, in chapter 4, higher CO_2 release during breaker stage signifying climacteric respiration, was attributable to lower fluxes in the CO_2 fixing reactions than in CO_2 releasing reactions. In addition, it was found that the main contributor to CO_2 production was from cytosolic reactions, in contrast to my expectation that

the main contributor to CO_2 release would be from the mitochondrial TCA cycle as found in several plant metabolic flux analysis (MFA) studies (Sweetlove et al., 2013). Notably, the CO_2 releasing cytosolic reactions provided the intermediates for the production of secondary metabolite precursors. This suggested that climacteric respiration is a consequence of a mechanism to supply intermediates for secondary metabolite synthesis. This is an important finding because the nature and cause of the climacteric has long been a mystery.

6.4 Future work

6.4.1 Further model refinement

The model development process is an iterative one. As such, it is important to continue to refine the tomato metabolic model to improve its predictive capabilities. Firstly, the model can be further curated to be able to accumulate or degrade other metabolites which were not taken into account in this thesis such as cell wall polymers. This will expand the scope of the model to reproduce other developmental stages or metabolic processes.

As the metabolic model LycoCyc is based on automated genome annotations which are prone to errors, the constructed model will also have acquired these errors, such as the inclusion of reactions that may not exist in plants. An example is pyruvate synthase, a reaction that converts pyruvate into acetyl-coA, which is typically found in bacteria and is not known to exist in plants. This reaction was automatically imported into the model by ScrumPy

from LycoCyc 3.0 as it was a reaction entry in the database although no tomato gene was associated with the enzyme. As the tomato metabolic network contains more than 2000 reactions, this error was only spotted when the modelling tasks were completed. It was found that pyruvate synthase acted as the dominant reaction to supply acetyl-coA rather than ATP-citrate lyase in both of the ripening transitions modelled. More extensive modelling work, activating the full range of metabolic capabilities of the genome-scale model would be required to identify other such spurious reactions.

6.4.2 Redistributing the fluxes for reductant supply

In Chapter 5, pushing the lycopene accumulation rate to its limit resulted in a dramatic change in flux distribution, in which high fluxes were exchanged via several aminotransferases across three subcellular compartments. This was a way for the network to balance the fluxes in order to meet the high reductant requirements following higher demand for fluxes through the MEP pathway to support high lycopene accumulation. However, it was found that NADPH was mainly produced by plastidic malate dehydrogenase (MDH) whereas the oxidative pentose phosphate pathway (OPPP) only carried minute fluxes (less than 0.1 μmol/gFW/day). The use of alternative dehydrogenases in preference to using OPPP was also predicted in other plant systems FBAs. In the Arabidopsis model, NADPH was mainly produced by NADP-glyceraldehyde dehydrogenase (GAPDH) while OPPP did not carry any flux (Poolman et al., 2009; Williams et al., 2010). Similarly, the rapeseed FBA preferred plastidial dehydrogenases than OPPP to generate NADPH (Hay & Schwender, 2011a). However, the OPPP is established as an important source for NADPH (Kruger

& von Schaewen, 2003), thus redirecting flux towards this pathway as a preference for the supply of reductants would generate a more realistic flux distribution in terms of meeting reductant demands (Cheung et al., 2013). This can be achieved in the model by restricting the plastidial NADPH-dehydrogenases to operate towards the direction of NADPH consumption as demonstrated in a recent Arabidopsis FBA model (Cheung et al., 2013).

6.4.3 Exploring off-vine ripening

The attempts to model off-vine ripening using the modelling approach in this thesis yielded no feasible flux distributions. This may be due to the fundamental issue of carbon balance which is discussed in Chapter 4. The quality of the outcomes from this off-vine modelling could be improved further with the use of other optimisation techniques. Other optimisation techniques for FBA includes mixed integer linear programming (MILP), quadratic programming (QP) and non-linear programming (NLP) (Lee et al., 2006). These techniques are effectively different in the way they explore the feasible solution space for the optimal flux distribution within the applied constraints. Thus, it would be interesting if an optimal flux distribution could be found within the applied constraints of off-vine ripening during BR-TU by applying these different optimisation techniques. This will lead towards identifying the metabolite composition that can be accumulated with pre-existing input metabolites during BR-TU without any additional carbon or nitrogen supply. The optimal flux distribution predicted will then provide information on which metabolic function was perturbed in order to efficiently consume the limited resources and the cost of the end fruit metabolite composition.

It would also be interesting to combine this model with metabolic profiles of off-vine ripened tomatoes. This would also provide the opportunity to compare the changes in the metabolic functions between on- and off-vine ripened tomatoes. This would shed light on why there are differences in the metabolite compositions of on- and off-vine ripened tomatoes (Arias et al., 2000; Sorrequieta et al., 2013). To date, there is a complete metabolite profile for all development stages of on-vine ripened tomatoes which were used in this thesis (Baxter et al., 2005; Carrari & Fernie, 2006), but not many were reported for off-vine ripened tomatoes. There is one, however, which profiled the metabolites of off-vine ripened Micro-Tom tomatoes but only for mature green and red stages of ripening (Sorrequieta et al., 2013).

6.5 Summary

This thesis has shown the application of integrating metabolite profiling data with metabolic modelling to gain a different perspective on the metabolic processes underlying tomato fruit ripening. Modelling tomato fruit ripening with increased lycopene accumulation has also demonstrated that the model can be used in manipulating the metabolic network to predict the effects without performing any labour extensive experiments. Such an approach not only reduces the cost, but also provides an initial step toward designing metabolic engineering strategies.

References

Abdul-Baki AA, McCollum JP, Dickinson DB (1965) The respiratory pattern in the tomato fruit and its alteration by infiltration with various chemicals. Plant Physiol **40**: 611–4

Agarwal S, Rao AV (2000) Tomato lycopene and its role in human health and chronic diseases. Can Med Assoc J **163**: 739–44

Akihiro T, Koike S, Tani R, Tominaga T, Watanabe S, Iijima Y, Aoki K, Shibata D, Ashihara H, Matsukura C, Akama K, Fujimura T, Ezura H (2008) Biochemical mechanism on GABA accumulation during fruit development in tomato. Plant Cell Physiol **49**: 1378–89

Allen DK, Ohlrogge JB, Shachar-Hill Y (2009) The role of light in soybean seed filling metabolism. Plant J **58**: 220–34

Allen DK, Young JD (2013) Carbon and nitrogen provisions alter the metabolic flux in developing soybean embryos. Plant Physiol **161**: 1458–75

Allen SM, Kader AA, Albright-Holton M, Algazi M (1977) Genotypic variation for flavor and composition in fresh market tomatoes. J Am Soc Hortic Sci **102**: 680–689

Alper H, Jin Y-S, Moxley JF, Stephanopoulos G (2005) Identifying gene targets for the metabolic engineering of lycopene biosynthesis in Escherichia coli. Metab Eng **7**: 155–64

Andrews J (1995) The climacteric respiration rise in attached and detached tomato fruit. Postharvest Biol Technol **44**: 287–292

Andriotis VME, Kruger NJ, Pike MJ, Smith AM (2010) Plastidial glycolysis in developing Arabidopsis embryos. New Phytol **185**: 649–62

Araújo WL, Ishizaki K, Nunes-Nesi A, Tohge T, Larson TR, Krahnert I, Balbo I, Witt S, Dörmann P, Graham IA, Leaver CJ, Fernie AR (2011) Analysis of a range of catabolic mutants provides evidence that phytanoyl-coenzyme A does not act as a substrate of the electron-transfer flavoprotein/electron-transfer flavoprotein:ubiquinone oxidoreductase complex in Arabidopsis during dark-induced senescence. Plant Physiol **157**: 55–69

Arias R, Lee T-C, Specca D, Janes H (2000) Quality comparison of hydroponic tomatoes (*Lycopersicon esculentum*) ripened on and off vine. J Food Sci **65**: 545–548

Arnold A, Nikoloski Z (2013) Comprehensive classification and perspective for modelling photorespiratory metabolism. Plant Biol **15**: 667–75

Bautista EJ, Zinski J, Szczepanek SM, Johnson EL, Tulman ER, Ching W-M, Geary SJ, Srivastava R (2013) Semi-automated curation of metabolic models via flux balance analysis: a case study with *Mycoplasma gallisepticum*. PLoS Comput Biol **9**: e1003208

Baxter CJ, Carrari F, Bauke A, Overy S, Hill SA, Quick PW, Fernie AR, Sweetlove LJ (2005) Fruit carbohydrate metabolism in an introgression line of tomato with increased fruit soluble solids. Plant Cell Physiol **46**: 425–37

Becker J, Zelder O, Häfner S, Schröder H, Wittmann C (2011) From zero to hero--design-based systems metabolic engineering of *Corynebacterium glutamicum* for L-lysine production. Metab Eng **13**: 159–68

Beckles DM (2012) Factors affecting the postharvest soluble solids and sugar content of tomato (Solanum lycopersicum L.) fruit. Postharvest Biol Technol **63**: 129–140

Bennett AB, Smith GM, Nichols BG (1987) Regulation of climacteric respiration in ripening avocado fruit. Plant Physiol **83**: 973–6

Bentley FK, Zurbriggen A, Melis A (2014) Heterologous expression of the mevalonic acid pathway in cyanobacteria enhances endogenous carbon partitioning to isoprene. Mol Plant **7**: 71–86

Bertin N, Genard M, Fishman S (2003) A model for an early stage of tomato fruit development: cell multiplication and cessation of the cell proliferative activity. Ann Bot **92**: 65–72

Bick JA, Lange BM (2003) Metabolic cross talk between cytosolic and plastidial pathways of isoprenoid biosynthesis: unidirectional transport of intermediates across the chloroplast envelope membrane. Arch Biochem Biophys **415**: 146–154

Bisogni CA, Armbruster G, Brecht PE (1976) Quality comparisons of room ripened and field ripened tomato fruits. J Food Sci **41**: 333–338

Bombarely A, Menda N, Tecle IY, Buels RM, Strickler S, Fischer-York T, Pujar A, Leto J, Gosselin J, Mueller LA (2011) The Sol Genomics Network (solgenomics.net): growing tomatoes using Perl. Nucleic Acids Res **39**: D1149–55

Budman H, Patel N, Tamer M, Al-Gherwi W (2013) A dynamic metabolic flux balance based model of fed-batch fermentation of *Bordetella pertussis*. Biotechnol Prog **29**: 520–531

Bush DR (1993) Proton-coupled sugar and amino acid transporters in plants. Annu Rev Plant Physiol Plant Mol Biol **44**: 513–542

Butelli E, Titta L, Giorgio M, Mock H-P, Matros A, Peterek S, Schijlen EGWM, Hall RD, Bovy AG, Luo J, Martin C (2008) Enrichment of tomato fruit with health-promoting anthocyanins by expression of select transcription factors. Nat Biotechnol **26**: 1301–8

Calık P, Sahin M, Taşpınar H, Soyaslan EŞ, Inankur B (2011) Dynamic flux balance analysis for pharmaceutical protein production by *Pichia pastoris*: human growth hormone. Enzyme Microb Technol **48**: 209–16

Canene-Adams K, Campbell JK, Zaripheh S, Jeffery EH, Erdman JW (2005) The tomato as a functional food. J Nutr **135**: 1226–1230

Carli P, Arima S, Fogliano V, Tardella L, Frusciante L, Ercolano MR (2009) Use of network analysis to capture key traits affecting tomato organoleptic quality. J Exp Bot **60**: 3379–86

Carrari F, Asis R, Fernie AR (2007) The metabolic shifts underlying tomato fruit development. Plant Mol Biol **55**: 45–55

Carrari F, Baxter C, Usadel B, Urbanczyk-Wochniak E, Zanor M-I, Nunes-Nesi A, Nikiforova V, Centero D, Ratzka A, Pauly M, Sweetlove LJ, Fernie AR (2006) Integrated analysis of metabolite and transcript levels reveals the metabolic shifts that underlie tomato fruit development and highlight regulatory aspects of metabolic network behavior. Plant Physiol **142**: 1380–96

Carrari F, Fernie AR (2006) Metabolic regulation underlying tomato fruit development. J Exp Bot **57**: 1883–97

Caspeta L, Shoaie S, Agren R, Nookaew I, Nielsen J (2012) Genome-scale metabolic reconstructions of *Pichia stipitis* and *Pichia pastoris* and *in silico* evaluation of their potentials. BMC Syst Biol **6**: 24

Centeno DC, Osorio S, Nunes-Nesi A, Bertolo ALF, Carneiro RT, Araújo WL, Steinhauser M-C, Michalska J, Rohrmann J, Geigenberger P, Oliver SN, Stitt M, Carrari F, Rose JKC, Fernie AR (2011) Malate plays a crucial role in starch metabolism, ripening, and soluble solid content of tomato fruit and affects postharvest softening. Plant Cell **23**: 162–84

Cercós M, Soler G, Iglesias DJ, Gadea J, Forment J, Talón M (2006) Global analysis of gene expression during development and ripening of citrus fruit flesh. A proposed mechanism for citric acid utilization. Plant Mol Biol **62**: 513–27

Cheung CYM, Poolman MG, Fell D, Ratcliffe RG, Sweetlove LJ (2014) A diel flux-balance model captures interactions between light and dark metabolism during day-night cycles in C3 and CAM leaves. Plant Physiol. doi: 10.1104/pp.113.234468

Cheung CYM, Williams TCR, Poolman MG, Fell DA, Ratcliffe RG, Sweetlove LJ (2013) A method for accounting for maintenance costs in flux balance analysis improves the prediction of plant cell metabolic phenotypes under stress conditions. Plant J **75**: 1050–61

Chung BK-S, Lakshmanan M, Klement M, Mohanty B, Lee D-Y (2013) Genome-scale *in silico* modeling and analysis for designing synthetic terpenoid-producing microbial cell factories. Chem Eng Sci **103**: 100–108

Colón AM, Sengupta N, Rhodes D, Dudareva N, Morgan J (2010) A kinetic model describes metabolic response to perturbations and distribution of flux control in the benzenoid network of *Petunia hybrida*. Plant J **62**: 64–76

Cunningham FX, Pogson BJ, Sun Z, McDonald KA, DellaPenna D, Gantt E (1996) Functional analysis of the ß and epsilon-lycopene cyclase enzymes of Arabidopsis reveals a mechanism for control of cyclic carotenoid formation. Plant Cell **8**: 1613–1626

Curien G, Bastien O, Robert-Genthon M, Cornish-Bowden A, Cárdenas ML, Dumas R (2009) Understanding the regulation of aspartate metabolism using a model based on measured kinetic parameters. Mol Syst Biol **5**: 271

Dai ZWW, Vivin P, Barrieu F, Ollat N, Delrot S (2010) Physiological and modelling approaches to understand water and carbon fluxes during grape berry growth and quality development: a review. Aust J Grape Wine Res **16**: 70–85

Dal'Molin CG de O, Nielsen LK (2013) Plant genome-scale metabolic reconstruction and modelling. Curr Opin Biotechnol **24**: 271–7

Dal'Molin CG de O, Quek L-E, Palfreyman RW, Brumbley SM, Nielsen LK (2010) AraGEM, a genome-scale reconstruction of the primary metabolic network in Arabidopsis. Plant Physiol **152**: 579–89

Dal'Molin CG de O, Quek L-E, Palfreyman RW, Brumbley SM, Nielsen LK (2010) C4GEM, a genome-scale metabolic model to study C4 plant metabolism. Plant Physiol **154**: 1871–85

DellaPenna D (2001) Plant metabolic engineering. Plant Physiol **125**: 160–3

Edwards JS, Ibarra RU, Palsson BO (2001) *In silico* predictions of *Escherichia coli* metabolic capabilities are consistent with experimental data. Nat Biotechnol **19**: 125–30

Edwards JS, Palsson BO (1999) Systems properties of the *Haemophilus influenzae* Rd metabolic genotype. J Biol Chem **274**: 17410–17416

Egea I, Bian W, Barsan C, Jauneau A, Pech J-C, Latché A, Li Z, Chervin C (2011) Chloroplast to chromoplast transition in tomato fruit: spectral

confocal microscopy analyses of carotenoids and chlorophylls in isolated plastids and time-lapse recording on intact live tissue. Ann Bot **108**: 291–7

Eisenreich W, Rohdich F, Bacher A (2001) Deoxyxylulose phosphate pathway to terpenoids. Trends Plant Sci **6**: 78–84

Enfissi EM A, Barneche F, Ahmed I, Lichtlé C, Gerrish C, McQuinn RP, Giovannoni JJ, Lopez-Juez E, Bowler C, Bramley PM, Fraser PD (2010) Integrative transcript and metabolite analysis of nutritionally enhanced DE-ETIOLATED1 downregulated tomato fruit. Plant Cell **22**: 1190–215

Ettenhuber C, Radykewicz T, Kofer W, Koop H-U, Bacher A, Eisenreich W (2005) Metabolic flux analysis in complex isotopolog space. Recycling of glucose in tobacco plants. Phytochemistry **66**: 323–35

Fabi JP, Seymour GB, Graham NS, Broadley MR, May ST, Lajolo FM, Cordenunsi BR, Oliveira do Nascimento JR (2012) Analysis of ripening-related gene expression in papaya using an Arabidopsis-based microarray. BMC Plant Biol **12**: 242

Farhi M, Marhevka E, Ben-Ari J, Algamas-Dimantov A, Liang Z, Zeevi V, Edelbaum O, Spitzer-Rimon B, Abeliovich H, Schwartz B, Tzfira T, Vainstein A (2011) Generation of the potent anti-malarial drug artemisinin in tobacco. Nat Biotechnol **29**: 1072–4

Farmer WR, Liao JC (2001) Precursor balancing for metabolic engineering of lycopene production in *Escherichia coli*. Biotechnol Prog **17**: 57–61

Farmer WR, Liao JC (2000) Improving lycopene production in *Escherichia coli* by engineering metabolic control. Nat Biotechnol **18**: 533–7

Feist AM, Palsson BO (2010) The biomass objective function. Curr Opin Microbiol **13**: 344–9

Fell DA, Poolman MG, Gevorgyan A (2010) Building and analysing genome-scale metabolic models. Biochem Soc Trans **38**: 1197–201

Fell DA, Schuster S (2007) Part IV. Molecular networks. *In* T Lengauer, ed, Bioinformatics: From genomes to Therapies. pp 758–771

Förster J, Famili I, Fu P, Palsson BØ, Nielsen J (2003) Genome-scale reconstruction of the *Saccharomyces cerevisiae* metabolic network. Genome Res **13**: 244–53

Fraser PD, Enfissi EMA, Halket JM, Truesdale MR, Yu D, Gerrish C, Bramley PM (2007) Manipulation of phytoene levels in tomato fruit: effects on isoprenoids, plastids, and intermediary metabolism. Plant Cell **19**: 3194–211

Fraser PD, Romer S, Shipton CA, Mills PB, Kiano JW, Misawa N, Drake RG, Schuch W, Bramley PM (2002) Evaluation of transgenic tomato plants expressing an additional phytoene synthase in a fruit-specific manner. Proc Natl Acad Sci U S A **99**: 1092–7

Fraser PD, Truesdale MR, Bird CR, Schuch W, Bramley PM (1994) Carotenoid biosynthesis during tomato fruit-development. Plant Physiol **105**: 405–413

Fray RG, Wallace A, Fraser PD, Valero D, Hedden P, Bramley PM, Grierson D (1995) Constitutive expression of a fruit phytoene synthase gene in transgenic tomatoes causes dwarfism by redirecting metabolites from the gibberellin pathway. Plant J **8**: 693–701

Gallardo F, Gfilvez S, Gadal P, Cánovas FM (1995) Changes in $NADP^+$-linked isocitrate dehydrogenase during tomato fruit ripening. Characterization of the predominant cytosolic enzyme from green and ripe pericarp. Planta **34**: 148–154

Génard M, Bertin N, Borel C, Bussières P, Gautier H, Habib R, Léchaudel M, Lecomte A, Lescourret F, Lobit P, Quilot B (2007) Towards a virtual fruit focusing on quality: modelling features and potential uses. J Exp Bot **58**: 917–28

Génard M, Lescourret F, Gomez L, Habib R (2003) Changes in fruit sugar concentrations in response to assimilate supply, metabolism and dilution: a modeling approach applied to peach fruit (*Prunus persica*). Tree Physiol **23**: 373–85

Génard M, Souty M (1996) Modeling the peach sugar contents in relation to fruit growth. J Am Soc Hortic Sci **121**: 1122–1131

Ghosh A, Zhao H, Price ND (2011) Genome-scale consequences of cofactor balancing in engineered pentose utilization pathways in *Saccharomyces cerevisiae*. PLoS One **6**: e27316

Gillaspy G, Ben-David H, Gruissem W (1993) Fruits: A developmental perspective. Plant Cell **5**: 1439–1451

Giovannoni JJ (2004) Genetic regulation of fruit development and ripening. Plant Cell **16 Suppl**: S170–80

Grafahrend-Belau E, Junker A, Eschenroder A, Muller J, Schreiber F, Junker BH (2013) Multiscale metabolic modeling: dynamic flux balance analysis on a whole plant scale. Plant Physiol **163**: 637–347

Grafahrend-Belau E, Schreiber F, Koschützki D, Junker BH (2009) Flux balance analysis of barley seeds: a computational approach to study systemic properties of central metabolism. Plant Physiol **149**: 585–98

Hanly TJ, Henson MA (2013) Dynamic metabolic modeling of a microaerobic yeast co-culture: predicting and optimizing ethanol production from glucose/xylose mixtures. Biotechnol Biofuels **6**: 44

Hay J, Schwender J (2011a) Computational analysis of storage synthesis in developing *Brassica napus L.* (oilseed rape) embryos: flux variability analysis in relation to ^{13}C metabolic flux analysis. Plant J **67**: 513–25

Hay J, Schwender J (2011b) Metabolic network reconstruction and flux variability analysis of storage synthesis in developing oilseed rape (*Brassica napus L.*) embryos. Plant J **67**: 526–41

Heazlewood JL, Verboom RE, Tonti-Filippini J, Small I, Millar AH (2007) SUBA: the Arabidopsis subcellular database. Nucleic Acids Res **35**: D213–8

Henry CS, DeJongh M, Best AA, Frybarger PM, Linsay B, Stevens RL (2010) High-throughput generation, optimization and analysis of genome-scale metabolic models. Nat Biotechnol **28**: 977–82

Holzhütter H-G (2004) The principle of flux minimization and its application to estimate stationary fluxes in metabolic networks. Eur J Biochem **271**: 2905–22

Hong SH, Kim JS, Lee SY, In YH, Choi SS, Rih J-K, Kim CH, Jeong H, Hur CG, Kim JJ (2004) The genome sequence of the capnophilic rumen bacterium *Mannheimia succiniciproducens*. Nat Biotechnol **22**: 1275–81

Hörtensteiner S, Kräutler B (2011) Chlorophyll breakdown in higher plants. Biochim Biophys Acta **1807**: 977–88

Hubbard NL, Pharr DM, Huber SC (1990) Role of sucrose phosphate synthase in sucrose biosynthesis in ripening bananas and its relationship to the respiratory climacteric. Plant Physiol **94**: 201–8

Hulme AC, Jones JD, Wooltorton LSC (1963) The respiration climacteric in apple fruits. Proc R Soc B Biol Sci **158**: 514–535

Ischebeck T, Zbierzak AM, Kanwischer M, Dörmann P (2006) A salvage pathway for phytol metabolism in Arabidopsis. J Biol Chem **281**: 2470–7

Jouhten P, Wiebe M, Penttilä M (2012) Dynamic flux balance analysis of the metabolism of *Saccharomyces cerevisiae* during the shift from fully respirative or respirofermentative metabolic states to anaerobiosis. FEBS J **279**: 3338–54

Kader AA (2008) Flavor quality of fruits and vegetables. J Sci Food Agric **88**: 1863–1868

Kader AA, Stevens MA, Albright-Holton M, Morris LL, Algazi M (1977) Effect of fruit ripeness when picked on flavor and composition in fresh market tomatoes. J Am Soc Hortic Sci **102**: 724–731

Karp PD, Ouzounis C a, Moore-Kochlacs C, Goldovsky L, Kaipa P, Ahrén D, Tsoka S, Darzentas N, Kunin V, López-Bigas N (2005) Expansion of the BioCyc collection of pathway/genome databases to 160 genomes. Nucleic Acids Res **33**: 6083–9

Katz E, Boo KH, Kim HY, Eigenheer RA, Phinney BS, Shulaev V, Negre-Zakharov F, Sadka A, Blumwald E (2011) Label-free shotgun proteomics and metabolite analysis reveal a significant metabolic shift during citrus fruit development. J Exp Bot **62**: 5367–84

Kauffman KJ, Prakash P, Edwards JS (2003) Advances in flux balance analysis. Curr Opin Biotechnol **14**: 491–496

Kaur D, Sharma R, Abas Wani A, Singh Gill B, Sogi DS (2006) Physicochemical changes in seven tomato (*Lycopersicon esculentum*) cultivars during ripening. Int J Food Prop **9**: 747–757

Keseler IM, Mackie A, Peralta-Gil M, Santos-Zavaleta A, Gama-Castro S, Bonavides-Martínez C, Fulcher C, Huerta AM, Kothari A, Krummenacker M, et al. (2013) EcoCyc: fusing model organism databases with systems biology. Nucleic Acids Res **41**: D605–12

Kim D, Filtz MR, Proteau PJ (2004) The methylerythritol phosphate pathway contributes to carotenoid but not phytol biosynthesis in *Euglena gracilis*. J Nat Prod **67**: 1067–9

Kim S, Keasling JD (2001) Metabolic engineering of the nonmevalonate isopentenyl diphosphate synthesis pathway in *Escherichia coli* enhances lycopene production. Biotechnol Bioeng **72**: 408–415

Klee HJ, Giovannoni JJ (2011) Genetics and control of tomato fruit ripening and quality attributes. Annu Rev Genet **45**: 41–59

Koia JH, Moyle RL, Botella JR (2012) Microarray analysis of gene expression profiles in ripening pineapple fruits. BMC Plant Biol **12**: 240

Krinsky NI, Johnson EJ (2005) Carotenoid actions and their relation to health and disease. Mol Aspects Med **26**: 459–516

Kruger NJ, Ratcliffe RG (2009) Insights into plant metabolic networks from steady-state metabolic flux analysis. Biochimie **91**: 697–702

Kruger NJ, von Schaewen A (2003) The oxidative pentose phosphate pathway: structure and organisation. Curr Opin Plant Biol **6**: 236–246

Lakshmanan M, Zhang Z, Mohanty B, Kwon J-Y, Choi H-Y, Nam H-J, Kim D-I, Lee D-Y (2013) Elucidating rice cell metabolism under flooding and drought stresses using flux-based modeling and analysis. Plant Physiol **162**: 2140–50

Lee JM, Gianchandani EP, Papin JA (2006) Flux balance analysis in the era of metabolomics. Brief Bioinform **7**: 140–50

Liu H-F, Génard M, Guichard S, Bertin N (2007) Model-assisted analysis of tomato fruit growth in relation to carbon and water fluxes. J Exp Bot **58**: 3567–80

Lois LM, Rodríguez-Concepción M, Gallego F, Campos N, Boronat A (2000) Carotenoid biosynthesis during tomato fruit development: regulatory role of 1-deoxy-D-xylulose 5-phosphate synthase. Plant J **22**: 503–513

Luo R, Wei H, Ye L, Wang K, Chen F, Luo L, Liu L, Li Y (2009) Photosynthetic metabolism of C3 plants shows highly cooperative regulation under changing environments : Proc Natl Acad Sci U S A **106**: 847–852

Ma SM, Garcia DE, Redding-Johanson AM, Friedland GD, Chan R, Batth TS, Haliburton JR, Chivian D, Keasling JD, Petzold CJ, Lee TS, Chhabra SR (2011) Optimization of a heterologous mevalonate pathway through the use of variant HMG-CoA reductases. Metab Eng **13**: 588–97

Mahadevan R, Edwards JS, Doyle FJ (2002) Dynamic flux balance analysis of diauxic growth in *Escherichia coli*. Biophys J **83**: 1331–40

Malacrida C, Valle EM, Boggio SB (2006) Postharvest chilling induces oxidative stress response in the dwarf tomato cultivar Micro-Tom. Physiol Plant **127**: 10–18

Malundo TMM, Shewfelt RL, Scott JW (1995) Flavor quality of fresh tomato (*Lycopersicon esculentum* Mill.) as affected by sugar and acid levels. Postharvest Biol Technol **6**: 103–110

Martin C, Bassolino L, Zhang Y, Schoonbeek H, Kiferle C, Perata P (2013) Accumulation of anthocyanins in tomato skin extends shelf life. New Phytol **200**: 650–655

Martin C, Butelli E, Petroni K, Tonelli C (2011) How can research on plants contribute to promoting human health? Plant Cell **23**: 1685–99

Martin C, Zhang Y, Tonelli C, Petroni K (2013) Plants, diet, and health. Annu Rev Plant Biol **64**: 19–46

Martin VJJ, Pitera DJ, Withers ST, Newman JD, Keasling JD (2003) Engineering a mevalonate pathway in *Escherichia coli* for production of terpenoids. Nat Biotechnol **21**: 796–802

Masakapalli SK, Kruger NJ, Ratcliffe RG (2013) The metabolic flux phenotype of heterotrophic Arabidopsis cells reveals a complex response to changes in nitrogen supply. Plant J **74**: 569–82

Matas AJ, Yeats TH, Buda GJ, Zheng Y, Chatterjee S, Tohge T, Ponnala L, Adato A, Aharoni A, Stark R, Fernie AR, Fei Z, Giovannoni JJ, Rose JKC (2011) Tissue- and cell-type specific transcriptome profiling of expanding tomato fruit provides insights into metabolic and regulatory specialization and cuticle formation. Plant Cell **23**: 3893–3910

Matthews PD, Wurtzel ET (2000) Metabolic engineering of carotenoid accumulation in *Escherichia coli* by modulation of the isoprenoid precursor pool with expression of deoxyxylulose phosphate synthase. Appl Microbiol Biotechnol **53**: 396–400

McNeil SD, Nuccio ML, Ziemak MJ, Hanson AD (2001) Enhanced synthesis of choline and glycine betaine in transgenic tobacco plants that overexpress phosphoethanolamine N-methyltransferase. Proc Natl Acad Sci U S A **98**: 10001–5

McNeil SD, Rhodes D, Russell BL, Nuccio ML, Shachar-Hill Y, Hanson AD (2000) Metabolic modeling identifies key constraints on an engineered glycine betaine synthesis pathway in tobacco. Plant Physiol **124**: 153–62

Meadows AL, Karnik R, Lam H, Forestell S, Snedecor B (2010) Application of dynamic flux balance analysis to an industrial *Escherichia coli* fermentation. Metab Eng **12**: 150–60

Milo R, Last RL (2012) Achieving diversity in the face of constraints: lessons from metabolism. Science **336**: 1663–7

Mintz-Oron S, Meir S, Malitsky S, Ruppin E, Aharoni A, Shlomi T (2012) Reconstruction of Arabidopsis metabolic network models accounting for subcellular compartmentalization and tissue-specificity. Proc Natl Acad Sci 1–6

Mo ML, Palsson BO, Herrgård MJ (2009) Connecting extracellular metabolomic measurements to intracellular flux states in yeast. BMC Syst Biol **3**: 37

Morgan JA, Rhodes D (2002) Mathematical modeling of plant metabolic pathways. Metab Eng **4**: 80–9

Morgan MJ, Osorio S, Gehl B, Baxter CJ, Kruger NJ, Ratcliffe RG, Fernie AR, Sweetlove LJ (2013) Metabolic engineering of tomato fruit organic acid content guided by biochemical analysis of an introgression line. Plant Physiol **161**: 397–407

Mueller LA, Solow TH, Taylor N, Skwarecki B, Buels R, Binns J, Lin C, Wright MH, Ahrens R, Wang Y, Herbst E V, Keyder ER, Menda N,

Zamir D, Tanksley SD (2005) The SOL Genomics Network: a comparative resource for Solanaceae biology and beyond. Plant Physiol **138**: 1310–7

Muller J, EschenrOder A, Christen O (2012) ProNet-CN Model: A dynamic and multi-scale process network combining photosynthesis, primary carbon metabolism and effects of leaf nitrogen status. IEEE 4th Int. Symp. Plant Growth Model. Simulation, Vis. Appl. pp 289–296

Munoz-Bertomeu J, Cascales-Minana B, Alaiz M, Segura J, Ros R (2010) A critical role of plastidial glycolytic glyceraldehyde-3-phosphate dehydrogenase in the control of plant metabolism and development. Plant Signal Behav **5**: 67–69

Oberhardt MA, Palsson BØ, Papin J a (2009) Applications of genome-scale metabolic reconstructions. Mol Syst Biol **5**: 320

Oberhuber M, Berghold J, Breuker K, Hortensteiner S, Krautler B (2003) Breakdown of chlorophyll: a nonenzymatic reaction accounts for the formation of the colorless “nonfluorescent” chlorophyll catabolites. Proc Natl Acad Sci U S A **100**: 6910–5

Oms-Oliu G, Hertog MLATM, Van de Poel B, Ampofo-Asiama J, Geeraerd AH, Nicolaï BM (2011) Metabolic characterization of tomato fruit during preharvest development, ripening, and postharvest shelf-life. Postharvest Biol Technol **62**: 7–16

Orth JD, Thiele I, Palsson BØ (2010) What is flux balance analysis? Nat Biotechnol **28**: 245–8

Osorio S, Alba R, Damasceno CMB, López-Casado G, Lohse M, Zanor MI, Tohge T, Usadel B, Rose JKC, Fei Z, Giovannoni JJ, Fernie AR (2011) Systems biology of tomato fruit development: combined transcript, protein and metabolite analysis of tomato transcription factor (nor, rin) and ethylene receptor (Nr) mutants reveals novel regulatory interactions. Plant Physiol **157**: 405–25

Pagliarini E, Monteleone E, Ratti S (2001) Sensory profile of eight tomato cultivars (*Lycopersicon esculentum*) and its relationship to consumer preference. Ital J Food Sci **13**: 285–296

Park JH, Lee KH, Kim TY, Lee SY (2007) Metabolic engineering of Escherichia coli for the production of L-valine based on transcriptome analysis and in silico gene knockout simulation. Proc Natl Acad Sci U S A **104**: 7797–802

Pek Z, Helyes L, Lugasi A (2010) Color changes and antioxidant content of vine and postharvest-ripened tomato fruits. HortScience **45**: 466–468

Pilalis E, Chatziioannou A, Thomasset B, Kolisis F (2011) An *in silico* compartmentalized metabolic model of *Brassica napus* enables the

systemic study of regulatory aspects of plant central metabolism. Biotechnol Bioeng **108**: 1673–82

Pitera DJ, Paddon CJ, Newman JD, Keasling JD (2007) Balancing a heterologous mevalonate pathway for improved isoprenoid production in *Escherichia coli*. Metab Eng **9**: 193–207

Poolman MG (2006) ScrumPy: metabolic modelling with Python. Syst Biol (Stevenage) **153**: 375–8

Poolman MG, Assmus HE, Fell DA (2004) Applications of metabolic modelling to plant metabolism. J Exp Bot **55**: 1177–86

Poolman MG, Fell DA, Thomas S (2000) Modelling photosynthesis and its control. J Exp Bot **51 Spec No**: 319–28

Poolman MG, Kundu S, Shaw R, Fell DA (2013) Responses to light intensity in a genome-scale model of rice metabolism. Plant Physiol **162**: 1060–72

Poolman MG, Miguet L, Sweetlove LJ, Fell DA (2009) A genome-scale metabolic model of Arabidopsis and some of its properties. Plant Physiol **151**: 1570–81

Poolman MG, Olçer H, Lloyd JC, Raines CA, Fell DA (2001) Computer modelling and experimental evidence for two steady states in the photosynthetic Calvin cycle. Eur J Biochem **268**: 2810–6

Powell ALT, Nguyen C V, Hill T, Cheng KL, Figueroa-Balderas R, Aktas H, Ashrafi H, Pons C, Fernández-Muñoz R, Vicente A, Lopez-Baltazar J, Barry CS, Liu Y, Chetelat R, Granell A, Van Deynze A, Giovannoni JJ, Bennett AB (2012) Uniform ripening encodes a Golden 2-like transcription factor regulating tomato fruit chloroplast development. Science **336**: 1711–5

Prabhakar V, Löttgert T, Geimer S, Dörmann P, Krüger S, Vijayakumar V, Schreiber L, Göbel C, Feussner K, Feussner I, Marin K, Staehr P, Bell K, Flügge U-I, Häusler RE (2010) Phospho*enol*pyruvate provision to plastids is essential for gametophyte and sporophyte development in *Arabidopsis thaliana*. Plant Cell **22**: 2594–617

Radrich K, Tsuruoka Y, Dobson P, Gevorgyan A, Swainston N, Baart G, Schwartz J-M (2010) Integration of metabolic databases for the reconstruction of genome-scale metabolic networks. BMC Syst Biol **4**: 114

Raffo A, Leonardi C, Fogliano V, Ambrosino P, Salucci M, Gennaro L, Bugianesi R, Giuffrida F, Quaglia G (2002) Nutritional value of cherry tomatoes (*Lycopersicon esculentum* cv. Naomi F1) harvested at different ripening stages. J Agric Food Chem **50**: 6550–6

Rao AV, Rao LG (2007) Carotenoids and human health. Pharmacol Res **55**: 207–16

Ré MD, Gonzalez C, Sdrigotti MA, Sorrequieta A, Valle EM, Boggio SB (2012) Ripening tomato fruit after chilling storage alters protein turnover. J Sci Food Agric **92**: 1490–6

Rios-Estepa R, Lange I, Lee JM, Lange BM (2010) Mathematical modeling-guided evaluation of biochemical, developmental, environmental, and genotypic determinants of essential oil composition and yield in peppermint leaves. Plant Physiol **152**: 2105–19

Rios-Estepa R, Turner GW, Lee JM, Croteau RB, Lange BM (2008) A systems biology approach identifies the biochemical mechanisms regulating monoterpenoid essential oil composition in peppermint. Proc Natl Acad Sci U S A **105**: 2818–23

Ro D-K, Paradise EM, Ouellet M, Fisher KJ, Newman KL, Ndungu JM, Ho KA, Eachus RA, Ham TS, Kirby J, Chang MCY, Withers ST, Shiba Y, Sarpong R, Keasling JD (2006) Production of the antimalarial drug precursor artemisinic acid in engineered yeast. Nature **440**: 940–3

Rocha M, Licausi F, Araújo WL, Nunes-Nesi A, Sodek L, Fernie AR, van Dongen JT (2010) Glycolysis and the tricarboxylic acid cycle are linked by alanine aminotransferase during hypoxia induced by waterlogging of *Lotus japonicus*. Plant Physiol **152**: 1501–13

Rodríguez-Concepción M (2010) Supply of precursors for carotenoid biosynthesis in plants. Arch Biochem Biophys **504**: 118–22

Rodríguez-Concepción M, Ahumada I, Diez-Juez E, Sauret-Güeto S, Lois LM, Gallego F, Carretero-Paulet L, Campos N, Boronat A (2001) 1-Deoxy-D-xylulose 5-phosphate reductoisomerase and plastid isoprenoid biosynthesis during tomato fruit ripening. Plant J **27**: 213–222

Roessner-Tunali U, Hegemann B, Lytovchenko A, Carrari F, Bruedigam C, Granot D, Fernie AR (2003) Metabolic profiling of transgenic tomato plants overexpressing hexokinase reveals that the influence of hexose phosphorylation diminishes during fruit development. Plant Physiol **133**: 84–99

Rohrmann J, Tohge T, Alba R, Osorio S, Caldana C, McQuinn RP, Arvidsson S, van der Merwe MJ, Riaño-Pachón DM, Mueller-Roeber B, Fei Z, Nesi AN, Giovannoni JJ, Fernie AR (2011) Combined transcription factor profiling, microarray analysis and metabolite profiling reveals the transcriptional control of metabolic shifts occurring during tomato fruit development. Plant J **68**: 999–1013

Rohwer JM (2012) Kinetic modelling of plant metabolic pathways. J Exp Bot **63**: 2275–92

Rohwer JM, Botha FC (2001) Analysis of sucrose accumulation in the sugar cane culm on the basis of in vitro kinetic data. **445**: 437–445

Ronen G, Cohen M, Zamir D, Hirschberg J (1999) Regulation of carotenoid biosynthesis during tomato fruit development: expression of the gene for lycopene epsilon-cyclase is down-regulated during ripening and is elevated in the mutant Delta. Plant J **17**: 341–351

Ruppin E, Papin JA, de Figueiredo LF, Schuster S (2010) Metabolic reconstruction, constraint-based analysis and game theory to probe genome-scale metabolic networks. Curr Opin Biotechnol **21**: 502–10

Saha R, Suthers PF, Maranas CD (2011) *Zea mays* iRS1563: A comprehensive genome-scale metabolic reconstruction of maize metabolism. PLoS One **6**: 12

Salunkhe DK, Jadhav SJ, Yu MH (1974) Quality and nutritional composition of tomato fruit as influenced by certain biochemical and physiological changes. Plant Foods Hum Nutr **24**: 85–113

Sato S, Tabata S, Hirakawa H, Asamizu E, Shirasawa K, Isobe S, Kaneko T, Nakamura Y, Shibata D, Aoki K, Egholm M, Knight J, Bogden R, Li C, Shuang Y, Xu X, Pan S, Cheng S, Liu X, Ren Y, Wang J, Albiero A, Pero F, Todesco S, Van Eck J, Buels R, Bombarely A, Gosselin J, Huang M, Leto J, Menda N, Strickler S, Mao L, Gao S, Tecle IY, York T, Zheng Y, Verbalov JT, Lee J, Zhong S, Mueller LA, Stiekema WJ, Ribeca P, Alioto T, Yang W, Huang S, Du Y, Zhang Z, Gao Ji, Guo Y, Wang X, Li Y, He J, Li C, Cheng Z, Zuo J, Ren J, Zhao J, Yan L, Jiang H, Wang B, Li H, Li Z, Fu F, Chen B, Han B, Feng Q, Fan D, Wang Y, Ling H, Xue Y, Ware D, McCombie WR, Lippman ZB, Chia J, Jiang K, Pasternak S, Gelley L, Kramer M, Anderson LK, Chang S, Royer SM, Shearer LA, Stack SM, Rose JKC, Xu Y, Eannetta N, Matas AJ, McQuinn R, Tanksley SD, Camara F, Guigo R, Rombauts S, Fawcett J, van de Peer Y, Zamir D, Liang C, Spannagl M, Gundlach H, Bruggmann R, Mayer K, Jia Z, Zhang J, Ye Z, Bishop GJ, Butcher S, Lopez-Cobollo R, Buchan D, Filippis I, Abbott J, Dixit R, Singh M, Singh A, Pal JK, Pandit A, Singh PK, Mahato AK, Dogra V, Gaikwad K, Sharma TR, Mohapatra T, Singh NK, Causse M, Rothan C, Schiex T, Noirot C, Bellec A, Klopp C, Delalande C, Berges H, Mariette J, Frasse P, Vautrin S, Zouine M, Latche A, Rousseau C, Regad F, Pech J, Philippot M, Bouzayen M, Pericard P, Osorio S, del Carmen AF, Monforte A, Granell A, Fernandez-Munoz R, Conte M, Luchtenstein G, Carrari F, De Bellis G, Fuligni F, Peano C, Grandillo S, Termolino P, Pietrella M, Fantini E, Falcone G, Fiore A, Giuliano G, Lopez L, Facella P, Perrotta G, Daddiego L, Bryan G, Orozco M, Pastor X, Torrents D, van Schriek MGM, Feron RMC, van Oeveren J, de Heer P, DaPonte L, Jacobs-Oomen S, Cariaso M, Prins , van Eijk MJT, Janssen A, van Haaren MJJ, Jo S, Kim J, Kwon S, Kin S, Koo D, Lee S, Hur C, Clouser C, Rico A, Hallab A, Gebhardt C, Klee K, Jocker A, Warfsmann J, Gobel U, Kawamura S, Yano K, Sherman JD, Fukuoka H, Negoro S,

Bhutty S, Chowdhury P, Chattopdhyay D, Datema E, Smit S, Schijlen EGWM, van de Belt J, van Haarst JC, Peters SA, van Staveren MJ, Henkens MHC, Mooyman PJW, Hesselink T, van Ham RCHJ, Jiang G, Droege M, Choi D, Kang B-C, Kim BD, Park M, Kim S, Yeom S-I, Lee Y-H, Choi Y-D, Li G, Gao J, Liu Y, Huang S, Fernandez-Pedrosa V, Vollado C, Zuniga S, Wang G, Cade R, Dietrich RA, Rogers J, Knapp S, Fei Z, White RA, Thannhauser TW, Giovannoni JJ, Botella MA, Gilbert L, Conzalez R, Goicoechea JL, Yu Y, Kudrna D, Collura K, Wissotski M, Wing R, Schoof H, Meyers BC, Gurazada AB, Green PJ, Mathur S, Vyas S, Solanke AU, Kumar R, Gupta V, Sharma AK, Khurana P, Khurana JP, Tyagi AK, Dalmay T, Mohorianu I, Walts B, Chamala S, Barbazuk WB, Li J, Guo H, Lee T-H, Wang Y, Zhang D, Paterson AH, Wang X, Tang H, Barone A, Chiusano ML, Ercolano MR, D'Agostino N, Di Filippo M, Traini A, Sanseverino W, Frusciante L, Seymour GB, Elharam M, Fu Y, Hua A, Kenton S, Lewis J, Lin S, Najar F, Lai H, Qin B, Qu C, Shi R, White D, White J, Xing Y, Yang K, Yi J, Yao Z, Zhou L, Roe BA, Vezzi A, D'Angelo M, Zimbello R, Schiavin R, Caniato E, Rigobello C, Campagna D, Vitulo N, Valle G, Nelson DR, De Paoli E, Szinay D, de Jong HH, Bai Y, Visser RGF, Lankhorst RMK, Beasley H, McLaren K, Nicholson C, Riddle C, Gianese G (2012) The tomato genome sequence provides insights into fleshy fruit evolution. Nature **485**: 635–41

Schallau K, Junker BH (2010) Simulating plant metabolic pathways with enzyme-kinetic models. Plant Physiol **152**: 1763–71

Schilling CH, Covert MW, Famili I, Church GM, Edwards JS, Palsson BO (2002) Genome-scale metabolic model of *Helicobacter pylori* 26695. J Bacteriol. doi: 10.1128/JB.184.16.000

Schomburg I, Chang A, Placzek S, Söhngen C, Rother M, Lang M, Munaretto C, Ulas S, Stelzer M, Grote A, Scheer M, Schomburg D (2013) BRENDA in 2013: integrated reactions, kinetic data, enzyme function data, improved disease classification: new options and contents in BRENDA. Nucleic Acids Res **41**: D764–72

Schuetz R, Kuepfer L, Sauer U (2007) Systematic evaluation of objective functions for predicting intracellular fluxes in *Escherichia coli*. Mol Syst Biol **3**: 119

Schwender J, Hay JO (2012) Predictive modeling of biomass component tradeoffs in *Brassica napus* developing oilseeds based on in silico manipulation of storage metabolism. Plant Physiol **160**: 1218–36

Schwender J, Ohlrogge J, Shachar-Hill Y (2004) Understanding flux in plant metabolic networks. Curr Opin Plant Biol **7**: 309–317

Schwender J, Shachar-Hill Y, Ohlrogge JB (2006) Mitochondrial metabolism in developing embryos of *Brassica napus*. J Biol Chem **281**: 34040–7

Segrè D, Vitkup D, Church GM (2002) Analysis of optimality in natural and perturbed metabolic networks. Proc Natl Acad Sci U S A **99**: 15112–7

Shachar-Hill Y (2013) Metabolic network flux analysis for engineering plant systems. Curr Opin Biotechnol **24**: 247–55

Simkin AJ, Guirimand G, Papon N, Courdavault V, Thabet I, Ginis O, Bouzid S, Giglioli-Guivarc'h N, Clastre M (2011) Peroxisomal localisation of the final steps of the mevalonic acid pathway in planta. Planta **234**: 903–14

Sorrequieta A, Abriata L, Boggio SB, Valle EM (2013) Off-the-vine ripening of tomato fruit causes alteration in the primary metabolite composition. Metabolites **3**: 967–978

Sorrequieta A, Ferraro G, Boggio SB, Valle EM (2010) Free amino acid production during tomato fruit ripening: a focus on L-glutamate. Amino Acids **38**: 1523–32

Sriram G, Fulton DB, Iyer V V, Peterson JM, Zhou R, Westgate ME, Spalding MH, Shanks J V (2004) Quantification of compartmented metabolic fluxes in developing soybean embryos by employing biosynthetically directed fractional ^{13}C labeling , two-dimensional [^{13}C , ^{1}H] nuclear magnetic resonance , and comprehensive isotopomer balancing[1[w]]. Plant Physiol **136**: 3043–3057

Steinhauser M-C, Steinhauser D, Koehl K, Carrari F, Gibon Y, Fernie AR, Stitt M (2010) Enzyme activity profiles during fruit development in tomato cultivars and *Solanum pennellii*. Plant Physiol **153**: 80–98

Steuer R (2007) Computational approaches to the topology, stability and dynamics of metabolic networks. Phytochemistry **68**: 2139–51

Sweetlove LJ, Beard KFM, Nunes-Nesi A, Fernie AR, Ratcliffe RG (2010) Not just a circle: flux modes in the plant TCA cycle. Trends Plant Sci **15**: 462–70

Sweetlove LJ, Fernie AR (2005) Regulation of metabolic networks: understanding metabolic complexity in the systems biology era. New Phytol **168**: 9–24

Sweetlove LJ, Ratcliffe RG (2011) Flux-balance modeling of plant metabolism. Front Plant Physiol **2**: 1–10

Sweetlove LJ, Williams TCR, Cheung CYM, Ratcliffe RG (2013) Modelling metabolic CO2 evolution--a fresh perspective on respiration. Plant Cell Environ **36**: 1631–40

Tandon KS, Baldwin EA, Scott JW, Shewfelt RL (2003) Linking sensory descriptors to volatile and nonvolatile components of fresh tomato flavor. J Food Sci **68**: 2366–2371

Tanz SK, Castleden I, Hooper CM, Vacher M, Small I, Millar HA (2013) SUBA3: a database for integrating experimentation and prediction to define the SUBcellular location of proteins in Arabidopsis. Nucleic Acids Res **41**: D1185–91

Thiele I, Palsson BØ (2010) A protocol for generating a high-quality genome-scale metabolic reconstruction. Nat Protoc **5**: 93–121

Uys L, Botha FC, Hofmeyr J-HS, Rohwer JM (2007) Kinetic model of sucrose accumulation in maturing sugarcane culm tissue. Phytochemistry **68**: 2375–92

Vadali R V, Fu Y, Bennett GN, San K-Y (2005) Enhanced lycopene productivity by manipulation of carbon flow to isopentenyl diphosphate in *Escherichia coli*. Biotechnol Prog **21**: 1558–61

Valle EM, Boggio SB, Heldt HW (1998) Free amino acid composition of phloem sap and growing fruit of Lycopersicon esculentum. Plant cell Physiol **39**: 458–461

Verhoeven NM, Jakobs C (2001) Human metabolism of phytanic acid and pristanic acid. Prog Lipid Res **40**: 453–66

Voutilainen S, Nurmi T, Mursu J, Rissanen TH (2006) Carotenoids and cardiovascular health. Am J Clin Nutr **83**: 1265–71

Wanders RJA, Jansen GA, Lloyd MD (2003) Phytanic acid alpha-oxidation, new insights into an old problem: a review. Biochim Biophys Acta - Mol Cell Biol Lipids **1631**: 119–135

Weber APM, Linka N (2011) Connecting the plastid: transporters of the plastid envelope and their role in linking plastidial with cytosolic metabolism. Annu Rev Plant Biol **62**: 53–77

Weitzel M, Nöh K, Dalman T, Niedenführ S, Stute B, Wiechert W (2013) 13CFLUX2--high-performance software suite for ^{13}C-metabolic flux analysis. Bioinformatics **29**: 143–5

Wiechert W, Möllney M, Petersen S, de Graaf a a (2001) A universal framework for ^{13}C metabolic flux analysis. Metab Eng **3**: 265–83

Wilding EI, Brown JR, Bryant AP, Chalker AF, Holmes DJ, Ingraham KA, Iordanescu S, So CY, Rosenberg M, Gwynn MN (2000) Identification, evolution, and essentiality of the mevalonate pathway for isopentenyl diphosphate biosynthesis in gram-positive cocci. J Bacteriol **182**: 4319–4327

Williams TCR, Poolman MG, Howden AJM, Schwarzlander M, Fell DA, Ratcliffe RG, Sweetlove LJ (2010) A genome-scale metabolic model accurately predicts fluxes in central carbon metabolism under stress conditions. Plant Physiol **154**: 311–23

Wittig U, Kania R, Golebiewski M, Rey M, Shi L, Jong L, Algaa E, Weidemann A, Sauer-Danzwith H, Mir S, Krebs O, Bittkowski M, Wetsch E, Rojas I, Müller W (2012) SABIO-RK--database for biochemical reaction kinetics. Nucleic Acids Res **40**: D790–6

Xu P, Ranganathan S, Fowler ZL, Maranas CD, Koffas MAG (2011) Genome-scale metabolic network modeling results in minimal interventions that cooperatively force carbon flux towards malonyl-CoA. Metab Eng **13**: 587–578

Yin Y-G, Tominaga T, Iijima Y, Aoki K, Shibata D, Ashihara H, Nishimura S, Ezura H, Matsukura C (2010) Metabolic alterations in organic acids and gamma-aminobutyric acid in developing tomato (*Solanum lycopersicum L.*) fruits. Plant Cell Physiol **51**: 1300–14

Yoon S, Lee Y, Kim J, Lee S, Lee J, Kim J, Jung K, Shin Y, Keasling JD, Kim S (2006) Enhanced lycopene production in *Escherichia coli* engineered to synthesize isopentenyl diphosphate and dimethylallyl diphosphate from mevalonate. Biotechnol Bioeng **94**: 1025–1032

Zamboni N, Fischer E, Sauer U (2005) FiatFlux--a software for metabolic flux analysis from ^{13}C-glucose experiments. BMC Bioinformatics **6**: 209

Zha W, Rubin-Pitel SB, Shao Z, Zhao H (2009) Improving cellular malonyl-CoA level in *Escherichia coli* via metabolic engineering. Metab Eng **11**: 192–8

Zhang P, Foerster H, Tissier CP, Mueller L, Paley S, Karp PD, Rhee SY (2005) MetaCyc and AraCyc. Metabolic Pathway Databases. **138**: 27–37

Zhang Y, Butelli E, De Stefano R, Schoonbeek H-J, Magusin A, Pagliarani C, Wellner N, Hill L, Orzaez D, Granell A, Jones JDG, Martin C (2013) Anthocyanins double the shelf life of tomatoes by delaying overripening and reducing susceptibility to gray mold. Curr Biol **23**: 1094–100

Zurbriggen A, Kirst H, Melis A (2012) Isoprene production via the mevalonic acid pathway in *Escherichia coli* (Bacteria). BioEnergy Res **5**: 814–828

Appendix A